Winter 12-15-2016

Focusing Light Inside Scattering Media with Optical Phase Conjugation

Yan Liu
Washington University in St. Louis

Recommended Citation

Liu, Yan, "Focusing Light Inside Scattering Media with Optical Phase Conjugation" (2016). *McKelvey School of Engineering Theses & Dissertations*. 208.
https://openscholarship.wustl.edu/eng_etds/208

WASHINGTON UNIVERSITY IN ST. LOUIS

School of Engineering and Applied Sciences
Department of Biomedical Engineering

Dissertation Examination Committee:
Lihong V. Wang, Chair
Samuel Achilefu
Mark Anastasio
Timothy Holy
Jung-Tsung Shen
Lan Yang

Focusing Light Inside Scattering Media with Optical Phase Conjugation

by
Yan Liu

A dissertation presented to
The Graduate School
of Washington University in
partial fulfillment of the
requirements for the degree
of Doctor of Philosophy

December 2016
St. Louis, Missouri

Table of Contents

List of Figures

List of Abbreviations

DOPC:	Digital optical phase conjugation
FWHM:	Full width at half maximum
OPC:	Optical phase conjugation
PBR:	Peak-to-background ratio
PCM:	Phase conjugate mirror
SLM	Spatial light modulator
TRUE:	Time-reversed ultrasonically encoded

Acknowledgments

I would like to express my deep gratitude to my advisor, Professor Lihong V. Wang, for his support and guidance during my Ph.D. study. I have learned a lot from him, such as how to keep organized, how to do presentations, and the importance of good habits, diligence and open-mindedness. All of this can also benefit the rest of my life.

I would also like to thank all my colleagues in the Optical Imaging Laboratory. Especially, I want to thank Dr. Cheng Ma and Dr. Yuecheng Shen, the discussions with whom are always fruitful. They are role models for me on my journey to become a great scientist. I was fortunate to join our big group, because I had the opportunity to learn from many people. I learned a lot about engineering from Joon-Mo Yang, Maslov Konstantin, Robert Berry, Xiao Xu, Junhui Shi, Lidai Wang, Chiye Li, Lijun Ma and Lei Li. I want to express my gratitude to Puxiang Lai, Xiao Xu, Chiye Li, Chi Zhang, Junhui Shi, Liang Gao, Jinyang Liang, Lidai Wang, Zijian Guo, Jun Xia, Ashton Hemphill, Lei Li, Ruiying Zhang, Lijun Ma, Maslov Konstantin, Yuta Suzuki, Jian Wei Tay, Jiamiao Yang, Callie Li, Qiang Yang, Liren Zhu, Junjie Yao, Hsun-Chia Hsu, Alejandro Garcia, Joon-Mo Yang, Bin Rao, Yong Zhou, Song Hu, Yu Wang for their discussions and help. I also want to thank Kun Wang, Chao Huang, Feng Qiao, Yang Lou, Huifeng Guan, and Thomas Matthews in Prof. Mark Anastasio’s group for helpful discussions. In addition, I thank Prof. James Ballard, who helped proofread my manuscripts and improve my English.

I am lucky to have Prof. Mark Anastasio, Prof. Samuel Achilefu, Prof. Timothy Holy, Prof. Jung-Tsung Shen, Prof. Lan Yang and Prof. Lihong V. Wang on my thesis committee, and I am grateful for their time and guidance.

I thank Chiye Li and Alejandro Garcia for always giving me a ride, and being so nice to me.

My special thank goes to the McDonnell International Scholars Academy of Washington University, for providing me five years of fellowship for my PhD study, and all the opportunities that helped me improve myself, make friends with other scholars all over the world, and better understand the American culture.

Finally, I thank my parents for their constant love and support.

Yan Liu

Washington University in St. Louis

December 2016

ABSTRACT OF THE DISSERTATION

Focusing Light Inside Scattering Media with Optical Phase Conjugation

by

Yan Liu

Doctor of Philosophy in Biomedical Engineering

Washington University in St. Louis, 2016

Professor Lihong Wang, Chair

In scattering media such as biological tissue, the heterogeneous refractive index distribution causes light to scatter, which makes the media look opaque and prevents us from focusing light beyond ~1 mm deep inside the media to achieve optical imaging and manipulation. Hence, the ability to focus light deep inside scattering media is highly desired, and it could revolutionize biophotonics by enabling deep-tissue non-invasive high-resolution optical microscopy, optical tweezing, optogenetics, micro-surgery, and phototherapy.

To break the optical diffusion limit and focus light deep inside scattering media, optical phase conjugation based wavefront shaping techniques, such as time-reversed ultrasonically encoded (TRUE) optical focusing, are being actively developed. In this dissertation, I will describe our efforts to improve the performance (speed, focusing quality and focusing depth) of optical phase conjugation for future *in vivo* applications. Remarkably, we have focused light through tissue-mimicking phantoms up to 96 mm thick, and through *ex vivo* chicken breast tissue up to 25 mm thick.

Chapter 1: Introduction

1.1 Background and Motivation

In biomedicine, light focusing plays a critical role in imaging molecules with high resolution and sensitivity [1-3], and in delivering optical energy precisely at a targeted position to perform optical manipulation [4], stimulation [5], micro-surgery [6] and therapy [7]. However, in biological tissue, photons are scattered by wavelength-scale refractive index inhomogeneities. As a result, it becomes infeasible to use a lens to focus light beyond ~1 transport mean free path (l_t', corresponding to ~1 mm in human skin) [8-11], which fundamentally limits the imaging depth of conventional optical microscopy (e.g., confocal microscopy, two-photon microscopy, optical coherence tomography and optical-resolution photoacoustic microscopy) and the operating depth of non-invasive optical manipulation and therapy. Hence, it is highly desired to focus light deep inside scattering media such as biological tissue, which could revolutionize biophotonics.

To focus light through or inside highly scattering media, various wavefront shaping approaches are being actively developed [12-14], including feedback-based wavefront shaping [15], transmission matrix measurement [16, 17], and optical time reversal/optical phase conjugation (OPC) [18-20]. Among these techniques, OPC is most promising for *in vivo* applications, because it achieves the shortest average mode time [21] (the average operation time per degree of freedom) by determining the optimum wavefront globally instead of stepwise.

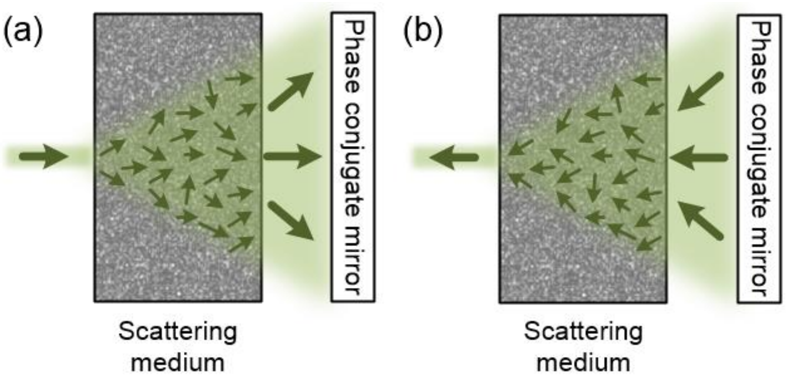

Figure 1.1 Illustration of optical phase conjugation. (a) A narrow beam illuminates a scattering medium and is scattered inside the medium. The distorted wave coming out of the medium is intercepted by a phase conjugate mirror. (b) The phase conjugate mirror generates the phase conjugated light, which retraces the original path back through the scattering medium and recovers the narrow incident beam.

Figure 1.1 illustrates a typical OPC experiment. In part (a), a narrow incident beam is scattered and broadened by a scattering medium. The distorted wave coming out of the medium is intercepted by a phase conjugate mirror (PCM) that performs optical phase conjugation. In part (b), the PCM produces the phase conjugate of the intercepted light in part (a). Since phase conjugation is equivalent to time reversal, the phase conjugated light retraces the original path back through the scattering medium and recovers the narrow incident beam. To achieve OPC, two types of PCMs have been developed. Analog PCMs employ nonlinear-optics-based static holography, four-wave mixing, or stimulated Brillouin scattering to generate the phase conjugated field [22, 23]; digital PCMs first employ a digital camera to measure the wavefront of the scattered light with digital holography, and then use a spatial light modulator (SLM) to reconstruct the conjugate wavefront of the scattered light [19, 20]. Although analog PCMs can be fast [24], however, the fluence reflectivity is low – the phase-conjugated light is much weaker than the scattered light impinging on the PCM. In comparison, digital PCMs [19, 20] have much higher fluence reflectivities ($\sim 10^5$), and is capable of synthesizing a light field [21, 25-28], thus becoming more useful and powerful.

To focus light inside a scattering medium with OPC, a PCM is used to phase conjugate the scattered light emitted from a guide star located deep inside the medium (Fig. 1.2) [13]. Time-reversed ultrasonically encoded (TRUE) optical focusing is one technique that employs focused ultrasound as a guide star, and it achieves optical focusing by ultrasound-guided optical phase conjugation [29-31]. Specifically, a PCM phase conjugates the ultrasound-modulated light emitted from an ultrasonic focus, thereby achieving optical focusing at the ultrasonic focus. TRUE focusing techniques using analog PCMs and digital PCMs are called analog TRUE focusing and digital TRUE focusing, respectively.

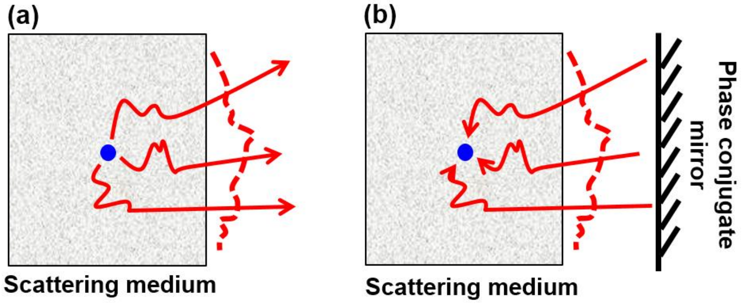

Figure 1.2 Focusing light inside scattering media with guide star based optical phase conjugation. (a) A guide star located deep inside the scattering medium emits light, whose wavefront is distorted by the scatterers inside the medium during light propagation. (b) A phase conjugate mirror measures the wavefront of the scattered light exiting the medium, and then phase conjugates the scattered light back to the guide star.

1.2 Dissertation outline

In Chapter 2, we used the hyperboloid-based Monte Carlo simulation method to quantitatively study the effect of light scattering on the quality of optical focusing inside scattering media [10]. To focus light deep inside living biological tissue, we need to improve the speed of TRUE focusing, because, otherwise, the motion of the scatterers inside tissue would break the time-reversal symmetry. In Chapter 3, we developed high-speed TRUE focusing using a fast responding photorefractive crystal ($Sn_2P_2S_6$:Te 1%) [24], a lock-in camera [32, 33], a ferroelectric liquid-crystal based spatial light modulator and a binary wavefront measurement method. To improve the quality of the focus achieved by OPC, in Chapter 4, we developed full-polarization digital OPC [34] and employed sub-Nyquist sampling of speckle grains [35]. In Chapeter 5, we improved the focusing depth of OPC by using a laser with a long coherence length and an optimized digital OPC system that can safely deliver more light power. We focused 532 nm light through tissue-mimicking phantoms up to 9.6 cm thick, as well as through *ex vivo* chicken breast tissue up to 2.5 cm thick [36].

Chapter 2: Monte Carlo simulation of optical focusing inside scattering media

In this chapter, we quantitatively study the effects of light scattering on the quality of optical focusing inside scattering media.

2.1 Methods

A Monte Carlo method [37] is often used to calculate the optical fluence distribution inside scattering media. The traditional way to simulate optical focusing with the Monte Carlo method is geometric focusing, in which the initial propagation direction of a photon packet launched on the tissue surface is simply toward the geometric focus of the beam [11]. This method cannot simulate the diffraction limit of the fluence distribution on the focal plane to study the broadening of the focal spot size due to scattering, because the fluence at the focal point is always much larger than the fluence at the grid points next to the focal point [38]. Instead, we used the hyperboloid focusing method to simulate optical focusing [39, 40] and we derived the formulae that can be directly used in standard a Monte Carlo simulation [8, 37].

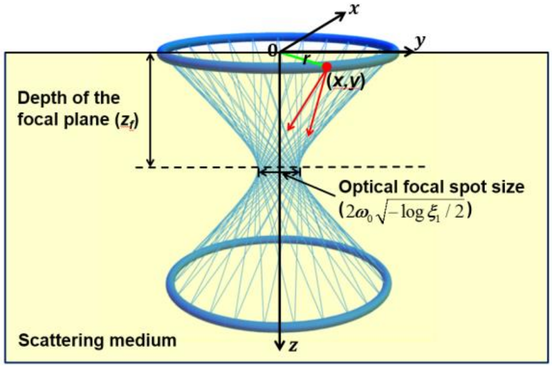

Figure 2.1 Illustration of the hyperboloid focusing method. A hyperboloid of one sheet whose focal constant is $2\omega_0\sqrt{-\log\xi_1/2}$ (sampled from the Gaussian distribution with a 1/e^2 characteristic length of ω_0) is shown (in blue). The position and the two possible propagation directions of a photon packet launched on the tissue surface are shown as a red dot and two red arrows. *r, x, y* are the radial position and the coordinates of the photon packet. ξ_1 is a random number that is uniformly distributed between 0 and 1.

In order to simulate the fluence distribution of a Gaussian beam focused into a scattering medium, we can construct the incident Gaussian beam by a set of hyperboloids of revolution of one sheet with different focal constants. A hyperboloid of one sheet is a doubly ruled surface, i.e., through each point there are two distinct lines that lie on the surface (Fig. 2.1). When the position of a photon packet launched on the tissue surface is generated in the Monte Carlo simulation, the two lines passing through this point while lying on the hyperboloid can be described by their direction cosines:

$$\text{Line 1: } u_x = \frac{-\hat{z}_f(\hat{z}_f x + y)}{(\hat{z}_f{}^2 + 1)L}, u_y = \frac{\hat{z}_f(x - \hat{z}_f y)}{(\hat{z}_f{}^2 + 1)L}, u_z = \frac{z_f}{L}, \tag{2.1}$$

$$\text{Line 2: } u_x = \frac{-\hat{z}_f(\hat{z}_f x - y)}{(\hat{z}_f{}^2 + 1)L}, u_y = \frac{-\hat{z}_f(x + \hat{z}_f y)}{(\hat{z}_f{}^2 + 1)L}, u_z = \frac{z_f}{L}, \tag{2.2}$$

where z_f is the depth of the focal plane, $\hat{z}_f = \frac{z_f}{z_0}$ is the normalized z_f, $z_0 = \frac{\pi\omega_0^2}{\lambda}$ is the Rayleigh range, $L = \sqrt{\frac{\hat{z}_f{}^2 r^2}{\hat{z}_f{}^2 + 1} + z_f{}^2}$ is a normalization factor to make $\bar{u} = (u_x, u_y, u_z)$ a unit vector, $\omega_0 = \frac{1}{\pi}\frac{\lambda}{NA}$ is the beam waist of the Gaussian beam [41] if the fill factor of the back aperture of the objective is 1, r is the radial position of a photon packet and x, y are the coordinates of a photon packet. Here, we set up a Cartesian coordinate system (Fig. 2.1). The x-y plane is on the surface of the scattering medium, and the z axis is the normal of the surface, pointing to the scattering medium [8]. The initial propagation direction of a photon packet is chosen from the two directions described by Eqs. (2.1) and (2.2) with equal probability. When there is no scattering, the trajectories of photon packets generated with the same r form a hyperboloid of revolution of one sheet. By samplin r according to the Gaussian distribution, we can generate a set of hyperboloids of one sheet. The resulting fluence distribution can perfectly reproduce the intensity distribution of a Gaussian beam when the medium is clear. In summary, we generate the position and the propagation direction of a photon packet launched on the surface of a scattering medium using the following steps:

1) Generate the radial position of a photon packet by $r = \left(\omega_0 \sqrt{1+\hat{z}_f^{\,2}}\right)\sqrt{-\log \xi_1 / 2}$.

2) Generate the *x*, *y* position of the photon packet from r by $\theta = 2\pi\xi_2, x = r\cos(\theta), y = r\sin(\theta)$.

3) Generate a random number ξ_3. If $0 < \xi_3 < 0.5$, the propagation direction of the photon packet is set according to Eq. (2.1); if $0.5 \le \xi_3 < 1$, the propagation direction is set according to Eq. (2.2).

In 1)-3), $\xi_i, i = 1, 2, 3$ is a random number that is uniformly distributed between 0 and 1. The rest of the procedure is similar to that in a standard Monte Carlo simulation [8, 37]. Thus, by using Eqs. (2.1) and (2.2) that we derived and following the above three steps for photon launching, the hyperboloid focusing method can be easily integrated into standard software packages such as MCML [37].

In our simulations, we assumed the following tissue optical parameters [8]: the scattering anisotropy g = 0.9, the scattering coefficient μ_s = 100 cm^{-1}, and the absorption coefficient μ_a = 0.1 cm^{-1}. As this work targets on studying the effects of light scattering on optical focusing, we used the refractive-index-matched boundary condition (i.e., the refractive indices of both the tissue and the water are 1.33) to avoid the effect of aberration caused by the mismatch in refractive index between the tissue and the ambient medium. The numerical aperture (NA) of the optical objective lens in air is 0.1 [42]. The optical wavelength was 570 nm, which was an isosbestic point for oxy- and deoxy-hemoglobin molecules. We chose a grid size dr = 0.1 µm along the radial direction, which is more than 10 times smaller than the optical focal spot size (full width at half-maximum (FWHM) spot size = 1.6 µm, and the radius defined by $1/e^2$ of the peak value = 1.36 µm). We chose a grid size dz = 1 µm along the z direction. From the optical properties of the scattering medium, we could obtain the mean free path $l_t = 1/(\mu_s+\mu_a) \approx 100$ µm and the transport mean free path [8] $l_t' = 1/(\mu_s(1-g)+\mu_a) \approx 1$ mm.

2.2 Results

The fluence distributions on the focal plane at varied z_f are shown in Figs. 2.2(a) and (b), from which we can see that the shoulder of the distribution rises with the increase of z_f, due to scattering. When z_f is close to 1 l_t', the FWHM of the distribution is not broadened much (2% when z_f = 0.9 l_t' and 14% when z_f = 1.1 l_t'), compared with the case of no scattering. When z_f is greater than 1 l_t', the shoulder of the distribution rises very quickly with increasing z_f. When z_f = 1.7 l_t', the fluence at 50 µm radial distance away from the focal point is 93% of that at the focal point, which shows that optical focusing is very weak. Due to the lack of computing power, we did not simulate the case for larger z_f by directly using the Monte Carlo method. Instead, we used the diffusion theory [8] to compute the fluence distribution when z_f = 3 l_t', and we can see from Fig. 2.2(a) that no optical focusing can be discerned. The number of scattering events (N_s) for the field points on the focal plane at varied z_f is shown in Fig. 2.2(c). Within the depth of 1 l_t', N_s is close to zero for field points inside the optical focal spot. When z_f is greater than 1 l_t', N_s increases quickly. When z_f = 1.7 l_t', N_s at the focal point is greater than 40. We can also see that for a given z_f, N_s for the field points outside the optical focal spot is always larger than that for the field points inside the focal spot. The on-axis fluence distributions corresponding to different z_f are shown in Fig. 2.2(d). The fluence at the focal point decays exponentially with the increase of z_f when z_f is smaller than 1.3 l_t'. The decay rate is 9.93 mm^{-1}, close to $\mu_t = \mu_s + \mu_a$ = 10.0 mm^{-1}, which agrees with Beer's law. Beyond 1.3 l_t', the fluence at the focal point decays more slowly.

When z_f is greater than 0.9 l_t', the on-axis fluence near the surface of the scattering medium becomes stronger than that on the focal plane.

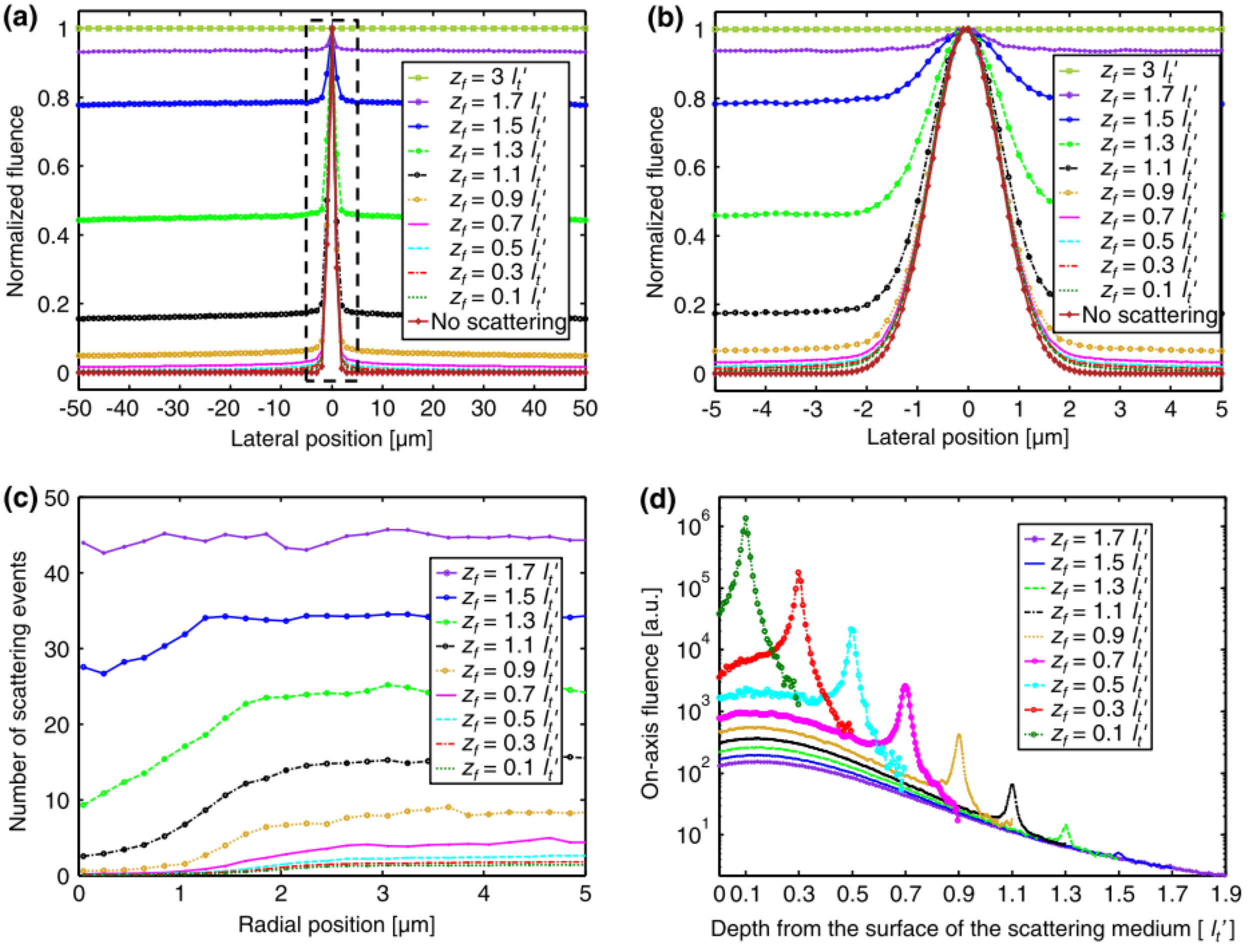

Figure 2.2 Fluence distribution and number of scattering events at different depth of the focal plane. (a) The fluence distribution on the focal plane at varied z_f. (b) A close-up of the region denoted by the dashed box in (a). (c) The number of scattering events for the field points on the focal plane at varied z_f. (d) The on-axis fluence distributions corresponding to different z_f.

Figure 2.3 shows the two dimensional fluence distributions at four different z_f (from 100 μm to 1300 μm). We can see the contrast of the focus becomes poorer and poorer with increasing z_f, and we can barely observe a focus when z_f = 1.3 mm.

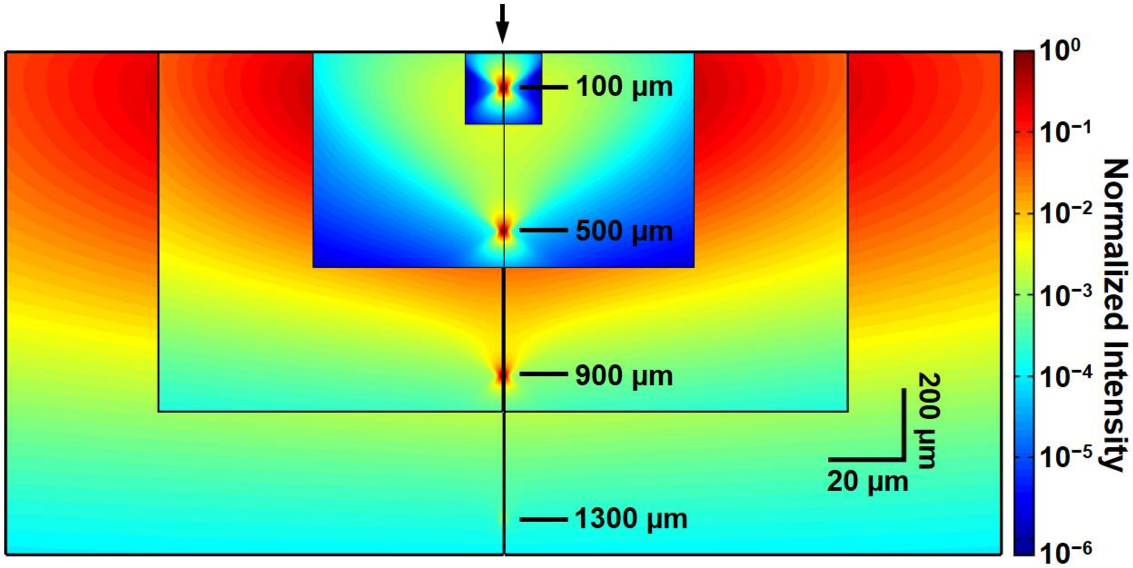

Figure 2.3 Two-dimensional fluence distributions at four different z_f (from 100 μm to 1300 μm).

2.3 Discussion and Conclusion

Focusing light deep inside scattering media is highly desired in optical imaging, sensing, therapy and manipulation. The transport mean free path, l_t', indicates the mean propagation distance that it takes for photons to lose memory of the initial propagation direction they had before entering the scattering medium [9]. Thus, optical focusing beyond one l_t' is generally regarded as infeasible. However, the lateral resolution when $z_f = 1\ l_t'$ and how it decays with depth have not been studied sufficiently, either theoretically or experimentally. In this work, we found that when z_f is close to 1 l_t', the FWHM of the corresponding fluence distribution is not broadened much (2% when $z_f = 0.9\ l_t'$ and 14% when $z_f = 1.1\ l_t'$), compared with the case of no scattering. This seems somewhat surprising, yet agrees with the simulation results by Hayakawa et al. [43]. When z_f is greater than 1 l_t', the shoulder of the fluence distribution rises very quickly with increasing z_f. When $z_f = 1.7\ l_t'$, the fluence at 50 μm radial distance away from the focal point is 93% of that at the focal point, which shows that optical focusing is already very weak at this depth. Experiments to validate these results are expected to be done in future work. Our simulation results show that it is not possible to focus light deep inside scattering media using just a lens. This motivates us to develop wavefront shaping techniques such as TRUE focusing to focus light deep inside scattering media.

From the on-axis fluence distribution in Fig. 2.2(d), we can see that when z_f is greater than 0.9 l_t', the fluence near the surface of the scattering medium becomes stronger than that on the focal plane, which degrades the image contrast of two-photon microscopy and is known as the fundamental limit of the maximum imaging depth of this image modality and other nonlinear optical microscopy [44].

It is important to note that the Monte Carlo method only describes the transport of energy, therefore it is incapable of modeling coherent phenomena. This limitation also applies to the hyperboloid-focusing-based Monte Carlo method. Although an imperfect method to simulate optical focusing in a scattering medium, it has been validated by some models and experiments. In the original paper that described this method [39], the heterodyne efficiency factors and the transverse intensity distribution simulated by the hyperboloid-focusing-based Monte Carlo method agree with those simulated by the extended Huygens-Fresnel (EHF) model [45], which is a widely-acknowledged model in OCT and has been validated experimentally. Good agreement between the heterodyne efficiency factors obtained by the Monte Carlo simulation and by experiments was also reported [46]. Moreover, two-photon fluorescence signals were simulated by the hyperboloid-focusing-based Monte Carlo method, and the result agreed well with the experiments [47].

The hyperboloid focusing method used in the Monte Carlo simulation provides a way to simulate optical focusing. However, when the grid size is small (e.g., $dr = 0.1$ µm and $dz = 1$ µm were used in this work), in order to obtain an acceptable statistical error in the result, 2×10^{10} photon packets with a cut-off weight of 10^{-4} were used to simulate the fluence distribution when $z_f = 0.9\ l_t'$, and 4×10^{12} photon packets were used when $z_f = 1.7\ l_t'$. Thus, graphics processing units (GPU) are highly recommended to accelerate the Monte Carlo simulation [48].

Chapter 3: Improving the speed of time-reversed ultrasonically encoded (TRUE) optical focusing

TRUE optical focusing have been confined to experimentation with static scattering media, such as ground glass diffusers, translucent tapes, tissue-mimicking phantoms, and *ex vivo* biological tissue, whose speckle correlation times are greater than 1 s. None has been applied to focusing light inside dynamic scattering media or living biological tissue. This restriction is due to the requirement that the deterministic property of light propagation in the scattering medium must be maintained during the entire time-reversal (optical phase conjugation) process (including both the measurement of the wavefront and the playback of the wavefront). In living biological tissue, the displacement of scatterers due to blood flow, heartbeat, breathing, and Brownian motion causes the speckle pattern (a random interference pattern formed by coherent light after propagating through a scattering medium) to decorrelate, reducing the speckle correlation time to the order of 1 ms [24, 49, 50], which further depends on the depth of interrogation. However, the speeds of previous TRUE focusing implementations were limited to no greater than 1 Hz, thus preventing them from *in vivo* applications. Figure 3.1 illustrates the influence of the response speed of a phase conjugate mirror during wavefront measurement on the quality of TRUE optical focusing. If the PCM does not respond fast enough, a blurred hologram will be recorded [Fig. 3.1(b)]. When this blurred hologram is read, no optical focus can be formed at the ultrasonic focal position [Fig. 3.1(d)]. Therefore, in order to achieve optical focusing inside dynamic scattering media, the PCM must respond sufficiently fast, so that hologram recording and reading can be completed within the speckle correlation time [Figs. 3.1(c) and 3.1(e)].

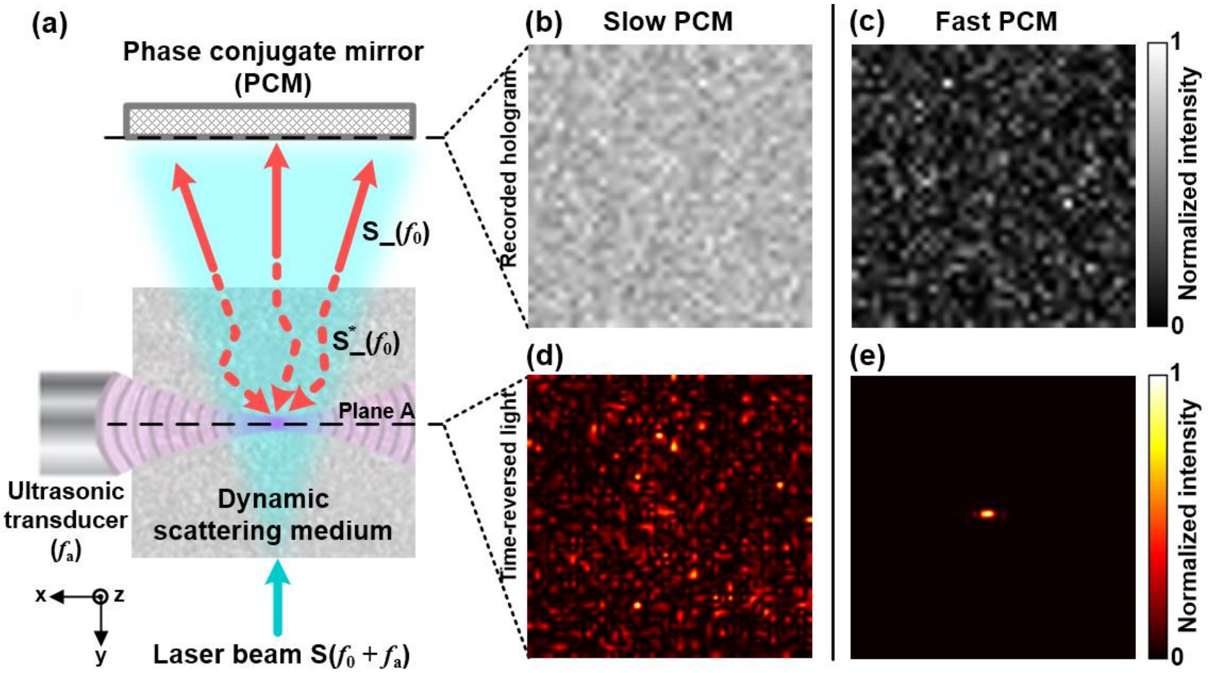

Figure 3.1 Influence of the response speed of a phase conjugate mirror (PCM) during wavefront measurement on the quality of TRUE optical focusing. (a) Illustration of the TRUE focusing concept. Laser light S with a frequency of $f_0 + f_a$ illuminates a scattering media and a portion of the diffuse light traversing the acoustic focus is frequency-down-shifted to f_0 (the frequency of the acoustic wave is f_a). A PCM records the wavefront of these ultrasonically modulated light $S_-(f_0)$ in a hologram and then phase conjugates the light back to the ultrasonic focus, thereby forming a focus. Dashed arrows indicate time-reversed light. Plane A denotes the *x*-*z* plane intersecting the acoustic axis. (b)−(c) Simulated recorded holograms in a slow (b) and fast (c) PCM. Hologram blurring is clearly visible in (b) as a reduction in speckle contrast. (d)−(e) Simulated light intensity distribution on plane A by reading the hologram recorded in the slow (d) and fast (e) PCM. No focusing can be observed in (d). All the images in (b)−(e) were normalized by their own maximum values. Abbreviations: S, sample light; S_-, frequency-down-shifted sample light (signal light); S_-^*, time-reversed signal light; TRUE, time-reversed ultrasonically encoded.

3.1 High-speed analog TRUE focusing based on a $Sn_2P_2S_6$:Te 1% crystal

3.1.1 Methods

Here, we present a solution to overcome the optical focusing challenges in non-static scattering media, by developing a high-speed TRUE focusing system with a 1% tellurium-doped tin thiohypodiphosphate ($Sn_2P_2S_6$:Te 1%) photorefractive crystal [51-53] as the PCM. The crystal is sensitive to light around 790 nm wavelength, making it particularly suitable for focusing light deep inside biological tissue, since the attenuation of near-infrared light in tissue is weaker than that of visible light [54]. More importantly, the crystal responds on the order of milliseconds under moderate light illumination (e.g., 7 ms at 1 W cm^{-2} and 1.3 ms at 10 W cm^{-2}), which is potentially fast enough to overcome the rapid speckle decorrelation caused by living tissue. Through direct visualization of the time-reversed light pattern, and by imaging an absorptive target embedded inside a dynamic scattering medium, we evaluated the TRUE focusing performance of our system at various speckle decorrelation rates. We confirm that our system is able to focus light inside a dynamic scattering medium having a speckle correlation time as short as 5.6 ms. Then, we achieved the first optical focusing of diffuse light inside a scattering medium containing living biological tissue.

Experimental set-up

The experimental set-up for imaging the absorptive target with TRUE light is schematically shown in Fig. 3.2. The light source was a 1.6 W continuous-wave Ti:Sapphire laser (MBR 110, Coherent, USA) operating at 793 nm, pumped by a 532 nm continuous-wave laser (Verdi 10, Coherent, USA). A TRUE focusing procedure consisted of recording and reading a hologram. In the recording phase, the laser output was switched to horizontal polarization by an electro-optic modulator (EOM, 350-80-LA-02, Conoptics, USA) to transmit through the first polarizing beamsplitter (PBS1). The residual light reflected from PBS1 was completely blocked by a mechanical shutter MS2 (Uniblitz LS3, Vincent Associates, USA). The transmitted light was split into a sample beam and a reference beam by PBS2, with a splitting ratio controlled by the second half-wave plate (HWP2). The sample beam S passed through two acousto-optic modulators (AOM, IntraAction AOM-802AF1) to achieve a frequency shift to $f = f_0 + f_a$, where f_0 was the laser frequency and f_a (3.5 MHz) was the frequency shift due to the two AOMs (shifted by +75 MHz, and −71.5 MHz, respectively). A function generator (33250A, Agilent, USA) sent a 150 mVpp sinusoidal wave with a frequency of f_a to a 50 dB gain RF power amplifier (325LA, ENI, USA) to drive the spherically focused ultrasonic transducer (A381S 3.5 MHz, Panametrics, USA). Due to the acousto-optic effect, a small portion of the light traversing the acoustic focus was frequency-shifted to f_0 and $f_0 + 2f_\mathrm{a}$. Only the frequency-down-shifted (i.e., at f_0) sample light (also called signal light) S_{-} and the reference beam R contributed to a stable hologram in the $Sn_2P_2S_6$:Te 1% crystal (6×6×6 mm^3). When interfering with R, the sample light at frequency $f_0 + f_\mathrm{a}$ (or $f_0 + 2f_\mathrm{a}$) formed a beat with a frequency of f_a (or $2f_\mathrm{a}$), which was too fast for the crystal to respond to and the hologram was washed out. The R and S beams illuminated the PRC at about ± 11 degrees from the normal of the PRC surface for 10 ms and 5 ms in the dynamic phantom and the living tissue experiments, respectively. In the hologram reading phase, the laser light was switched to vertical polarization by the EOM and reflected by PBS1 to form the reading beam R^*, which was phase-conjugated to R. The residual horizontally polarized light transmitted through PBS1 was blocked by the shutter MS1. When the 3.4 W cm^{-2} R^* beam illuminated the PRC, the time-reversed signal light S_{-}^{*} was generated and converged back to the acoustic focus. A portion of S_{-}^{*} was then reflected by a beamsplitter (BS) and detected by a photodiode (PDA36A, Thorlabs, USA) with a 70 dB gain. The signal was digitized by an oscilloscope (TDS 5034, Tektronix, USA) running in fast frame mode and sent to a PC via a GPIB cable and a GPIB-USB controller. The ultrasound was off during the hologram reading phase. Although R^* was on for 2 ms (the minimum exposure time determined by the mechanical shutter), the maximum signal amplitude was detected by the photodiode immediately after the shutter MS2 was opened since the signal decayed quickly as the hologram was being washed out by the reading beam. The intralipid-gelatin phantom was mounted on a linear stage (462-X-M, Newport, USA) driven by a motorized actuator (CONEX-TRA25CC, Newport, USA) to control the movement speed. The timing of the EOM, shutters, and function generators was controlled by a pulse delay generator (DG645, Stanford Research Systems, USA) which was externally triggered by a multifunction DAQ (NI USB-6008, National Instruments, USA) controlled by a PC.

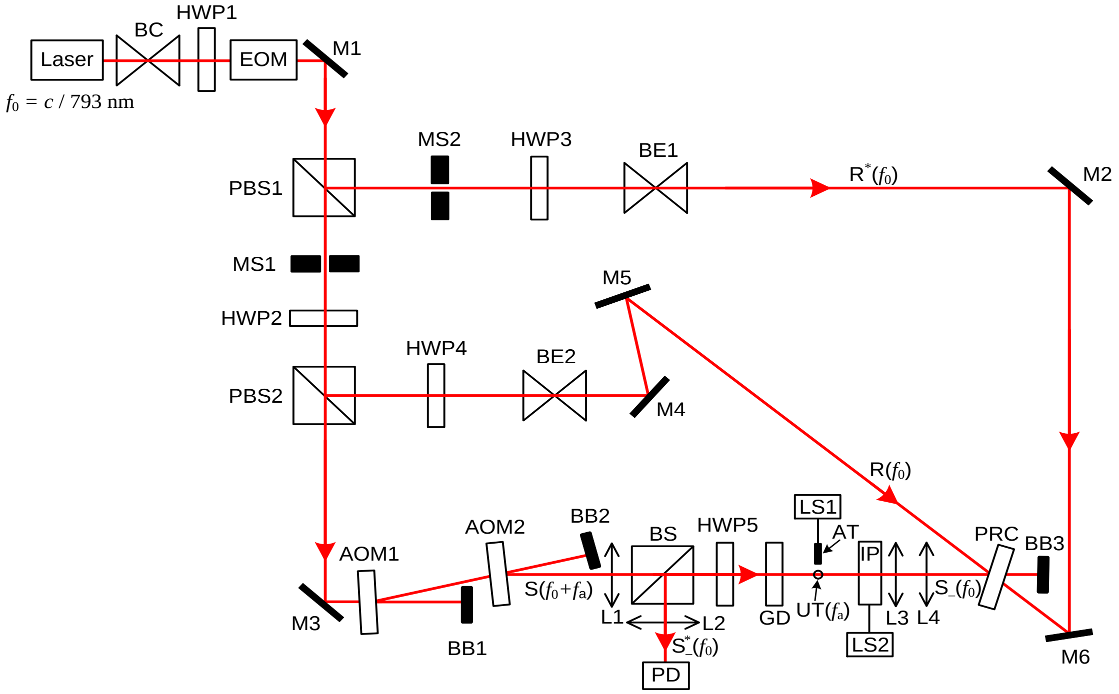

Figure 3.2 Schematic of the experimental set-up for imaging an absorptive target inside a dynamic scattering medium with TRUE optical focusing. Abbreviations: AOM, acousto-optic modulator; AT, absorptive target; BB, beam block; BC, beam condenser; BE, beam expander; BS, beamsplitter; EOM, electro-optic modulator; f_0, frequency of the laser light; f_a, frequency detuning applied by AOMs, which was also the frequency used to drive the ultrasonic transducer; GD, ground glass diffuser; HWP, half-wave plate; IP, intralipid-gelatin phantom, mounted on a motorized linear stage; L, lenses; LS, linear stage; M, mirror; PBS, polarizing beamsplitter; PD, photodiode; PRC, photorefractive crystal; R, reference beam; R*, reading beam, phase conjugate to R; S, sample light; S_-, frequency-down-shifted sample light (signal light); S_-^*, time-reversed signal light; MS, mechanical shutter; UT, ultrasonic transducer.

Measurement of the speckle correlation time of the sample

To measure the speckle correlation time (τ_c) of the dynamic phantom, we used a CMOS camera (208 fps, 320×108 pixels, global shutter, exposure time = 0.062 ms, FMVU-03MTM, Point Grey, Canada) to record the speckle patterns magnified by an objective (40×, NA = 0.65, tube length = 160 mm, Leica E_1 ACHRO). The NA of the objective was chosen to be greater than the image space NA of lens L (0.23), so that it did not restrict the NA of the system. Otherwise, τ_c cannot be measured correctly since it is inversely proportional to the NA of the objective when NA < 0.23, which was proved in theory and verified by our experiments using objectives with different NA (data not shown).

To measure τ_c of the living tissue, we illuminated the left mouse ear (sandwiched between a cover slip (thickness = 0.17 mm, VWR 48393-172) and a microscope slide (thickness = 1 mm, Corning 2947-75×25)) with a beam 5.0 mm in diameter; the large vessels in the center were covered by the beam. The other mouse ear was bent downward and taped to the home-built animal holder to avoid blocking the light. During the experiment, the mouse (15-week-old, Female, Hsd:Athymic Nude-Foxl NU, Harlan Co., USA) was held on a heating pad (SRFG-104/10, Omega, USA) whose temperature was set to 37 °C by a controller (YO-89802-52, Cole-Parmer, USA) to maintain the mouse's body temperature. This temperature was crucial to keep a normal blood flow speed. The mouse was held steady with a home-machined hard palate fixture and kept still by using a breathing anesthesia system (E-Z Anesthesia, Euthanex, USA). All experimental animal procedures were carried out in conformity with the laboratory animal protocol approved by the Animal Studies Committee at Washington University in St. Louis. At first, a CMOS camera (30 fps, 344×216 pixels, global shutter, exposure time = 0.062 ms, FMVU-03MTM, Point Grey, Canada) was used to record the speckle patterns magnified by an objective (60×, NA = 0.80, tube length = 160 mm, Nikon, Japan). Then, a faster sCMOS camera (pco. Edge, PCO AG, Germany) was used to record speckle patterns at a higher frame rate (2271 fps, 160×38 pixels, global shutter, exposure time = 0.010 ms), from which we obtained τ_c of a living-mouse ear. We shifted the positions of the objective and the camera to record the speckle patterns at 5 different locations on the mouse ear. To block the blood flow, a metal bar pressed the ear against a stiff acrylic wall. We monitored the speckle patterns from 20 seconds till 12 minutes after blocking the blood flow, and no fast-decorrelating (on a time scale of 1–10 ms) speckle patterns were observed.

Determination of the image resolution

Since the one-dimensional (1D) point spread function of the system can be approximated by a Gaussian function $\mathrm{PSF}(x) = A\exp(-x^2/2\sigma^2)$, and the transmission of the object (whose boundary positions are specified by x_1 and x_2) can be approximated by a rectangular function $\mathrm{o}(x) = -B[\mathrm{u}(x-x_1) - \mathrm{u}(x-x_2)]$, the 1D image of the object can be written theoretically as a convolution: $\mathrm{y}(x) = \mathrm{PSF}(x) * \mathrm{o}(x) = C\left[\mathrm{erf}(\frac{x-x_1}{\sqrt{2}\sigma}) - \mathrm{erf}(\frac{x-x_2}{\sqrt{2}\sigma})\right]$, where *A*, *B*, *C* are constants, $\mathrm{u}(x)$ is the step function, and $\mathrm{erf}(x) = \frac{2}{\sqrt{\pi}}\int_0^x \exp(-t^2)dt$ is the error function. By fitting the experimental data with $\mathrm{y}(x) = C\left[\mathrm{erf}(\frac{x-x_1}{\sqrt{2}\sigma}) - \mathrm{erf}(\frac{x-x_2}{\sqrt{2}\sigma})\right] + D$, we obtained σ, which was related to the image resolution (defined as the full-width at half maximum (FWHM) of the Gaussian profile) as in $\mathrm{FWHM} = 2\sqrt{2\ln 2}\sigma$.

Measurement of the optical thickness of a living-mouse ear

We illuminated the living-mouse ear perpendicularly with a collimated laser beam (beam width ~ 1.5 mm) and measured the power of the transmitted ballistic light at two meters away [8, 31] from the ear using a photodiode (PDA36A, Thorlabs, USA) to be $(2.8 \pm 0.3) \times 10^{-8}$ of the power of the incident light. Thus, the optical thickness of the mouse ear, defined as the negative natural logarithm of the fraction of unscattered light, was measured to be 17.4 ± 0.1 (for 6 mice). All mice were under anesthesia during the measurement.

Blocking blood flow in a living mouse

To study the origin of the fast speckle decorrelation, we measured the speckle patterns of light passing through a living mouse ear, before and after blocking its blood flow. A metal bar was used to press the mouse ear against a stiff acrylic wall to block its blood flow (Fig. 3.3).

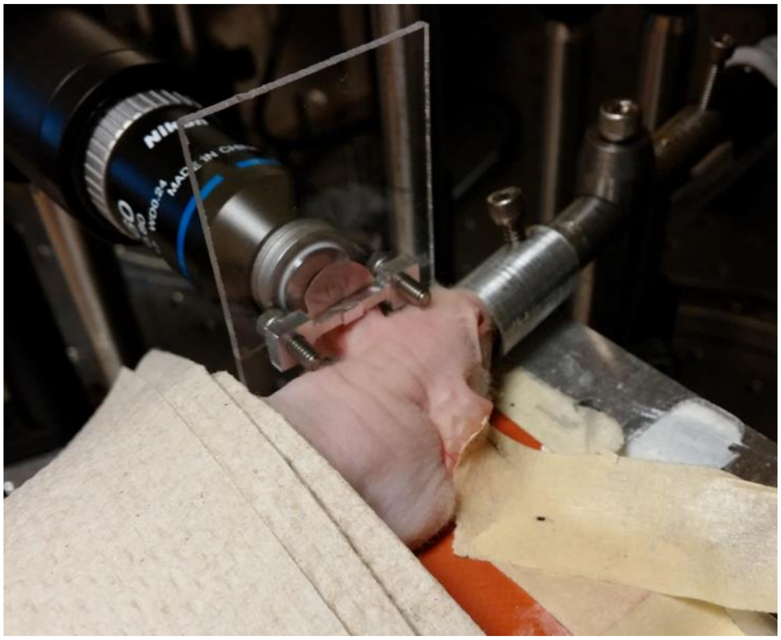

Figure 3.3 A photo of the set-up to measure the speckle correlation time after blocking the blood flow in a living mouse ear.

Sample preparation

The intralipid-gelatin phantom was made from intralipid (Intralipid® 20%, Fresenius Kabi, Sweden), porcine skin gelatin (10% by weight, #G2500-1kG, gel strength 300, Sigma-Aldrich, USA) and de-ionized water [55] with a lipid concentration of 1.5 g ml^{-1}. The reduced scattering coefficient μ_s' was measured by a home-built oblique incidence reflectometer [56] to be 9.8 cm^{-1}. Acrylic spacers with a thickness of 1.5 mm were sandwiched between two acrylic sheets to accurately control the thickness of the intralipid-gelatin phantom to be 1.5 mm (equivalent to 1.5 l_t'). The clear gelatin-gel layer was made from porcine skin gelatin (10% by weight) and de-ionized water. The optical absorptive target (3.9 mm × 1.3 mm × 20.0 mm along the *x, y* and *z* direction) was made from black ink, gelatin, and distilled water. The absorption coefficient of the target was 0.80 cm^{-1}, as measured by a spectrophotometer (Cary Eclipse, Varian, USA). The diffuser (DG20-120, Thorlabs, USA) was embedded inside the gelatin gel to position it closer to the absorptive target (distance = 8.0 mm) and the intralipid-gelatin layer (distance = 22.1 mm) without blocking the ultrasonic waves.

Simulation methods

Here we describe the simulation methods to obtain the results shown in Fig. 3.1. Inside the scattering media, the 2-dimensional (2D) light field on the *x*-*z* plane intersecting the acoustic axis (denoted as plane A, see Fig. 3.1(a)) was represented by a random complex matrix $\mathbf{A}_0$ (dimension = 40×40), whose elements followed a circular Gaussian distribution [57]. Upon ultrasonic modulation, the light field became $\mathbf{A}=\mathbf{A_0}\cdot\times\mathbf{I_{US}}$, where "$\cdot\times$" represents element-wise multiplication, and $\mathbf{I_{US}}$ is the 2D acoustic intensity distribution on plane A, approximated by

$I_{\mathrm{US}}(x,z) = \dfrac{I_0}{\omega_0^{\,2}\left[1+\left(\dfrac{z}{z_0}\right)^2\right]} \exp\left\{-2x^2/\omega_0^{\,2} \middle/ \left[1+\left(\dfrac{z}{z_0}\right)^2\right]\right\}$. I_0 is a constant, $\omega_0 = \dfrac{1}{\pi}\dfrac{\lambda}{NA}$, $z_0 = \dfrac{\pi\omega_0^{\,2}}{\lambda}$,

where NA is the numerical aperture of the transducer, and λ is the acoustic wavelength. $\mathbf{A}$ was then reshaped to a column vector $\mathbf{a}$ with a dimension of 1600×1. Propagation of the ultrasonically encoded light through the scattering medium and the free space was simulated by multiplying $\mathbf{a}$ with a transmission matrix $\mathbf{T}$ (dimension = 1600×1600) [16]. In our experiment, the number of modes on the PRC was much smaller than the total number of output modes. Under this condition, the elements of $\mathbf{T}$ obeyed a circular Gaussian distribution . The signal light field on the PRC was calculated by $\mathbf{b} = \mathbf{Ta}$. To simulate dynamic scattering media, we generated 51 independent random matrices $\mathbf{T}_\mathbf{i}$ (i = 0, 1, 2,⋯, 50, representing the scattering medium at the time of i ms), whose elements followed the circular Gaussian distribution and $\mathbf{T}_\mathbf{i}^\dagger \mathbf{T}_\mathbf{i} \approx \hat{\mathbf{I}}$, where "$\dagger$" denotes conjugate transpose and $\hat{\mathbf{I}}$ is the identity matrix. Since different matrices $\mathbf{T}_\mathbf{i}$ were uncorrelated, $\mathbf{b}_\mathbf{i} = \mathbf{T}_\mathbf{i}\mathbf{a}$ were uncorrelated, so the speckle correlation time τ_c was smaller than 1 ms. The signal light $\mathbf{b}_\mathrm{i}$ interfered with a reference beam R (whose electric field was represented by a vector $\mathbf{R}$ (dimension = 1600×1) in which all elements were 1), and formed an interference pattern $\mathbf{I}_\mathbf{i} = |\mathbf{b}_\mathbf{i} + \mathbf{R}|^2$ on the PRC. The hologram recorded on the PCM at time t can be calculated by[56] $\mathbf{h}(t) \propto \int_0^t \mathbf{I}(t-\tau)\exp(-\tau/\tau_\mathrm{r})d\tau$, where τ_r is the response time of the PCM. We let $\tau_{\mathrm{r\_f}}$ and $\tau_{\mathrm{r\_s}}$ denote the response times of a fast PCM and a slow PCM, and assumed $\tau_{\mathrm{r\_f}} \ll \tau_\mathrm{c}$ and $\tau_{\mathrm{r\_s}} \gg \tau_\mathrm{c}$. So, at t = 50 ms, the hologram recorded in a slow PCM (shown in Fig. 3.1(b)), $\mathbf{h}_\mathrm{s}$, was approximately proportional to (and simulated by) $\sum_{\mathrm{i}=0}^{50} \mathbf{I}_\mathbf{i} = \sum_{\mathrm{i}=0}^{50} |\mathbf{b}_\mathbf{i} + \mathbf{R}|^2$ (since

$\mathbf{h}_\mathrm{s} \propto \int_0^{t=50\ \mathrm{ms}} \mathbf{I}(t-\tau)\exp(-\tau/\tau_{\mathrm{r\_s}})d\tau$), and the hologram recorded in a fast PCM (shown in Fig. 3.1(c)), $\mathbf{h}_\mathrm{f}$, was approximately proportional to (and simulated by) $\mathbf{I}_{\mathbf{50}}$ = $|\mathbf{b}_{\mathbf{50}} + \mathbf{R}|^2$ (since $\mathbf{h}_\mathrm{f} \propto \int_0^{t=50\ \mathrm{ms}} \mathbf{I}(t-\tau)\exp(-\tau/\tau_{\mathrm{r\_f}})d\tau$).

In the time-reversal step, the holograms $\mathbf{h}_\mathrm{s}$ and $\mathbf{h}_\mathrm{f}$ were read by R* (whose electric field was represented by a vector $\mathbf{R}^*$) at t = 50 ms, and the −1st order diffracted light was proportional to $\sum_{\mathrm{i}=0}^{50}\mathbf{b}_\mathbf{i}^*$, and $\mathbf{b}_{\mathbf{50}}^*$, respectively. At this time, the dynamic scattering medium IP was represented by the transmission matrix $\mathbf{T}_{\mathbf{50}}$, so on plane A, the light field distribution $\mathbf{a}_\mathrm{s}^* \propto \mathbf{T}_{\mathbf{50}}^T \sum_{i=0}^{50}\mathbf{b}_\mathbf{i}^*$ for the slow PCM, and $\mathbf{a}_\mathbf{f}^* \propto \mathbf{T}_{\mathbf{50}}{}^T\mathbf{b}_{\mathbf{50}}^* \approx \mathbf{a}^*$ (since $\mathbf{T}_{\mathbf{50}}{}^\dagger\mathbf{T}_{\mathbf{50}} \approx \hat{\mathbf{I}}$) for the fast PCM, where the superscript "T" denotes matrix transpose. It can be seen that $\mathbf{a}_\mathbf{f}^*$ resembles the perfect time-reversed light field $\mathbf{a}^*$. The intensity distributions shown in Fig. 3.1(d)−(e) were calculated by $|\mathbf{a}_\mathrm{s}^*|^2$ and $|\mathbf{a}_\mathbf{f}^*|^2$ with bicubic interpolation.

3.1.2 Results

Tissue-mimicking phantom experiments

Here, we demonstrated TRUE optical focusing inside a dynamic scattering medium composed of an intralipid-gelatin phantom (IP, thickness = 1.5 mm, reduced scattering coefficient = 0.98 mm^{-1}) and a ground glass diffuser. An absorptive target was sandwiched between the two scattering media to mimic an optical heterogeneity, such as a tumor, inside tissue. By translating the IP at different speeds, speckle patterns with different speckle correlation times (τ_c) were created. The set-up illustrated in Fig. 3.4(a) was used to characterize the dependence of the speckle correlation time on the phantom movement speed. As shown, the diffuse light passing through the diffuser and the IP was collected by a lens L, and concentrated onto the photorefractive crystal (PRC). To measure the speckle patterns on the front surface of the PRC, light was reflected by a mirror and directed to a finite-conjugate objective whose object plane was a mirrored plane of the surface of the PRC. When the IP was moved at different speeds along the *x*-axis, the corresponding speckle patterns were magnified by the objective and recorded on a CMOS camera (see Methods). Then, we calculated the correlation coefficients between the first and each of the ensuing frames of the recorded patterns. By fitting the speckle correlation coefficient versus time using a Gaussian function [58, 59], we obtained τ_{c}, defined as the time during which the correlation coefficient decreased to $1/\mathrm{e}^2$ or 13.5%, at a given phantom movement speed. As an example, Fig. 3.4(b) shows the speckle correlation coefficient as a function of time when the phantom was moved at $v = 0.010$ mm s^{-1}, from which $\tau_{\mathrm{c}} = 60$ ms was determined. The relationship between the speckle correlation time and the phantom movement speed is shown in Fig. 3.4(c). Theoretically, $\tau_{\mathrm{c}} = d_{\mathrm{b}} / v$, where d_{b} is the expected size of the speckle grains back-projected from the camera to the surface of the IP through lens L and the objective. From its definition, $d_{\mathrm{b}} = d / (M_1 M_2)$, where M_1 (= 2.8, simulated by Zemax, Zemax, LLC, USA) and M_2 (= 40) are the magnifications of L and the objective, respectively, and *d* is the expected speckle size on the camera ($d = \lambda l / D$, where λ is the optical wavelength, *l* (150 mm) is the distance between L and the PRC, and *D* (75 mm) is the aperture size of L). From the fitted curve in Fig. 3.4(c), $d_{\mathrm{b}} = 0.56 \pm 0.01$ μm ($R^2 = 0.999$), which is close to its theoretical value of $\lambda l / (D M_1)$ = 0.57 μm. The value of τ_{c} at different speeds can therefore be estimated from $\tau_{\mathrm{c}} = 0.56 / v$ [ms] (the unit of *v* is mm s^{-1}), especially when $v > 0.040$ mm s^{-1} (for those speeds, it was impossible to measure τ_c accurately with the current set-up, since the frame rate of the camera was limited to 208 frames per second (fps)).

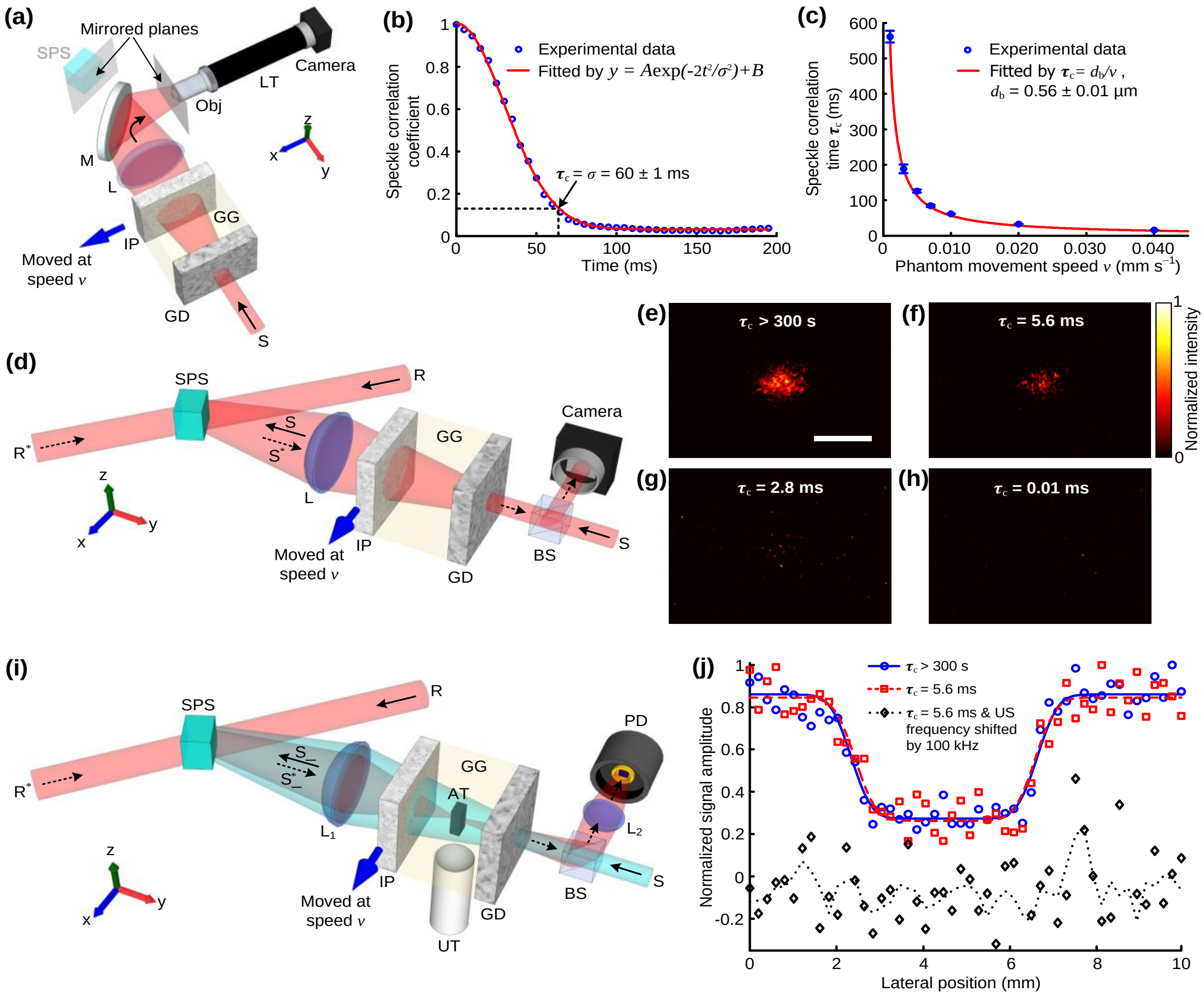

Figure 3.4 TRUE optical focusing inside a dynamic scattering medium containing a tissue-mimicking phantom. (a) Schematic of the set-up for characterizing the relationship between the speckle correlation time (τ_c) and the phantom movement speed. The front surface of the crystal and the object plane of the objective were mirrored planes. (b) The speckle correlation coefficient as a function of time when the phantom was moved at 0.010 mm s^{-1}. τ_c = 60 ms was determined for this speed. (c) The relationship between the speckle correlation time and the phantom movement speed. Error bar shows the standard error of τ_c measured when light illuminated three different locations on the intralipid-gelatin phantom. (d) Schematic of the set-up for evaluating the quality of the time-reversed light at various sample decorrelation rates. (e–g) The time-reversed light pattern when the intralipid-gelatin phantom was static (τ_c > 300 s, (e)), moved at 0.100 mm s^{-1} (τ_c = 5.6 ms, (f)), and at 0.200 mm s^{-1} (τ_c = 2.8 ms, (g)). (h) No time-reversed light was observed when the frequency of S was shifted by 100 kHz (τ_c = 0.01 ms). All the images in (e–h) were normalized by their own maximum values. (i) Schematic of the set-up for imaging an absorptive target with TRUE light. The target was scanned along the *x*-direction. (j) One dimensional images of the target acquired under different conditions. The circles, squares, and diamonds denote experimental data. The solid and dashed lines denote curve fitting of the experimental data. The dotted line denotes the 4-point moving average

of the experimental data. Abbreviations: AT, absorptive target; BS, beamsplitter; GD, ground glass diffuser; GG, gelatin gel; IP, intralipid-gelatin phantom; L, lens; LT, lens tube; M, mirror; Obj, Objective; PD, photodiode; R, reference beam; R^*, reading beam, phase conjugate to R; S, sample light; S_-, frequency-down-shifted sample light (signal light); S_-^*, time-reversed signal light; SPS, $Sn_2P_2S_6$:Te 1% photorefractive crystal; TRUE, time-reversed ultrasonically encoded; US, ultrasound; UT, ultrasonic transducer. Scale bar, 1 mm.

To evaluate the limiting speed of our system in achieving optical phase conjugation, we used the set-up illustrated in Fig. 3.4(d) to directly visualize the time-reversed light patterns at various sample decorrelation rates. The diffuse sample light S passing through the scattering medium interfered with a reference beam R (plane wave, with the same optical frequency as that of S) for 10 ms and wrote a volumetric hologram inside the PRC. Then, S and R were blocked, and a reading beam R^*, conjugate to R, was applied to illuminate the PRC for 2 ms, generating a phase conjugated copy of S, i.e., the time-reversed light S^*, which was monitored by a CMOS camera in real time. The intensity distributions of S^* when the IP was static (τ_c > 300 s), moved at v = 0.100 mm s^{-1} (τ_c = 5.6 ms), and at v = 0.200 mm s^{-1} (τ_c = 2.8 ms) are shown in Figs. 3.4(e)−(g). To quantify the phase conjugation quality, we calculated the ratio R_I between the averaged light intensities within ($\bar{I}_{in}$) and outside ($\bar{I}_{out}$) the targeted region of the phase conjugated light (the region was determined when τ_c > 300 s, as shown in Fig. 3.4(e)). To determine the limiting speed of our system in achieving optical phase conjugation, we identified the shortest speckle correlation time at which $\bar{I}_{in} \geq \bar{I}_{out} + 3\sigma(I_{out})$ was satisfied (where $\sigma(I_{out})$ is the standard deviation of the background light intensity outside the targeted region). Phase conjugation could be achieved when τ_c = 5.6 ms [Fig. 3.4(f)], although at a degraded quality (R_I = 114) compared with that when τ_c > 300 s [Fig. 3.4(e), R_I = 287]. In contrast, when τ_c = 2.8 ms [Fig. 3.4(g)], R_I dropped to 5. Compared with the phase conjugated light pattern when τ_c = 5.6 ms, the diffracted light was much less localized when τ_c = 2.8 ms, and it was coupled into a stronger background, suggesting that the PRC could not produce time-reversed light with good fidelity. When the frequency of S was detuned by 100 kHz (by using acousto-optic modulators, corresponding to τ_c = 0.01 ms), no time-reversed light was observed [Fig. 3.4(h), R_I = 0.7]. This result was expected, since the interference pattern decorrelated at a speed (100 kHz) greater than the response speed of the PRC and the hologram was washed out. The shortest speckle correlation time our system could tolerate defined with $\overline{I}_{in} \geq \overline{I}_{out} + 3\sigma(I_{out})$ was between 2.8 ms and 5.6 ms.

We further demonstrated that TRUE focusing and imaging could be accomplished when τ_c = 5.6 ms using the set-up illustrated in Fig. 3.4(i). In this experiment, light S with a frequency of $f_0 + f_a$ (f_0 was the laser frequency and f_a (3.5 MHz) was a frequency detuning applied by acousto-optic modulators) illuminated the scattering media (see Methods). The frequency of a portion of the diffuse light traversing the ultrasonic focus was down-shifted to f_0 due to the acousto-optic effect [60, 61] (the frequency of the ultrasonic wave was f_a = 3.5 MHz). These photons (the frequency-down-shifted sample light S_-, also called signal light) contributed to a stable hologram in the PRC by interfering with R, whose frequency was also f_0. Thereby, the recorded hologram corresponded to a wavefront emanating from the ultrasonic focus. When the hologram was then read by R^*(with a frequency of f_0), the time-reversed signal light S_-^* was generated and converged back to the acoustic focus. A photodiode was used to sample S_-^* that came out of the diffuser, and the photodiode outputs corresponding to S_-^* light diffracted from the holograms that were recorded when the focused ultrasonic modulation was on and off are shown in Fig. 3.5, when the IP was moved at v = 0.100 mm s^{-1} (τ_c = 5.6 ms). The positive difference between the maximum signal amplitudes at the on and off states confirmed effective TRUE focusing when τ_c = 5.6 ms. Such a positive difference could no longer be observed repetitively when the frequency of the focused ultrasonic modulation was down-shifted by 100 kHz to f_a' = 3.4 MHz (see Fig. 3.5(b)). This result was expected, since the interference pattern of the ultrasonically encoded light and the reference beam decorrelated too fast (at $f_{S-} - f_R$ $= [(f_0 + f_a) - f_a'] - f_0$ $= f_a - f_a'$ = 3.5 MHz – 3.4 MHz = 0.1 MHz, and $f_{S+} - f_R$ $= [(f_0 + f_a) + f_a'] - f_0 = f_a + f_a'$ = 3.5 MHz + 3.4 MHz = 6.9 MHz, where $f_{S-} = (f_0 + f_a) - f_a'$ and $f_{S+} = (f_0 + f_a) + f_a'$ are the down-shifted and up-shifted frequencies of the sample beam due to the focused ultrasonic modulation at f_a'), which caused the hologram to be washed out. We further validated TRUE focusing by imaging an absorptive target, which was sandwiched between the two scattering media and scanned along the *x*-direction with a step size of 0.2 mm. At each scanning position, to make sure that we indeed obtained signals from TRUE light instead of from R* light that was randomly scattered by the PRC due to beam fanning, a signal was obtained by taking the difference between the peak photodiode outputs corresponding to the two hologram recording states (i.e., focused ultrasound on and off) [62-64]. At each scanning position, 20 TRUE focusing procedures (ultrasonic modulation on and off alternately 10 times during hologram recording) were performed to obtain a 10-time-averaged signal, and the TRUE focusing procedures were operated at a repetition rate of 20 Hz. In each TRUE focusing procedure (50.0 ms long), 10.0 ms was used in hologram recording, 0.6 ms was used for completely shutting off the writing beams, 2.0 ms was used in hologram reading, and the remaining 37.4 ms was idle (i.e., ultrasound was turned off, and shutters were closed) to protect the ultrasonic transducer from over-heating by reducing its duty cycle. One dimensional images of the target are shown in Fig. 3.4(j), when the IP was static (τ_c > 300 s) and when it was moved at a speed of 0.100 mm s^{-1} (τ_c = 5.6 ms). The dips in the images represent the absorptive target since it absorbed part of the TRUE light. The image qualities for τ_c = 5.6 ms and τ_c > 300 s are comparable in terms of target position, dimension, contrast and resolution, demonstrating that focusing was achieved inside a dynamic scattering medium with a speckle correlation time as short as 5.6 ms. The resolution of the image obtained from curve fitting was 0.90 mm (see Methods), which was in agreement with the theoretical value of 0.87 mm, as determined by the focal width of the ultrasonic transducer (3.5 MHz, numerical aperture (NA) = 0.25). As a control, when the frequency of the focused ultrasonic modulation was down-shifted by 100 kHz relative to its correct value, the target could not be imaged, as expected.

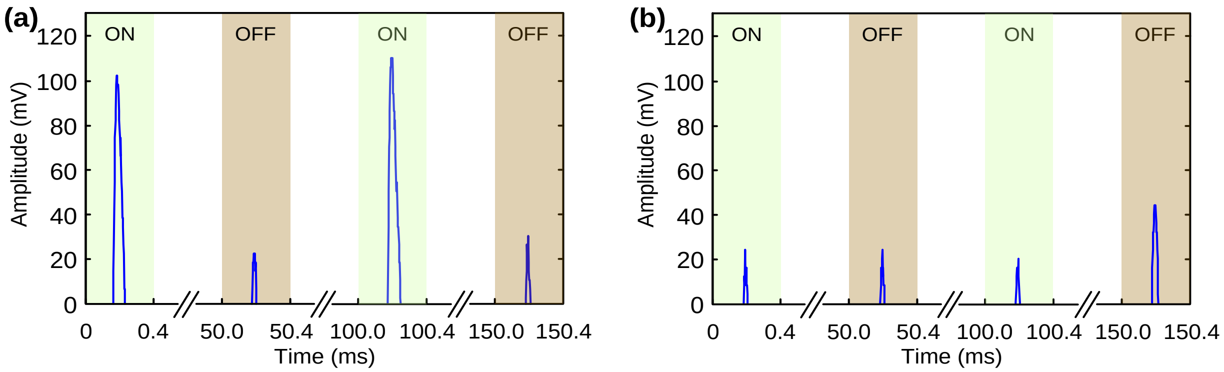

Figure 3.5 Photodiode signal amplitudes of the detected $\mathbf{S}_{-}^{*}$ light diffracted from the holograms that were recorded when the focused ultrasonic modulation was on and off. The frequency of the focused ultrasonic modulation was 3.5 MHz (equal to the difference between the frequency of the light that illuminated the sample and the frequency of the reference beam) in (a), and shifted to 3.4 MHz in (b). A constant offset was subtracted in both figures.

Living tissue experiments

The capability of our system to tolerate fast speckle decorrelation ($\tau_c \geq$ 5.6 ms) paves the way to achieving TRUE optical focusing even when the scattering medium is living tissue whose speckle correlation time is on the order of 1 ms, depending on the depth of interest. A 350-µm-thick living-mouse ear (which comprises two skin layers that are fed by separate blood and lymphatic circulations, with a cartilage layer sandwiched in the middle) was used in our experiments. The optical thickness of the mouse ear, defined as the negative natural logarithm of the fraction of unscattered light, was measured to be 17.4 ± 0.1 (see Methods), so the power of the ballistic light component is negligible compared with the total light power (ratio $< 2.8 \times 10^{-8}$). In addition, no optical focus could be observed by directly focusing light through a living-mouse ear with a microscope objective (Fig. 3.6).

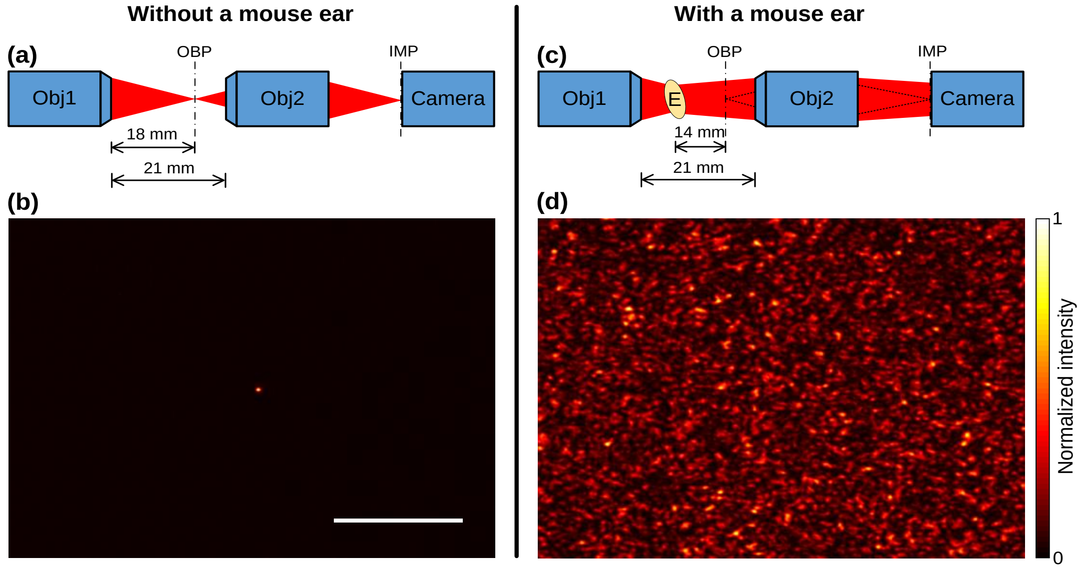

Figure 3.6 Light intensity distributions on the focal plane of an objective (Obj1) before and after a living-mouse ear was inserted as a scattering medium. (a) The experimental set-up. The focal plane of objective 1 (AC080-020-B-ML, Thorlabs Inc., USA. Working distance = 18 mm, NA = 0.2) was imaged by objective 2 (Leica, E1 ACHRO, 10×, NA = 0.25) and a CMOS camera (FMVU-03MTM, Point Grey, Canada). (b) The light intensity distribution on the focal plane of objective 1. The full width at half maximum focal spot size was 2.4 µm on the object plane, which was close to the diffraction-limited focal spot size (2.0 µm). (c) A living-mouse ear (E) was inserted between objective 1 and its focal plane. The distance between the mouse ear and the focal plane was 14 mm, which was the same as the distance between the mouse ear and the ultrasonic focus in the TRUE focusing experiment illustrated in Fig. 3.7(c). (d) The light intensity distribution on the focal plane of objective 1. The focus in (b) could no longer be observed due to scattering of the mouse ear. Abbreviations: E, mouse ear; IMP, image plane; Obj, objective; OBP, object plane. Scale bar, 1 mm.

We first measured the speckle correlation time of the ear of a living mouse under normal anesthesia (see Methods). A sequence of speckle patterns was recorded at 30 fps, from which the speckle correlation coefficient was computed and is shown as a function of time in Fig. 3.7(a). The movie shows a fast-decorrelating speckle pattern on top of a slowly-decorrelating background speckle pattern (see Supplementary notes for a detailed analysis). The background speckle pattern, presumably mainly formed by photons not scattered by blood, translated 0.64 μm back and forth every 800 ms with a duration of 65 ms, due to the breathing of the mouse. The fast-decorrelating speckle pattern, on the other hand, was possibly mainly formed by photons scattered by blood. To validate this hypothesis, we recorded speckle patterns before and after blocking the blood flow in the mouse ear and employed a faster sCMOS camera (with a frame rate of 2271 fps at 160×38 resolution) to measure the speckle correlation time. The speckle correlation coefficients for five different locations on the mouse ear were computed from movies and are shown as a function of time in Fig. 3.7(b). The value of τ_c determined thereby ranges from less than 0.44 ms (limited by the camera's frame rate) to 10 ms, depending on the measurement position. Given that τ_c can be estimated by [58, 65] $\tau_c \approx \lambda / v$, where λ is the wavelength of light and v is the blood flow speed, the range of τ_c is in accordance with the fact that the flow speed in a mouse ear can range from 0.11 mm s^{-1} in capillaries [66] to 5.0 mm s^{-1} in arteries [67]. Once the blood flow was blocked by pressing the ear against a stiff acrylic wall with a metal bar (Fig. 3.3), τ_c became much larger (> 500 ms, see the top, almost flat curve in Fig. 3.7(b)), confirming that the fast speckle decorrelation was due to the light scattered by blood.

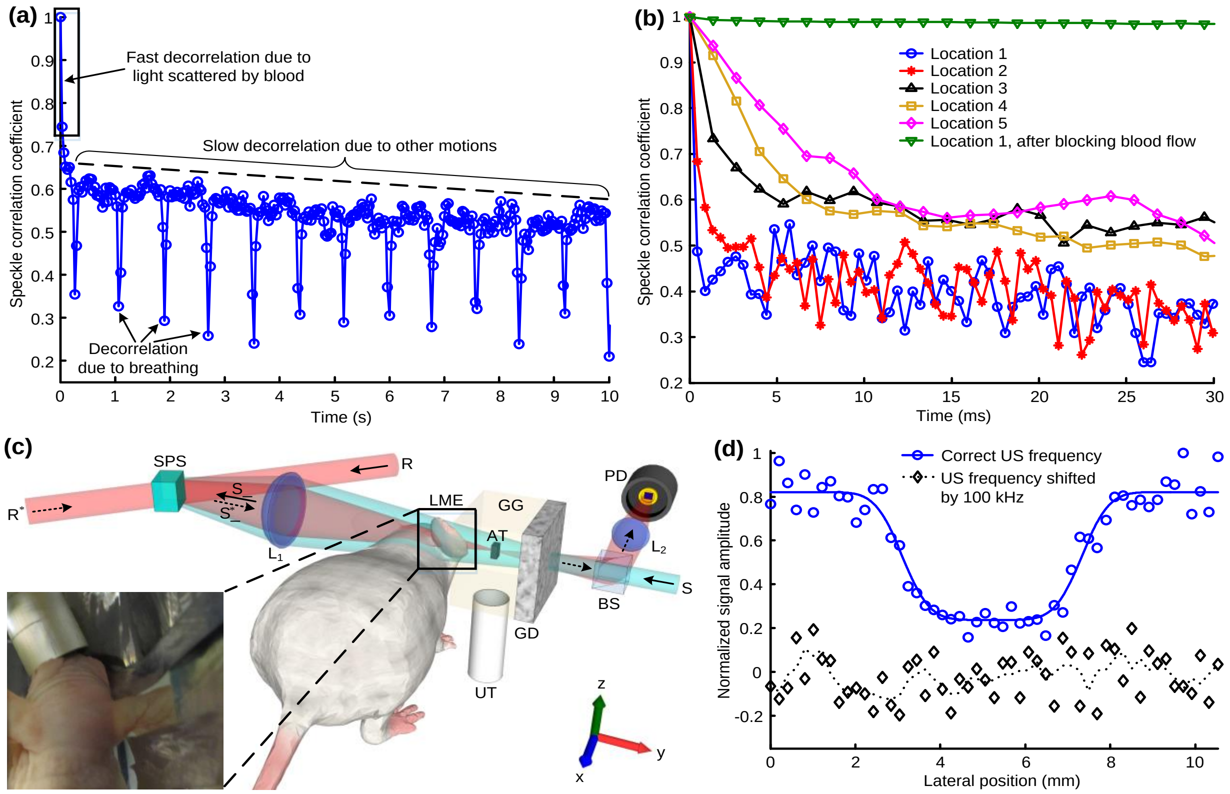

Figure 3.7 TRUE optical focusing inside a dynamic scattering medium containing a living-mouse ear. (a) The speckle correlation coefficient as a function of time for a living-mouse ear. Three speckle decorrelation characteristics were identified. (b) The speckle correlation curves measured at five locations on the mouse ear. The speckle correlation time (τ_c) determined from the curves ranged from less than 0.44 ms to 10 ms. When the blood flow was blocked, τ_c became much larger. (c) Schematic of the set-up for imaging an absorptive target placed between a living-mouse ear and a diffuser. The target was scanned along the *x*-direction. Inset: a photo showing the right ear of a mouse used as a dynamic scattering medium. The left ear was bent downward to avoid blocking the light. Aluminum foil tapes were used to block the light that did not pass through the right ear. (d) One dimensional images of the absorptive target. The circles and diamonds denote experimental data. The solid line denotes curve fitting of the experimental data. The dotted line denotes the 4-point moving average of the experimental data. Abbreviations: AT, absorptive target; BS, beamsplitter; GD, ground glass diffuser; GG, gelatin gel; L, lens; LME, living-mouse ear; PD, photodiode; R, reference beam; R^*, reading beam, phase conjugate to R; S, sample light; S_-, frequency-down-shifted sample light (signal light); S_-^*, time-reversed signal light; SPS, $Sn_2P_2S_6$:Te 1% photorefractive crystal; TRUE, time-reversed ultrasonically encoded; UT, ultrasonic transducer.

TRUE optical focusing was further demonstrated by imaging an absorptive target embedded between the living-mouse ear and a ground glass diffuser [Fig. 3.7(c)]. By scanning the target along the *x*-direction and monitoring the transmitted TRUE light power at each scanning position, a one-dimensional image of the target was obtained, as shown in Fig. 3.7(d). The target is clearly revealed as a dip with an image resolution of 1.1 mm determined from the curve fitting, which is reasonably close to the size of the ultrasonic focus. As a control, when the frequency of the focused ultrasonic modulation was down-shifted by 100 kHz relative to its correct value, the target could not be imaged, as expected. In these experiments, we applied the same averaging scheme as in the phantom experiments. To push the imaging speed, TRUE focusing procedures were operated at 132 Hz at each scanning position, and the transducer ran at a much higher duty cycle than it ran in the experiments with phantoms. The shutters were operated in burst mode. In each TRUE focusing procedure (7.6 ms), 5.0 ms was used in hologram recording, 0.6 ms was used for completely shutting off the writing beams, and 2.0 ms was used in hologram reading. The intensity of the reference beam was 1.0 W cm^{-2} in the dynamic phantom experiment and 1.8 W cm^{-2} in the living tissue experiment. In both cases, the intensity of the sample light on the crystal was about 7 times weaker. We tested different power splitting ratios between the sample beam and the reference beam, and determined the optimum intensity ratio (1:8) by maximizing the time-reversed signal strength. So far, we have not found a satisfactory theoretical explanation of the optimum intensity ratio.

3.1.3 Discussion and Conclusion

Optical focusing at depths beyond one transport mean free path inside living biological tissue is one of the most challenging goals in biomedical optics. The focusing speeds of previous wavefront shaping systems are far too low for *in vivo* applications where the fast speckle decorrelation caused by living tissue needs to be overcome. In this study, we improved the speed of focusing light deep inside scattering media by one to two orders of magnitude, and provided the first demonstration of using TRUE light to focus inside a dynamic scattering medium comprising living tissue. Since our system uses a near-infrared wavelength, it has the potential to focus light deep inside tissue due to the weaker optical attenuation.

The speckle size on the PRC in the dynamic phantom experiment was measured to be 1.6 µm, so the number of optical modes accommodated by the PRC was estimated to be $(A/d)^2 = (6\times10^3/1.6)^2 = 1.4\times10^7$ (where A = 6 mm is the area of the front surface of the PRC and d = 1.6 µm is the speckle size on the PRC), which is 22 times more than that can be accommodated by a state-of-the-art SLM (1920×1280 pixels) used in digital TRUE focusing systems or wavefront shaping techniques. The large number of optical modes, N, controlled by our system, enables a more complete phase conjugation [30] and a focus with a higher peak to background ratio [15, 31, 63] (PBR = $(N+1)/M$, where M is the number of optical modes inside the focus) under the same experimental condition. It will take ~1.9×10^3 s to handle the same number of optical modes even using the fastest implementations demonstrated in wavefront shaping [68, 69] (although the number of pixels in a digital micromirror device (DMD) [68] or a micro-electro-mechanical systems (MEMS) deformable mirror [69] is far less than 1.4×10^7), which is 1.5×10^5 times less than the focusing speed of our system. A large N is desired to achieve a sufficient PBR in deep tissue because M can be as large as $\sim\left[\lambda_\mathrm{a}/(\lambda/2/n)\right]^2$ = [150 µm/(0.8 µm/2/1.33)]^2 = 2.5×10^5 in the acoustic-wave-guided wavefront shaping (assuming a 10 MHz ultrasonic wave whose wavelength λ_a is 150 µm, an optical wavelength λ of 0.8 µm in vacuum, a refractive index n of 1.33 for water in biological tissue, and fully-developed speckles).

In the dynamic phantom experiment, we determined the optimum hologram writing time (10 ms) by maximizing the signal-to-noise ratio when τ_c = 5.6 ms. The shorter speckle correlation time seems to contradict the fact that time-reversal could still be achieved, which, however, can be explained as follows. Although the recorded hologram was partially blurred, it could be decomposed into a correct hologram and an incorrect one. The correct hologram generated a TRUE focus, while the incorrect one produced a background. For the background, light energy was broadly distributed in space so that the intensity was much lower than that in the TRUE focus. Since the hologram writing time was only 79% longer than τ_{c} and 43% longer than the response time of the PRC [51, 70] (7 ms at 1 W cm^{-2}), the correct hologram still prevailed, forming a TRUE focus (see the simulation results in Fig. 3.8 and Supplementary notes).

In the experiment with living tissue, the light intensity on the mouse ear was 0.42 W cm^{-2}, which is close to the American National Standards Institute (ANSI) safety limit around 793 nm (0.30 W cm^{-2}). No apparent damage was observed in the tissue after the experiment. It is also worth noting that the ANSI safety limit is usually 10 times below the real damage threshold. Nevertheless, we could further decrease the light intensity on the tissue to meet the standard.

By recording the speckle patterns of the light passing through the living-mouse ear, we found that some part of the pattern (mainly formed by blood-scattered light) decorrelated fast (τ_{c} ranged from less than 0.44 ms to 10 ms), while the rest (mainly formed by non-blood-scattered light) decorrelated slowly ($\tau_{\mathrm{c}} > 60$ s, when the motion of the ear due to breathing was suppressed by a home-made immobilization set-up, which gently pressed the ear using two microscope slides). Since the response time of the PRC is inversely proportional to the illuminating light intensity and the intensity was higher on the PRC in the living tissue experiment than that in the dynamic phantom experiment, we expect our system to have achieved TRUE focusing when τ_{c} was less than 5.6 ms in the living tissue experiment. Considering the range of τ_{c} of a living-mouse ear, we reasoned that most of the non-blood-scattered photons and part of the blood-scattered photons impinging on the PRC were time-reversed back to the acoustic focus. Cui *et al.* reported light transmission through (as opposed to focusing inside) a living rabbit ear by optical phase conjugation and measured the speckle correlation time to be 1.5 s [71]. Considering the speed of their system, we believe they time-reversed only the photons that were not scattered by blood, which formed a quasi-static speckle pattern on the camera. For thicker tissue, however, the number of photons that are not scattered by blood becomes smaller, and the photons that are multiply-scattered by blood tend to result in a faster decorrelating speckle pattern [72]. In order to achieve TRUE focusing in these situations, higher speed is needed. To this end, one may boost the reference beam intensity to further decrease the PRC's response time, which, however, may decrease the TRUE signal amplitude due to a non-optimum intensity ratio between the reference beam and the signal beam on the PRC, once the intensity of the sample beam is limited by the ANSI safety limit. Alternatively, one may employ faster PRCs, such as GaAs [73].

In the future, to achieve TRUE focusing inside thick tissue, we plan to implement the system in a reflection configuration [62], where light is illuminated and detected on the same side of the tissue. For applications such as phototherapy or multi-photon imaging, where large energy or power deposition is needed, it is important to add gain to the TRUE light. Nevertheless, even without gain, it has been shown that there is enough TRUE light to achieve single-photon fluorescence imaging [63] deep inside scattering media.

To conclude, we focused diffuse light inside a dynamic scattering medium containing either a tissue-mimicking phantom or living tissue. Our system can tolerate rapid speckle decorrelation on the scale of 5.6 ms. Because the demonstrated focusing speed approaches the tissue decorrelation rate, this work is an important step toward *in vivo* deep tissue optical imaging, manipulation, optogenetics and phototherapy.

3.1.4 Supplementary notes

Remarks on the speckle patterns formed by light passing through a living-mouse ear.

The light intensity at each position on the camera has contributions from both blood-scattered photons and non-blood-scattered photons. So, the output of each pixel of the camera, $V(\vec{r},t)$, can be expressed as:

$$V(\vec{r},t) \propto \int_{t-T/2}^{t+T/2} \left|E(\vec{r},\tau)\right|^2 d\tau = \int_{t-T/2}^{t+T/2} \left|\tilde{E}_{\mathrm{s}}(\vec{r})\exp(-i\omega\tau) + \tilde{E}_{\mathrm{d}}(\vec{r},\tau)\exp(-i\omega\tau)\right|^2 d\tau .$$

Here, $\tilde{E}_{\mathrm{s}}(\vec{r})$ is the complex amplitude of the net electric field (E-field) of non-blood-scattered light at position $\vec{r}$, which does not change over time; $\tilde{E}_{\mathrm{d}}(\vec{r},\tau)$ is the complex amplitude of the net E-field of blood-scattered light at position $\vec{r}$ and time τ; ω is the frequency of the laser light; and T is the camera's exposure time. The intensities of the bright speckle grains in the seemingly-static background pattern fluctuate over time at small amplitudes, which can be explained as follows. In these speckle grains, the phasor $\tilde{E}(\vec{r},t) = \tilde{E}_{\mathrm{s}}(\vec{r}) + \tilde{E}_{\mathrm{d}}(\vec{r},t)$ is a vector sum of a large constant vector in the complex plane and a small vector which rotates randomly over time and changes its length. Since $\left|\tilde{E}_{\mathrm{s}}(\vec{r})\right|$ is much larger than $\left|\tilde{E}_{\mathrm{d}}(\vec{r},t)\right|$, the resulting amplitude of the phasor $\tilde{E}(\vec{r},t)$ can be approximated by $\left|\tilde{E}_{\mathrm{s}}(\vec{r})\right|$, thus the intensity $I(\vec{r},t)$ appears to be constant in these speckle grains.

Simulation of TRUE optical focusing inside a dynamic scattering medium with a speckle correlation time of 5.6 ms.

Similar to the procedures described in Methods, the E-field of the ultrasonically encoded light on the PRC can be calculated by $\mathbf{b} = \mathbf{Ta}$, where $\mathbf{T}$ is the transmission matrix (dimension = 625 ×

625) and $\mathbf{a}$ is the ultrasonically encoded light field (dimension = 625×1) on the *x*-*z* plane intersecting the acoustic axis (denoted as plane A, see Fig. 3.1(a)). In our phantom experiment, since the speckle pattern $|\mathbf{b}|^2$ had a speckle correlation time (τ_c) of 5.6 ms when the phantom was moved at 0.100 mm/s, we simulated 11 transmission matrices $\mathbf{T_i}$ (i = 0, 1, 2,$\cdots$, 10, representing the scattering medium at the time of *i* ms), whose elements $\left[\mathbf{T_i}\right]_{jk}$ were correlated because they were sampled from 9-point moving averaging of a sequence of random complex numbers. Specifically, $[\mathbf{T_i}]_{jk} = \sum_{p=i-4}^{p=i+4} [\mathbf{M_p}]_{jk} / 9$ (i = 0, 1, 2,$\cdots$, 10), where $\mathbf{M_p}$ (p = −4, −3, $\cdots$, 14) are 19 independent random matrices whose elements follow the circular Gaussian distribution, and $\mathbf{M_p} \mathbf{M_p^\dagger} \approx \hat{\mathbf{I}}$, where "$\dagger$" denotes conjugate transpose and $\hat{\mathbf{I}}$ is the identity matrix. The speckles at different time, $\mathbf{b_i} = \mathbf{T_i a}$, were correlated with a τ_c = 5.2 ms (see Figs. 3.8(a)–(b)), similar to the measured value (τ_c = 5.6 ms) in our experiments. $\mathbf{b_i}$ interfered with a reference beam R (whose E-field was represented by a vector $\mathbf{R}$ (dimension = 625×1) in which all elements were 1) and formed an interference pattern $\mathbf{I_i} = |\mathbf{b_i} + \mathbf{R}|^2$. The hologram recorded within the writing time (t_w = 10 ms) was proportional to a weighted summation of $\mathbf{I_i}$ (see Fig. 3.8(d)) as in:

$$\mathbf{h}_{\mathbf{t_w}} = \mathbf{h}(t = t_\mathrm{w} = 10\ \mathrm{ms}) \propto \int_0^{t=10\ \mathrm{ms}} \mathbf{I}(\mathrm{t} - \tau) \exp(-\tau / \tau_\mathrm{r})\, \mathrm{d}\tau \approx \sum_{i=0}^{10} |\mathbf{b_i} + \mathbf{R}|^2 w_i,$$

$$w_i = \exp\left[-(10 - i) / \tau_\mathrm{r}\right].$$

Here, τ_r = 7 ms is the response time of the PRC at 1 W cm^{-2}. If the response time of the PRC was much shorter than τ_c, $\mathbf{h}(t$ = 10 ms$) \triangleq \mathbf{h_{Correct}} \propto \mathbf{I_{10}}$ (see Fig. 3.8(c)). It can be seen that although $\mathbf{h}_{\mathbf{t_w}}$ was partially blurred compared with $\mathbf{h}_{\mathbf{Correct}}$, it was still highly correlated with $\mathbf{h}_{\mathbf{Correct}}$ (r = 0.74). $\mathbf{h}_{\mathbf{t_w}}$ could be further decomposed into $\mathbf{h}_{\boldsymbol{\tau}_\mathbf{c}}$ and $\mathbf{h}_{\mathbf{Wrong}}$. $\mathbf{h}_{\boldsymbol{\tau}_\mathbf{c}} \propto \sum_{i=5}^{10} \left|\mathbf{b_i} + \mathbf{R}\right|^2 w_i$ was the hologram integrated over a duration of τ_c starting at time $t_\mathrm{w} - \tau_\mathrm{c}$. Compared with $\mathbf{h}_{\mathbf{t_w}}$, $\mathbf{h}_{\boldsymbol{\tau}_\mathbf{c}}$ was expected to resemble $\mathbf{h}_{\mathbf{Correct}}$ more closely due to reduced blurring (r = 0.81, see Fig. 3.8(e)). $\mathbf{h}_{\mathbf{Wrong}} \propto \sum_{i=0}^{4} \left|\mathbf{b_i} + \mathbf{R}\right|^2 w_i$ was the hologram integrated from time 0 to $t_\mathrm{w} - \tau_\mathrm{c}$. Since $\mathbf{b_i}$ (i = 0 – 4) was poorly correlated with $\mathbf{b_{10}}$, $\mathbf{h}_{\mathbf{Wrong}}$ was expected to be poorly correlated with $\mathbf{h}_{\mathbf{Correct}}$ (r = 0.12, see Fig. 3.8(f)).

In the time-reversal step, the hologram $\mathbf{h}_{\mathbf{t_w}}$ was read by a reading beam R^* (whose E-field was represented by a vector $\mathbf{R}^*$) at t = 10 ms, and the −1st order diffracted light was generated, which was proportional to $\sum_{i=0}^{10} \mathbf{b}_\mathbf{i}^* w_i$. At this time, the dynamic scattering medium (i.e. the intralipid-gelatin phantom) was represented by the transmission matrix $\mathbf{T_{10}}$, and the light field distribution on plane A in Fig. 3.1(a), $\mathbf{a}_{\mathbf{t_w}}^*$, was proportional to $\mathbf{T}_{\mathbf{10}}^T \sum_{i=0}^{10} \mathbf{b}_\mathbf{i}^* w_i$ (see Fig. 3.8(h) for the intensity distribution $\left|\mathbf{a}_{\mathbf{t_w}}^*\right|^2$), where the superscript "T" denotes matrix transpose. If $\mathbf{h}_{\mathbf{Correct}}$ was read, the field distribution on plane A, $\mathbf{a}_{\mathbf{Correct}}^*$, was proportional to $\mathbf{T_{10}}^T \mathbf{b}_{\mathbf{10}}^* \approx \mathbf{a}^*$ (assuming $\mathbf{T_{10}}^\dagger \mathbf{T_{10}} \approx \hat{\mathbf{I}}$), representing the ideal TRUE focus (see Fig. 3.8(g) for $\left|\mathbf{a}_{\mathbf{Correct}}^*\right|^2$). The background in $\left|\mathbf{a}_{\mathbf{Correct}}^*\right|^2$ was due to partial time-reversal[2] (i.e. not all the output modes were detected and time-reversed). Compared with $\left|\mathbf{a}_{\mathbf{Correct}}^*\right|^2$, there was a stronger background in $\left|\mathbf{a}_{\mathbf{t_w}}^*\right|^2$. This elevated background could be better understood by studying the readout of the hologram $\mathbf{h}_{\tau_c}$ and $\mathbf{h}_{\mathbf{Wrong}}$ ($\mathbf{h}_{\mathbf{t_w}} = \mathbf{h}_{\tau_c} + \mathbf{h}_{\mathbf{Wrong}}$), simulated by $\mathbf{a}^*_{\tau_c} \propto \mathbf{T_{10}}^T \sum_{i=5}^{10} \mathbf{b}_{\mathbf{i}}^* w_i$ and $\mathbf{a}^*_{\mathbf{Wrong}} \propto \mathbf{T_{10}}^T \sum_{i=0}^{4} \mathbf{b}_{\mathbf{i}}^* w_i$, respectively (see Figs. 3.8(i)−(j) for the intensity distributions $\left|\mathbf{a}^*_{\tau_c}\right|^2$ and $\left|\mathbf{a}^*_{\mathbf{Wrong}}\right|^2$). It can be seen that the little-blurred hologram $\mathbf{h}_{\tau_c}$ generated a TRUE focus with good fidelity, while the incorrect hologram $\mathbf{h}_{\mathbf{Wrong}}$ generated a background $\left|\mathbf{a}^*_{\mathbf{Wrong}}\right|^2$ with no focus. For the background $\left|\mathbf{a}^*_{\mathbf{Wrong}}\right|^2$, the energy of light was broadly distributed in space so that the intensity at each position was much lower than the intensity in the TRUE focus in $\left|\mathbf{a}^*_{\tau_c}\right|^2$. Because of this, the background in $\left|\mathbf{a}^*_{\mathbf{t_w}}\right|^2$ is only slightly stronger than the background in $\left|\mathbf{a}^*_{\mathbf{Correct}}\right|^2$, and thus the quality of the TRUE focus in $\left|\mathbf{a}^*_{\mathbf{t_w}}\right|^2$ is comparable with that in $\left|\mathbf{a}^*_{\mathbf{Correct}}\right|^2$ ($r = 0.93$).

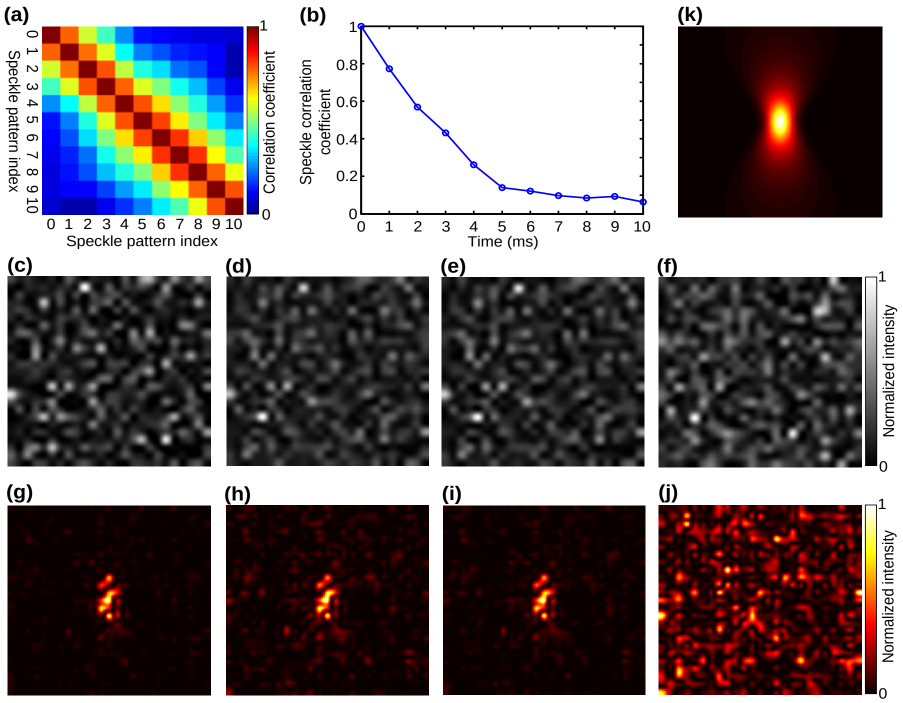

Figure 3.8 Simulation of TRUE optical focusing inside a dynamic scattering medium with a speckle correlation time of 5.2 ms. (a) The correlation coefficients between different speckle patterns. The i^{th} speckle pattern is the speckle

pattern on the PRC (formed by signal light S_-) at the time of *i* ms. (b) The correlation coefficients between the speckle pattern at 0 ms, and each of the ensuing speckle patterns, from which τ_c = 5.2 ms was determined. (c) The correct hologram formed by the interference between S_- and the reference beam R at 10 ms. The partially blurred hologram within the hologram writing time (10 ms) (d) can be decomposed into a partially blurred hologram within τ_c ((e), formed by the integration of the interference patterns between the S_- and R at 5 – 10 ms) and an incorrect hologram ((f), formed by the integration of the interference patterns between S_- and R at 0 – 4 ms). (g)–(j) The light intensity distributions on Plane A (i.e., the *x*-*z* plane intersecting the acoustic axis in Fig. 3.1(a)) when the corresponding holograms in (c)−(f) were read. (k) The ultrasonic modulation efficiency distribution. All the images were normalized by their own maximum values.

3.2 High-speed digital TRUE focusing based on a lock-in camera with improved bit-efficiency

3.2.1 Introduction

In previous digital TRUE focusing systems, a conventional camera records four interference patterns that are transferred to a computer to calculate the wavefront of ultrasonically tagged light (a method known as phase-shifting holography [74]). The conventional camera is highly inefficient in its use of bits and limits the speed of wavefront measurement, which can be understood as follows. To measure the wavefront of ultrasonically tagged light using phase-shifting holography, a camera records the light patterns formed by a planar reference beam (R), ultrasonically tagged light (T), and untagged light (U) at a frame rate of $4f_b$ [Figs. 3.9(a), (b)], when T and R beat at a frequency of f_b. The averaged light intensity recorded by each camera pixel can be expressed as $I(\vec{r},t) = I_R + I_T(\vec{r}) + I_U(\vec{r}) + 2\sqrt{I_R I_T(\vec{r})}\cos\left[2\pi f_b t + (\varphi_T(\vec{r}) - \varphi_R)\right]$. Here, I_R, I_T and I_U are the intensities of R, T, and U, respectively; φ_T and φ_R are the phases of T and R. In general, when a scattering sample is dynamic, I_T, I_U, and φ_T also depend on time. They can be treated as time-independent quantities, however, if the measurement is done before the speckle decorrelates, $I(\vec{r},t)$ can also be decomposed as $I(\vec{r},t) = I_{DC}(\vec{r}) + S_{AC}(\vec{r},t)$ [Fig. 3.9(c)], where $I_{DC}(\vec{r}) = I_R + I_T(\vec{r}) + I_U(\vec{r})$ and $S_{AC}(\vec{r},t) = 2\sqrt{I_R I_T(\vec{r})}\cos\left[2\pi f_b t + (\varphi_T(\vec{r}) - \varphi_R)\right]$. $S_{AC}(\vec{r},t)$ is related to the phase map $\varphi_{\mathrm{T}}(\vec{r})$ that we want to measure, and it oscillates at a frequency of f_{b}, while $I_{\mathrm{DC}}(\vec{r})$ is a static background that does not contain useful phase information. Therefore, the signal-to-background ratio (SBR), or modulation depth, can be expressed as SBR $= \mathrm{amp}(S_{\mathrm{AC}}) / I_{\mathrm{DC}} = 2\sqrt{I_{\mathrm{R}} I_{\mathrm{T}}} \big/ (I_{\mathrm{R}} + I_{\mathrm{T}} + I_{\mathrm{U}})$, where $\mathrm{amp}(\cdot)$ denotes taking the amplitude. When the targeted focusing location is deep inside a scattering medium and a high-frequency ultrasonic transducer is used for a small focal volume, due to the large amount of untagged light compared with tagged light, the SBR can be extremely low. For example, in a simulation of focusing 10 mm deep inside chicken breast, using a 50-MHz transducer and 800-nm laser illumination, the SBR was found to be $\sim 10^{-4}$ [75]. So, to measure the phase map $\varphi_{\mathrm{T}}(\vec{r})$ using phase-shifting holography, a high dynamic range camera has to be used. When the SBR is lower than 10^{-4}, even with a 16-bit analog-to-digital converter (ADC), no more than 3 bits of a pixel value can be used to represent the signal (S_{AC}), while most of the bits are wasted in representing the informationless background (I_{DC}). Besides this low efficiency in the use of bits, all 16-bit data, including both the signal and the background, are transferred to a computer, which increases the data transfer load [Fig. 3.9(d)]. Even worse, phase-shifting holography needs to record and transfer at least four frames of images to calculate the phase map on a computer, so the speed of wavefront determination is severely limited by the low frame rates of conventional cameras (typically < 700 Hz with 300 × 300 pixels) and the heavy load during data transfer. When averaging is needed, even more frames need to be recorded and transferred, so it takes seconds to acquire a phase map (with 1920 × 1080 pixels) before time-reversed focusing can be performed in previous works [30, 31, 76, 77]. To apply this technique *in vivo*, systems with higher speeds are strongly desired to accommodate the fast speckle decorrelation (on a time scale from 0.1 ms to 1 ms) primarily due to blood flow [24].

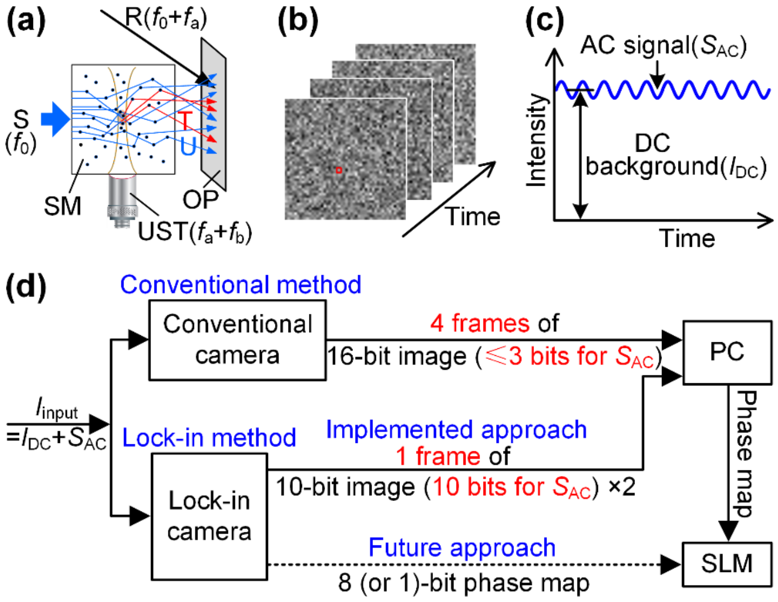

Figure 3.9 A comparison of using a conventional camera and using a lock-in camera to achieve TRUE optical focusing. (a) Illustration of different components of light that are detected by a camera. f_0, laser frequency; f_a, frequency of ultrasonic transducer; f_b, beat frequency between R and T; OP, the object plane imaged by a camera to measure the wavefront of ultrasonically tagged light; R, reference beam; S, sample beam; SM, scattering medium; T, ultrasonically tagged light, which has a frequency of $f_0 + f_a + f_b$; UST, ultrasonic transducer; U, untagged light, which is not modulated by ultrasound and whose frequency is f_0. (b) The light intensity patterns on plane OP at various times. (c) Light intensity as a function of time for the pixel denoted by the red square in (b). A small AC signal (with a frequency of f_b) sits on a very large DC background. (d) A comparison between using a conventional camera and using a lock-in camera to achieve TRUE focusing. The wavefront of ultrasonically tagged light is measured by phase-shifting holography or our lock-in method, then the conjugate phase map is displayed on a phase-only spatial light modulator (SLM) to phase conjugate the ultrasonically tagged light T back to the ultrasonic focus. PC, personal computer.

3.2.2 Methods

Here, we developed a wavefront measurement method based on a lock-in camera [78, 79] (heliCam C3, Heliotis; 300 × 300 pixels; 40 μm pixel size), in which each pixel performs analog lock-in detection and outputs only the information of the AC signal (S_{AC}) at up to 3800 frames per second to an on-chip memory. Specifically, the lock-in circuitry generates the in-phase ($S_I(r) \propto 2\sqrt{I_R I_T(\vec{r})}\sin[(\varphi_T(\vec{r})-\varphi_R+\pi/4)]$) and the quadrature ($S_Q(r) \propto 2\sqrt{I_R I_T(\vec{r})}\cos[(\varphi_T(\vec{r})-\varphi_R+\pi/4)]$) components of the AC signal oscillated at the frequency of f_b, which are then digitized by a 10-bit ADC. Since only the information of the AC signal, not that of the DC background, is digitized, the lock-in camera tremendously increases the bit efficiency by using all the bits to represent the signal, and it enables the use of inexpensive low-resolution ADCs. Moreover, compared with the previous method that needs to record and transfer 4 frames, our approach can obtain the desired phase map after only a single frame of measurement taken within 0.3 ms. It also reduces the amount of data to transfer by transferring only one frame of the information of the signal, instead of 4 frames of raw images composed of both the signal and the background.

The lock-in camera has two related output modes [Fig. 3.9(d)]. In Mode A, S_I and S_Q for each pixel are transferred to a computer via a USB 2.0 interface. In Mode B, the desired phase map, $\varphi_\mathrm{T}(\vec{r})-\varphi_\mathrm{R}+\pi/4$, calculated by an on-chip field-programmable gate array (FPGA) is directly transferred to a computer using the same interface. Compared with Mode A, Mode B minimizes the amount of data to transfer and removes the need for a computer to calculate the phase map, therefore it is ideal for high-speed TRUE focusing systems. However, since our camera is designed for full-field optical coherence tomography applications, Mode B outputs some other data irrelevant for our applications, transferring more data than Mode A. Because the speed is currently limited by the data transfer rate of USB 2.0, we chose to use Mode A. In all our experiments, a planar reference beam was shined normal to the surface of the camera, so φ_R was approximately a position-independent constant. f_b was experimentally optimized to 70 kHz for maximum sensitivity. The lock-in camera locked-in 20 cycles of the beat signal at frequency f_b, and output one frame of data comprising S_I and S_Q for each pixel. The phase map was calculated on a computer by $\varphi_\mathrm{T}(\vec{r})$ = arg($S_\mathrm{I}/S_\mathrm{Q}$) based on the data from a single frame measured within 0.3 ms. Here, arg(·) denotes taking the argument, and the uniform phase offset $-\varphi_\mathrm{R}+\pi/4$ has been dropped.

3.2.3 Results

We tested the lock-in camera by measuring two standard wavefronts. A continuous-wave laser at 532 nm (Verdi V5, Coherent) was used in all our experiments. For a plane wave with an incidence angle of −5’ relative to the z axis [Fig. 3.10(a)], the measured phase map is shown in Fig. 3.10(b), which represents a plane wave at oblique incidence. For a spherical wave generated by lens focusing [Fig. 3.10(c)], the measured phase map shows concentric rings, as expected [Fig. 3.10(d)]. The less-obvious ghost rings surrounding the central rings are due to the spatial aliasing effect, since the widths of the concentric rings become narrower than the pixel size of the lock-in camera beyond a certain radius.

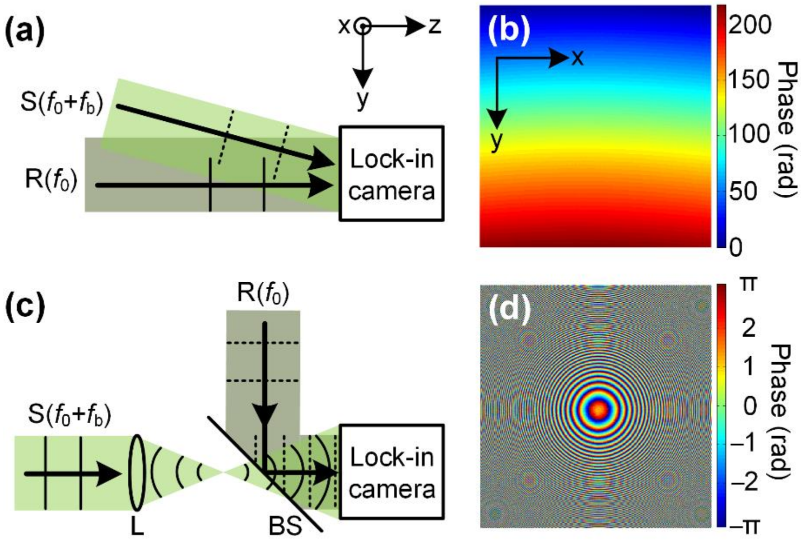

Figure 3.10 Two standard wavefronts measured by the lock-in camera. (a) Schematic of the set-up to measure the wavefront of an oblique incident plane wave, and (b) the measured phase map. (c) Schematic of the set-up to measure the wavefront of a spherical wave, and (d) the measured phase map. BS, beamsplitter; f_0, laser frequency; f_b, beat frequency between R and S; R, reference beam, whose frequency is f_0; S, sample beam, whose frequency is f_0+f_b.

To characterize the phase sensitivity of the lock-in camera as a function of SBR, we used the camera to measure the spatial light modulator (SLM) encoded wavefront of a sample beam (S).

The intensity ratio between the sample beam (I_S) and the reference beam (I_R) was controlled by inserting neutral density filters with different transmittances in the sample beam [Fig. 3.11(a)]; $\mathrm{SBR} = 2\sqrt{I_S I_R} \big/ \left(I_S + I_R\right)$. The left half of the SLM displayed π/4, while the right half displayed −π/4. To remove the background in the measured phase map caused by the SLM's curvature and the wavefront mismatch between the reference and the sample beams, the phase map measured when the SLM displayed all zeros was subtracted from the measured phase map. The phase maps measured when the SBR ranged from 6×10^{-3} to 6×10^{-5} are shown in Fig. 3.11(b). When the SBR was between 1 and 2×10^{-2}, the measured phase maps resemble the phase map measured when the SBR = 6×10^{-3}, so they are not shown. The phase sensitivity (defined as the standard deviation of the left half of the measured phase map) and the difference of the mean phase between the left and right halves of the phase map are shown as a function of SBR in Fig. 3.11(c). With decreasing SBR, the phase sensitivity degrades due to the decreasing signal-to-noise ratio (SNR), and the mean phase difference deviates more from the expected value of π/2 for the same reason. The phase sensitivity has reached 0.51 rad even when the SBR is 6×10^{-4}. To obtain the data in Fig. 3.11(c), as the SBR decreased from 1 to 6×10^{-5}, the light power at the image sensor was set to 1 mW, 1 mW, 4 mW, 8 mW, 17 mW, 44 mW, 120 mW, 120 mW, 120 mW and 120 mW. Higher power was used to increase the SNR when the SBR was low, but the power did not exceed 120 mW, to avoid camera saturation.

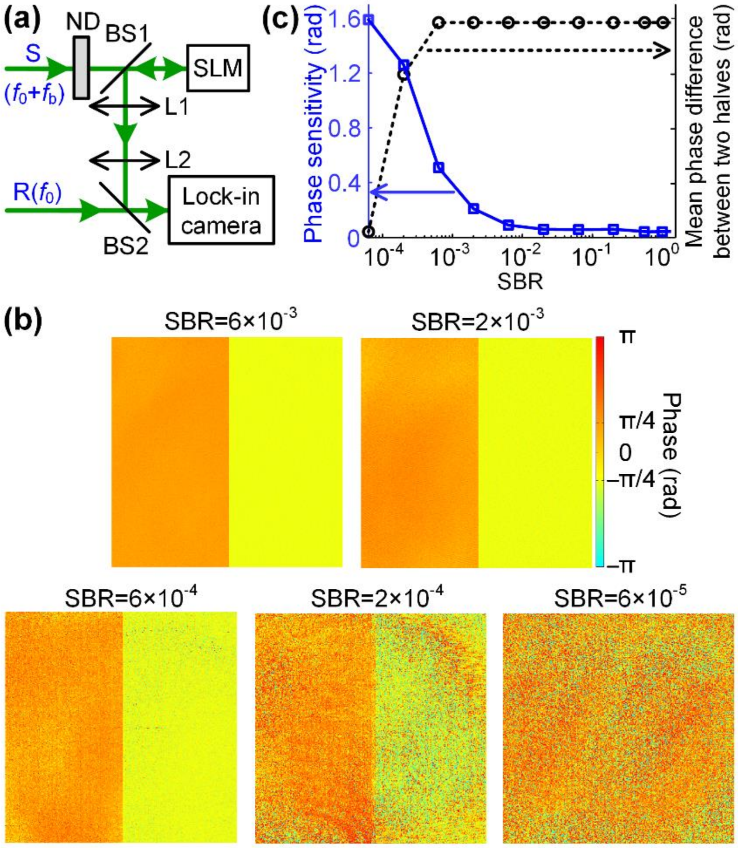

Figure 3.11 Characterizing the phase sensitivity of the lock-in camera. (a) Schematic of the set-up. The lock-in camera was used to measure the SLM-encoded wavefront of sample beam S at different signal-to-background ratios (SBRs) controlled by different neutral density (ND) filters. BS, beamsplitter; f_0, laser frequency; L, lens; R, reference beam; SLM, spatial light modulator. (b) The phase maps measured at different SBRs. (c) The phase sensitivity and the difference of the mean phase between the left and right halves of the phase map as a function of SBR.

Based on the lock-in camera, we developed a TRUE focusing system [Fig. 3.12(a)] to focus light inside a scattering medium composed of two ground glass diffusers. Our focusing procedure included two steps. In the first step, the wavefront of ultrasonically tagged light $\varphi_{\mathrm{T}}(\vec{r})$ was measured using the lock-in camera with a Mach–Zehnder interferometer. After passing through an acousto-optic modulator (AOM, AOM-505AF1, IntraAction), the frequency of the planar reference beam (R) became f_0+f_a, where f_a = 50 MHz, and f_0 was the laser frequency. In the sample arm (S), after passing through a ground glass diffuser (D1, DG10-1500, Thorlabs), the frequency of a portion of the diffuse light traversing the ultrasonic focus was shifted to $f_0 + (f_a + f_b)$, due to the acousto-optic effect, where $f_a + f_b = 50$ MHz + 70 kHz was the frequency of the ultrasound generated from an ultrasonic transducer (UST, V358-SU, Olympus; a customized lens with a 7.9 mm focal length and a 0.40 numerical aperture was attached to the surface of the transducer). The driving voltage to the transducer was 20 V, and the ultrasound was present only during the exposure time (0.286 ms) of the lock-in camera. The sample beam then passed through a second diffuser (D2, DG20-600, Thorlabs), collected by lens L5, and combined with R by 50/50 beamsplitter BS2. Then, the combined beams were reflected from an SLM (Pluto NIR-II, Holoeye; pixel size 8 μm) and were further directed to the lock-in camera by 50/50 beamsplitter BS3. The lock-in camera imaged the surface of the SLM by a 4*f* system (comprising lenses L6 and L7) with a magnification of 5/3, and each camera pixel imaged a super-pixel (3 × 3 pixels) on the SLM. The lock-in camera locked in the beat frequency $f_b = 70$ kHz and thus measured the phase map of the ultrasonically tagged light. In the second step, we achieved digital TRUE focusing by phase conjugating ultrasonically tagged light. In this step, the sample beam was blocked by a mechanical shutter, and we displayed the conjugate phase map $-\varphi_T(\vec{r})$ on the SLM [Fig. 3.12(b)]. Upon reflection from the SLM, the reference beam R acquired a wavefront $-\varphi_T(\vec{r})$, thus becoming phase conjugated to the ultrasonically tagged light. After passing through diffuser D2, the phase-conjugated light converged to the original ultrasonic focal position (No ultrasound was applied in this step). To visualize the TRUE focus, we placed 10/90 beamsplitter BS1 in between D2 and the ultrasonic focal position to produce a copy of the optical focus that was measured by a CCD camera outside the water tank WT.

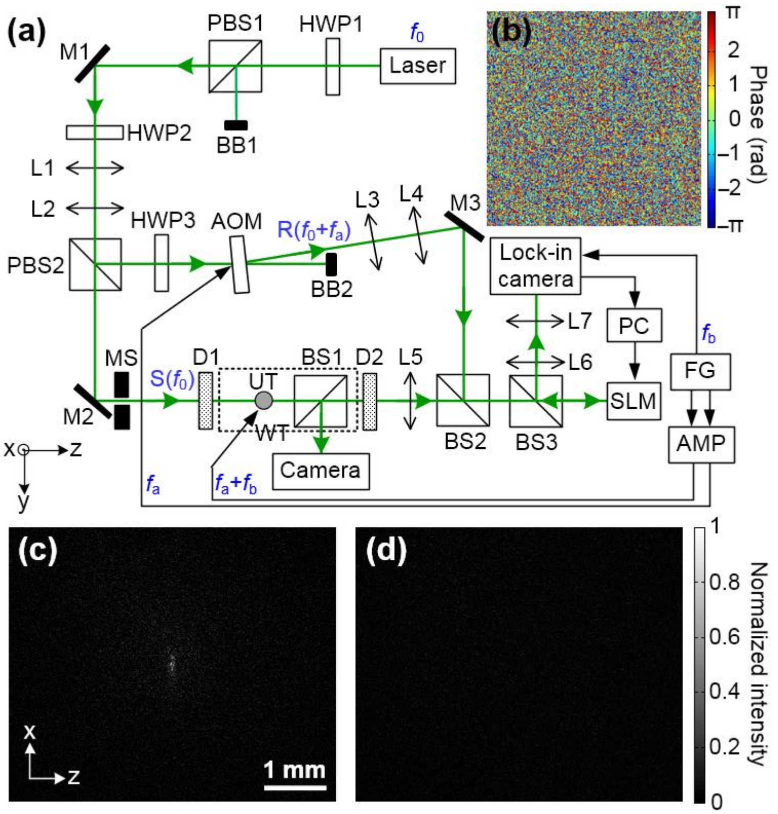

Figure 3.12 Lock-in camera based TRUE optical focusing inside a scattering medium composed of two diffusers. (a) Schematic of the set-up. AMP, power amplifier; AOM, acousto-optic modulator; BB, beam block; BS, beamsplitter; D, diffuser; FG, function generator; HWP, half-wave plate; L, lens; M, mirror; PC, personal computer; SLM, spatial light modulator; PBS, polarizing beamsplitter; UST, ultrasonic transducer; WT, water tank, denoted by the dashed rectangle. (b) The conjugate wavefront of the ultrasonically tagged light, which was displayed on the SLM. (c) The observed TRUE focus when the SLM displayed the phase map in (b). (d) When the correct phase map was shifted leftward by 1 super pixel (3 SLM pixels), the TRUE focus disappeared.

The observed TRUE focus is shown in Fig. 3.12(c), and it disappeared when the correct phase map on the SLM was shifted leftward by 1 super pixel (= 3 pixels) [Fig. 3.12(d)], as expected. In Fig. 3.12(c), the full width at half maximum (FWHM) focal spot size along the *y* direction was 58 µm, which is close to its theoretical value of 47 µm, as determined by the measured acoustic focal spot size along the transverse direction. The FWHM focal spot size along the *x* direction (the acoustic axis direction) was 262 µm, which is smaller than the measured depth of focus of the acoustic focal zone (= 336 µm). The peak-to-background ratio (PBR), defined as the ratio between the average intensities within and outside the TRUE focus, was 12, which is about 30 times lower than its theoretical value [~ 3.6×10^2, as calculated by $\pi N/(4M)$, where N (= 1.4×10^4) is the number of speckles recorded on the lock-in camera during wavefront measurement, and M (= 38) is the number of speckles in the measured TRUE focus [80]]. The discrepancy between the measured and the theoretical PBR is probably due to imperfect alignment, and the exact reason is under investigation. In our experiment, the distance between diffuser D1 and the ultrasonic focus was 13 mm, and the distance between diffusers D1 and D2 was 60 mm.

3.2.4 Discussion and Conclusion

For thick biological tissue, the number of speckles in the TRUE focus (M) can be as big as 10^5, which is significantly larger than that in our experiment. To maintain a sufficient PBR in this case, we may reduce M by iterative TRUE focusing [76, 81, 82] or time reversal of variance-encoded light (TROVE) [25], or increase N by increasing the pixel count of the camera.

In our TRUE focusing experiment, the SBR was measured to be 6×10^{-3}, which was comparable with the SBR achieved in previous TRUE focusing experiment using a sCMOS camera [76]. Currently, the sample arm was very lossy (only ~1/1000 of the light power incident on the sample arrived at the camera), which limited the available light power on the lock-in camera. To accommodate even lower SBRs for deeper penetration or more scattering samples by increasing the SNR, a stronger laser and a higher collection efficiency for the diffuse light are needed.

Currently, even though the wavefront is measured within 0.3 ms, it takes ~12 ms to transfer the data from the lock-in camera to a computer, limited by the speed of the USB 2.0 interface (~250 Mb/s). If a camera link interface is used (data transfer rate ~7024 Mb/s), which is commonly used with an sCMOS camera, the data transfer time can be reduced to 0.4 ms. Moreover, rather than outputting S_I and S_Q, the camera can also directly output a 16-bit phase map calculated by the on-chip FPGA, which reduces the data to transfer by half and removes the need to calculate the phase map on a computer (currently, it takes 4.2 ms for data processing in Matlab). Since digital optical phase conjugation has a high tolerance for phase error [19], 8 bits rather than 16 bits are sufficient to represent a phase value, so we can further decrease the data transfer time by half to 0.1 ms by using an 8-bit ADC. Currently, it takes ~30 ms to display a phase map on the SLM, which is the bottleneck of speed in our whole TRUE focusing procedure. Because SLMs with binary modulation, such as digital micromirror devices (DMDs) [21, 68, 80, 83, 84], are much faster than our gray-scale SLM, we plan to modify the FPGA program on the camera to output a binary phase map (1 bit per pixel) directly to a binary modulation SLM [Fig. 3.9(d)]. In this way, we can further decrease the data transfer load by 8 times.

In conclusion, based on a lock-in camera, we developed a method to quickly measure the wavefront of light in a low SBR condition, and applied it to TRUE optical focusing inside scattering media. Since the lock-in camera digitizes only the signal after rejecting the background, our method is highly efficient in the use of bits, and has the potential to achieve a very large data reduction at an early stage to minimize the amount of data to transfer. Combined with a binary modulation SLM, our approach can potentially complete the whole TRUE focusing procedure within 1 ms, which will open the door to many *in vivo* applications that require light focusing deep inside tissue. Compared with other wavefront sensors, such as Shack-Hartmann sensor, our sensor has much greater resolution (300 × 300 pixels versus 11 × 11 pixels [85]). Moreover, our high-speed wavefront measurement method is readily applicable to other time-reversal/optical-phase-conjugation-based techniques, such as time-reversed adapted perturbation focusing (TRAP [21, 26, 27]). Since the lock-in camera can also measure the amplitude of an AC signal ($=\sqrt{S_{\mathrm{I}}^2(\vec{r})+S_{\mathrm{Q}}^2(\vec{r})}$) for each pixel in parallel in a low SBR condition, it is an excellent choice for ultrasound-modulated optical tomography (also known as acousto-optic imaging) [33].

3.3 High-speed digital TRUE focusing based on a ferroelectric spatial light modulator and binary wavefront measurement

3.3.1 Introduction

Digital OPC (DOPC) and digital TRUE focusing has been limited by the low speeds of cameras, data transfer, data processing, and spatial light modulator. The low speeds prevent DOPC from being applied to thick living biological tissue, because the motion of the scatterers inside tissue causes the speckles on the phase conjugate mirror to decorrelate (on a time scale of 0.1 – 10 ms [24, 50, 80, 86], and breaks the time-reversal symmetry. Although a bit-efficient, sub-millisecond wavefront measurement method was developed based on a lock-in camera [32], the net speed of the system was limited by the low speed of data transfer and wavefront modulation. Recently, a fast DOPC system controlling 1.3×10^5 optical degrees of freedom was developed, and it focused light through scattering media with an effective latency of 5.3 ms and a total system runtime of 7.1 ms [80]. The system employed a single-shot wavefront measurement method, a field programmable gate array (FPGA) for data processing, and a digital micromirror device (DMD) for fast modulation. However, the reported single-shot wavefront measurement method does not work when the goal is to focus light inside, instead of through, highly scattering media. For biomedical and many other applications, focusing light inside scattering media is much more useful and difficult than focusing light through scattering media. The use of a DMD also imposes several limitations, which will be explained in the next section.

Here, we develop a simpler but faster DOPC system that focuses light not only through, but also inside, scattering media. For the first time in the wavefront shaping field, we employ a ferroelectric liquid crystal based SLM to achieve binary-phase modulation for high speed and high focusing quality. To take full advantage of the SLM and further improve the speed of ultrasound-guided DOPC, we develop a double-exposure binary wavefront measurement method. The speed of our system is one to two orders of magnitude higher than that of previous ultrasound-guided DOPC systems [25, 30-32, 76, 77, 81, 82, 87], and our method achieves the fastest light focusing inside a scattering medium among all the digital wavefront shaping methods developed to date [12-14].

3.3.2 Methods

Binary-phase modulation based high-speed wavefront shaping enabled by a ferroelectric liquid crystal based SLM

DOPC focuses light through or inside scattering media by phase conjugating the scattered light emitted from a guide star. Specifically, a digital camera is used to measure the wavefront of the scattered light with digital holography. Then, an SLM, whose pixels are one-to-one matched with the pixels of the camera by a camera lens, is used to reconstruct the conjugate wavefront of the scattered light to achieve optical phase conjugation/time reversal. In most wavefront shaping experiments, nematic liquid crystal based SLMs (NLC-SLMs) are used for phase modulation [15, 17, 19, 20]. However, the latency of NLC-SLMs (typically tens of milliseconds [21, 86], including the response time of the molecules and the data transfer time) is much longer than the speckle correlation time associated with living biological tissue. To increase the speed, digital micromirror devices (DMDs) have been employed to achieve high-speed wavefront shaping [68, 80, 84, 88-91]. However, DMDs have several limitations for this application: a) They typically achieve binary-amplitude modulation, which results in a lower focusing contrast compared with that of phase modulations. b) The optical fluence threshold causing DMDs to malfunction under pulsed laser illumination is usually lower than that of liquid crystal based SLMs [92]. c) The alignment of a DMD based DOPC system is significantly complicated by the oblique reflection angle of the DMD [80]. d) Although a loaded pattern can be displayed at ~23 kHz on a DMD, transferring a pattern from a PC or an FPGA board to the DMD can take 1.6 – 4.5 ms [80, 89, 91], limiting the speed of a DOPC system.

To overcome the above drawbacks of DMDs and NLC-SLMs, we developed a high-speed DOPC system using a ferroelectric liquid crystal based SLM (FLC-SLM, A512-P8, Meadowlark Optics, 512 × 512 pixels, 15 µm pixel size), which has a net latency of ~1 ms including the data transfer time. Specifically, it takes ~0.6 ms to transfer a pattern from a PC to the SLM using a PCI Express ×4 interface, and the response time of the FLC molecules is ~0.45 ms. Unlike NLC-SLMs that modulate the phase of the light field on each SLM pixel by a value between 0 and 2π, FLC-SLMs modulate the phase of the light field by only 0 or π (binary-phase modulation). Since in principle only one bit per pixel needs to be transferred to an FLC-SLM from a PC, while eight bits per pixel needs to be transferred to an NLC-SLM, the use of FLC-SLMs can reduce the data transfer load by eight times and thus increase the data transfer speed.

Figure 3.13 shows a comparison of different wavefront modulation schemes. Without shaping the wavefront of the input light, the light field at a targeted location inside a scattering medium is a random phasor sum. In conventional wavefront shaping, an NLC-SLM rotates each phasor to align them, so that they constructively interfere and form a focus. A DMD, on the other hand, achieves wavefront shaping by binary-amplitude modulation – it turns off those “bad” phasors that destructively interfere with the net phasor formed by the rest of the phasors. In contrast, instead of turning off the "bad" phasors, an FLC-SLM rotates the "bad" phasors by 180°, making them constructively interfere with the net phasor formed by the rest. In this way, FLC-SLMs double the focal peak-to-background ratio (PBR, which quantifies the focusing contrast), compared with DMDs [21, 93, 94] (see Supplementary notes for a derivation of the theoretical PBR for binary-phase modulation based wavefront shaping). Although the PBR achieved by FLC-SLMs is 40% of that achieved by NLC-SLMs that achieve full-phase modulation, the response time of FLC molecules (0.04 – 0.45 ms) is much shorter than that of NLC molecules, because FLC molecules have a spontaneous electric polarization, which enables them to respond quickly to an external electric field [95].

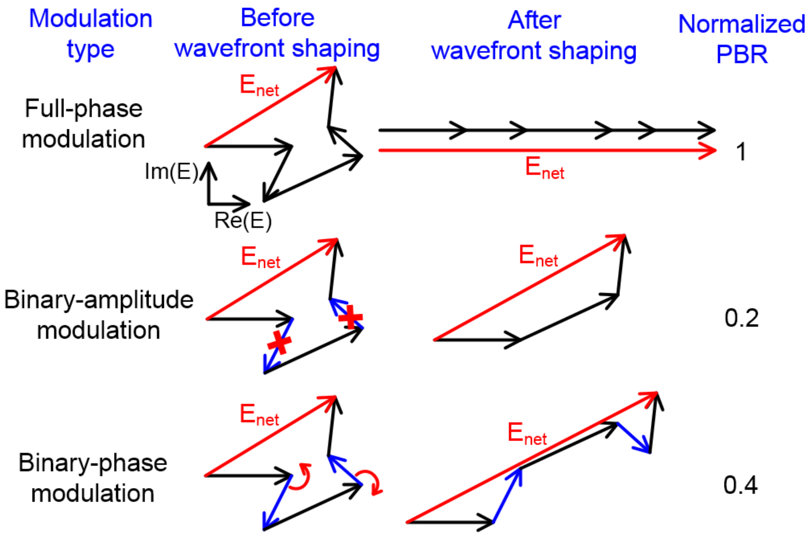

Figure 3.13 A comparison of different wavefront modulation schemes in wavefront shaping. PBR, peak-to-background ratio.

Figures 3.14(a) – (b) show how an FLC-SLM achieves binary-phase modulation. The SLM works in reflection mode. While the FLC layers act as a quarter-wave plate, the net result for round-trip light propagation is that each SLM pixel acts as a half-wave plate, whose optic axis orientation is electrically controllable between two states that are 2θ apart (θ = 22.5°, see e_1 and

e_2 in Fig. 3.14(b)). To achieve binary-phase modulation, the polarization direction of the incident light field bisects the two states of the optic axis, i.e., along the vertical direction. By reflection off an SLM pixel, the polarization of the light field is rotated to along either −45° or +45°, depending on the orientation of the optical axis. After passing through a linear polarizer whose axis is along the horizontal direction, the output electric field is either along −90° or +90° for the two optical axis states, with the same amplitude [Fig. 3.14(b)]. In this way, an FLC-SLM achieves binary-phase modulation. For reflection-mode FLC-SLMs, the linear polarizer is usually replaced by a polarizing beamsplitter [Fig. 3.14(a)]. It should be noted that the FLC-SLM requires vertically polarized incident light, while the output binary wavefront corresponds to horizontally polarized light.

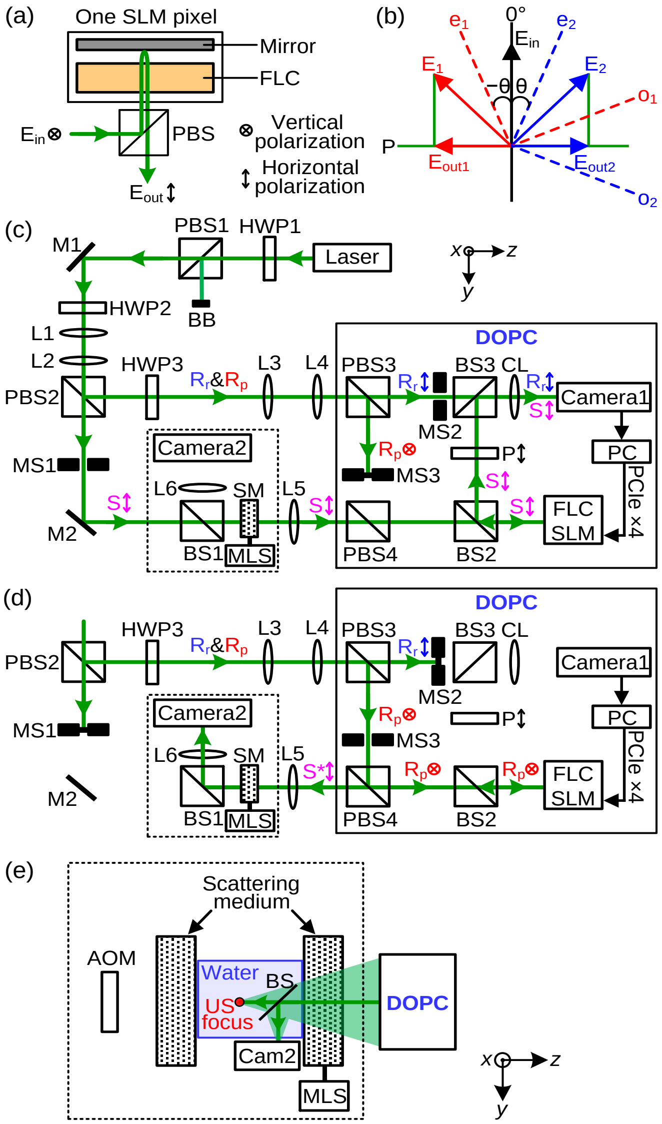

Figure 3.14 Digital optical phase conjugation using a ferroelectric liquid crystal based spatial light modulator (FLC-SLM). (a) Each FLC-SLM pixel acts as a half-wave plate. PBS, polarizing beamsplitter. (b) The optical axis orientation can be switched between two states (e_1 and e_2), to achieve binary-phase modulation of the incident light E_{in}. $\theta = 22.5°$. (c) Schematic of the set-up during wavefront recording for DOPC based light focusing through scattering media. BB, beam block; BS, beamsplitter; CL, camera lens; DOPC, digital optical phase conjugation; HWP, half-wave plate; M, mirror; MLS, motorized linear stage; MS, mechanical shutter; PC, personal computer; PCIe ×4, peripheral component interconnect express interface with 4 lanes; SM, scattering medium; S, sample beam; R_r and R_p, reference beams for wavefront recording and playback. (d) Schematic of the set-up during wavefront playback for DOPC based light focusing through scattering media. (e) Schematic of the set-up for focusing light inside a scattering medium comprising two pieces with ultrasound-guided DOPC. A complete schematic can be obtained by replacing the components enclosed in the dashed box in Figs. 3.14(c) and (d) with the components enclosed in the dashed box in Fig. 3.14(e). The acousto-optic modulator (AOM) is used only during wavefront recording. During wavefront playback, to verify that light is focused to the ultrasonic (US) focus, a beamsplitter (BS) reflects the focal pattern onto Camera2 (Cam2). This configuration allows us to study the effect of medium decorrelation on the quality of the phase-conjugated focus. To control the speckle correlation time on the SLM plane, a motorized linear stage (MLS) moves the second piece of the scattering medium at different speeds during the entire DOPC process (including both wavefront measurement and playback).

B. Experimental set-up and methods for fast binary wavefront measurement

Using an FLC-SLM, we developed a DOPC system to focus light through [Figs. 3.14(c) and (d)] or inside [Fig. 3.14(e)] scattering media. In Fig. 3.14(c), the output of a continuous-wave laser (1 W, 532 nm, Verdi V10, Coherent) was split into a sample beam (S) and two planar reference beams (R_r and R_p, for wavefront recording and playback, respectively). S was first scattered by a scattering medium. Then, to measure the wavefront of the scattered light field along the horizontal polarization direction, we let the scattered light interfere with horizontally polarized R_r on Camera1 (pco-edge 5.5, PCO Tech, 500 μs exposure time). To obtain the binary phase map for focusing light through scattering media, we used the single-shot binary phase retrieval method [80]. Specifically, the interference pattern between S and R_r is written as $I(\vec{r}) = I_S(\vec{r}) + I_R(\vec{r}) + 2\sqrt{I_R(\vec{r})I_S(\vec{r})}\cos[\varphi_S(\vec{r}) - \varphi_R(\vec{r})] \approx I_R(\vec{r}) + 2\sqrt{I_R(\vec{r})I_S(\vec{r})}\cos[\varphi_S(\vec{r}) - \varphi_R(\vec{r})]$, where I_S and I_R are the intensities of S and R_r impinging on each camera pixel at position $\vec{r}$, and $I_R >> I_S$ in this experiment; φ_S and φ_R are the phases of S and R_r, and φ_R is assumed to be a constant. $I_R(\vec{r})$ is not dependent on the dynamics of the sample and can be measured separately by blocking the sample beam before starting DOPC experiments. Then, the binary phase map of S is obtained by

$$\varphi_S(\vec{r}) = \begin{cases} 0, \text{ if } I(\vec{r}) \geq I_R(\vec{r}) \\ \pi, \text{ if } I(\vec{r}) < I_R(\vec{r}) \end{cases},$$

where a constant phase offset φ_R is ignored. To achieve phase conjugation, a pre-calibrated binary phase map to compensate for the curvatures of R_r, R_p, and the SLM was added to the phase map $\varphi_S(\vec{r})$ [96], and the resulting binary phase map was displayed on the FLC-SLM to modulate the wavefront of $\mathrm{R_p}$ [Fig. 3.14(d)]. After reflecting off the FLC-SLM and passing through polarizing beamsplitter PBS4, $\mathrm{R_p}$ became phase conjugate to the horizontal component of the scattered light field S exiting the scattering medium. After propagating through the scattering medium, $\mathrm{R_p}$ became a collimated beam and was focused by lens L6 onto Camera2 (GS3-U3-23S6M, Point Grey, exposure time = 1 ms).

To focus light inside, rather than through, scattering media, focused ultrasound was used as a guide star for DOPC, and this ultrasound-guided OPC is known as time-reversed ultrasonically encoded (TRUE) optical focusing. Fig. 3.14(e) is a schematic of the set-up for focusing light inside a scattering medium comprising two pieces. A complete schematic can be obtained by replacing the components enclosed in the dashed box in Figs. 3.14(c) and (d) with the components enclosed in the dashed box in Fig. 3.14(e). During wavefront recording, the sample beam S was first frequency up-shifted by 50 MHz by an acousto-optic modulator (AOM-505AF1, IntraAction) before it illuminated the scattering sample. After being scattered by the first piece of the scattering medium, a portion of the light passing through the ultrasonic focus was frequency down-shifted by 50 MHz because of the acousto-optic effect (the frequency of the ultrasound was 50 MHz), and further scattered by the second piece of the scattering medium [Fig. 3.14(e)]. These ultrasonically tagged photons formed a stable hologram on Camera1 when interfering with the reference beam $\mathrm{R_r}$. The intensity recorded by Camera1 can be written as $I(\vec{r}) = I_{\mathrm{R}}(\vec{r}) + I_{\mathrm{T}}(\vec{r}) + I_{\mathrm{U}}(\vec{r}) + 2\sqrt{I_{\mathrm{R}}(\vec{r}) I_{\mathrm{T}}(\vec{r})}\cos\left[\varphi_{\mathrm{T}}(\vec{r}) - \varphi_{\mathrm{R}}(\vec{r})\right]$, where I_{T} and I_{U} are the intensities of the ultrasonically tagged light and untagged light ($I_{\mathrm{U}} >> I_{\mathrm{T}}$ for highly scattering media), and φ_{T} is the phase of the ultrasonically tagged light we want to measure. To use the single-shot wavefront measurement method [80] to obtain φ_{T}, $\sqrt{I_{\mathrm{R}}(\vec{r}) I_{\mathrm{T}}(\vec{r})} >> I_{\mathrm{U}}(\vec{r})$ needs to be satisfied. However, this condition is generally not satisfied for highly scattering media without using an excessively high I_{R}, which would dramatically reduce the signal-to-background ratio and the signal-to-noise ratio [31, 32, 82]. Thus, the single-shot wavefront measurement method cannot be used here. To measure the phase map at maximum speed by minimizing the number of holograms recorded, we developed a double-exposure binary wavefront measurement method, which also works perfectly with FLC-SLMs that perform binary-phase modulation. Specifically, we record two frames when focused ultrasound was applied. However, in the second frame, the initial phase of the ultrasound was shifted by π. Mathematically, the intensities on each pixel of Camera1 recorded in the two frames can be written as $I_1(\vec{r}) = I_{\mathrm{R}}(\vec{r}) + I_{\mathrm{T}}(\vec{r}) + I_{\mathrm{U}}(\vec{r}) + 2\sqrt{I_{\mathrm{R}}(\vec{r}) I_{\mathrm{T}}(\vec{r})}\cos\left[\varphi_{\mathrm{T}}(\vec{r}) - \varphi_{\mathrm{R}}(\vec{r})\right]$ and $I_2(\vec{r}) = I_{\mathrm{R}}(\vec{r}) + I_{\mathrm{T}}(\vec{r}) + I_{\mathrm{U}}(\vec{r}) + 2\sqrt{I_{\mathrm{R}}(\vec{r}) I_{\mathrm{T}}(\vec{r})}\cos\left[\varphi_{\mathrm{T}}(\vec{r}) + \pi - \varphi_{\mathrm{R}}(\vec{r})\right]$. Then, the binary phase map of the ultrasonically tagged light can be obtained by

$$\varphi_{\mathrm{T}}(\vec{r}) = \begin{cases} 0, \text{ if } I_1(\vec{r}) \geq I_2(\vec{r}) \\ \pi, \text{ if } I_1(\vec{r}) < I_2(\vec{r}) \end{cases},$$

where a constant phase offset φ_{R} is ignored. To generate two bursts of ultrasound that have a π shift in the initial phase, we used an RF switch (ZASWA-2-50DR+, Mini-Circuits) to sequentially enable the outputs of the two channels of a function generator. Each channel generated a 2.9 ms long burst of sinusoidal waves with an amplitude of 80 mVpp, and the initial phases of the bursts generated by the two channels differed by π (see Fig. 3). By using this approach, we avoided an unwanted amplitude change when using an RF phase shifter. The output of the RF switch was amplified by a power amplifier (25A250A, Amplifier Research) with a gain of 54 dB, to drive an ultrasonic transducer (V358-SU, Olympus, with a lab-made lens having a numerical aperture of 0.4). During wavefront playback, to verify that light was focused to the ultrasonic focus by phase conjugation, a beamsplitter was used to reflect the focal pattern onto Camera2 [Fig. 3.14(e)]. This configuration allowed us to study the effect of medium decorrelation on the quality of the phase-conjugated focus, because we could move the scattering medium at different speeds during the entire DOPC process while monitoring the corresponding focusing quality. In our experiments, a program written in C/C++ calculated the phase map, and controlled the cameras, the FLC-SLM and a multifunction data acquisition card (PCIe 6363, National Instruments) for trigger generation.

Total system runtime and effective system latency

The total system runtime, defined as the time from when Camera1 starts recording to playback of the wavefront, is 4.7 ms for focusing light through scattering media with the single-shot binary phase retrieval method. The total system runtime is 7.7 ms for focusing light inside scattering media with the double-exposure binary phase retrieval method (see the workflow in Fig. 3.15). However, the effective system latency is shorter than the total system runtime [80], since a rolling shutter was used in Camera1 to achieve a higher frame rate during wavefront recording. With the rolling shutter, the top and the bottom halves of the image sensor expose and read out simultaneously in a row by row manner from the edge to the center of the sensor, and neighboring rows are exposed successively with a 9.17 μs delay in their start times. Since the central 520 rows on the sensor of Camera1 were used in our experiments, the effective system latencies, calculated from the average exposure start time to the playback of the wavefront, are 3.5 ms and 6.5 ms for focusing light through and inside scattering media, respectively. The actual system latencies, defined as the time constants in the exponential relationship between the measured PBR and the speckle correlation time [80], were obtained by the experiments described in the next section, and were 3.0 ms and 6.0 ms for focusing light through and inside scattering media, respectively. It should be noted that by under-sampling speckle grains on Camera1 and the SLM [35], the number of optical degrees of freedom controlled by our system was 2.6×10^5, limited by the SLM pixel count (512 × 512 pixels). Our number of optical degrees of freedom is two to three orders of magnitude more than that in feedback-based wavefront shaping [15] and conventional adaptive optics experiments [97].

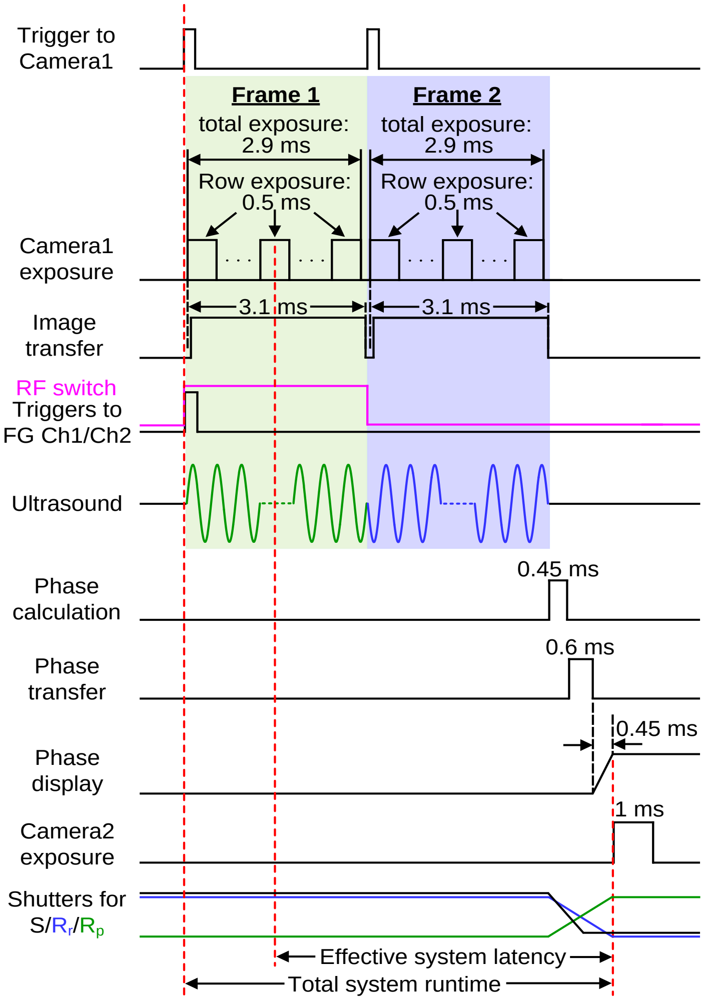

Figure 3.15 Workflow of TRUE optical focusing inside scattering media. A rolling shutter was used for Camera1, i.e. neighboring rows are exposed successively with a 9.17 µs delay in their start times. The shutter for S (LS6, Vincent Associates) has a full-aperture transfer time of 0.8 ms, while the shutters for R_r (VSR14, Vincent Associates) and R_p (VS14, Vincent Associates) have full-aperture transfer times of 1.5 ms, because of their larger aperture sizes (14 mm). FG, function generator; Ch, channel; RF, radio-frequency.

3.3.3 Results

DOPC system quantification

Similar to what was done in Ref. [80], we quantified the OPC efficiency of our system by calculating the ratio between the experimental and the theoretical PBR of the focus achieved by focusing light through an opal diffuser with a 4π scattering angle (10DIFF-VIS, Newport). PBR was calculated by the ratio between the average intensity of the pixels in the focus whose intensities are above half the maximum intensity and the ensemble average of the mean intensity of the speckles when a random wavefront was applied. Fig. 3.16(a) shows the focus our DOPC system achieved when focusing light through the opal diffuser, and Fig 3.16(b) shows the focal intensity distribution along the vertical direction. The experimental PBR is 5.1×10^3 and the background intensity is calculated over an area of 1.2×1.2 mm^2. The theoretical PBR is calculated by $N/(2\pi M)$, where N is the number of optical degrees of freedom, M is the number of speckle grains in the DOPC focus, and the factor of 2 is due to the fact that the opal diffuser nearly completely scrambles the polarization and our system phase conjugates only a single polarization of the sample light [34] (see Supplementary notes). The speckle size on the FLC-SLM was 7.6 µm, computed from the full width at half maximum (FWHM) of the autocovariance function of the speckle patterns measured by a camera with a pixel size of 3.45 µm. Since the camera lens for Camera1 had a magnification ratio of 0.43, the speckle size on Camera1 was 3.3 µm, which was smaller than the pixel size of Camera1 (6.5 µm). We intentionally had Camera1 under-sample the speckle grains to increase the number of optical degrees of freedom [35], so $N = 512 \times 512$. To compute M, we measured the area of the achieved focus on Camera2 (1.5×10^3 $\mu\mathrm{m}^2$) and the area of a speckle grain on Camera2 (8.1×10^2 $\mu\mathrm{m}^2$, computed from the speckle size). So, $M = 1.9$, and the theoretical PBR is $N/(2\pi M) = 2.2 \times 10^4$. Thus, the experimental PBR is 23% of the theoretical PBR, and the discrepancy is probably due to imperfect alignment and imperfect correction for the curvatures of the reference beams and the SLM.

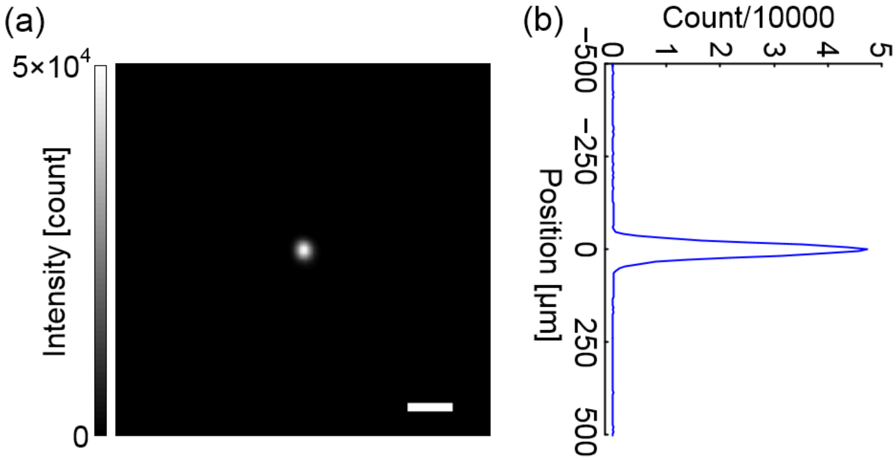

Figure 3.16 Focusing light through an opal diffuser. (a) Image of the DOPC focus after light passed through an opal diffuser with a 4π scattering angle. The peak-to-background ratio is 5.1×10^3. Scale bar, 100 μm. (b) Focal intensity distribution along the vertical direction.

Focusing light through moving scattering tissue

To measure the actual system latency, we used our DOPC system to focus light through a dynamic scattering medium with controllable speckle correlation times, achieved using a moving sample strategy [24, 68, 69, 80, 89]. The scattering sample was a 3 mm thick slice of fresh chicken breast tissue (scattering coefficient μ_s = 30 mm^{-1}, scattering anisotropy g = 0.965 [80]), sandwiched between two microscope slides. To ensure the tissue was 3 mm thick, three 1 mm thick microscope slides were used as spacers between the two microscope slides. To minimize the change of tissue’s optical property, the sample chamber was sealed by aluminum foil tape to mitigate tissue dehydration, and all experiments were completed within 8 hours after the sample was prepared. To control the speckle correlation time on the SLM plane by controlling the tissue movement speed, the sample was mounted on a linear stage with a motorized actuator (LTA-HS, Newport). To ensure the stage reached and maintained the preset speed, we started the wavefront measurement 10 seconds after the stage began to accelerate, and let the stage continue running for 10 seconds after the wavefront playback had finished (to avoid deceleration of the stage during measurement).

To measure the speckle correlation time at a given tissue movement speed, we used a camera with a pixel size of 3.45 μm to record movies of speckle patterns (along the horizontal polarization direction, by adding a polarizer) on the SLM plane, as the tissue was moved. We could not use Camera1 for this task since the speckle grains were under-sampled on Camera1. Then, we calculated the correlation coefficients between the first and each of the ensuing frames of the recorded speckle patterns. By fitting the correlation coefficient R_{I} versus time, using [24, 58] $R_{\mathrm{I}}(t) = \exp(-2t^2/\tau_{\mathrm{c}}{}^2)$, we obtained the speckle correlation time τ_{c}, defined as the time during which the correlation coefficient decreases to $1/e^2$ (=13.5%) at a given tissue movement speed. As an example, Fig. 3.17(a) shows the correlation coefficient as a function of time when the tissue was moved at 0.01 mm/s, from which τ_{c} = 131 ms was determined. The relationship between the measured speckle correlation time τ_{c} and the preset tissue movement speed v is shown in Fig. 3.17(b). By fitting the experimental data with a theoretical model [24] $\tau_{\mathrm{c}} = d_{\mathrm{b}}/v$, we obtained τ_{c} = 1.3/v [ms] (the unit of v is mm/s), where d_{b} = 1.3 μm is the expected speckle size back-projected from the SLM plane to the sample plane through collection lens L5. Based on this equation, we were able to control the speckle correlation time by controlling the tissue movement speed.

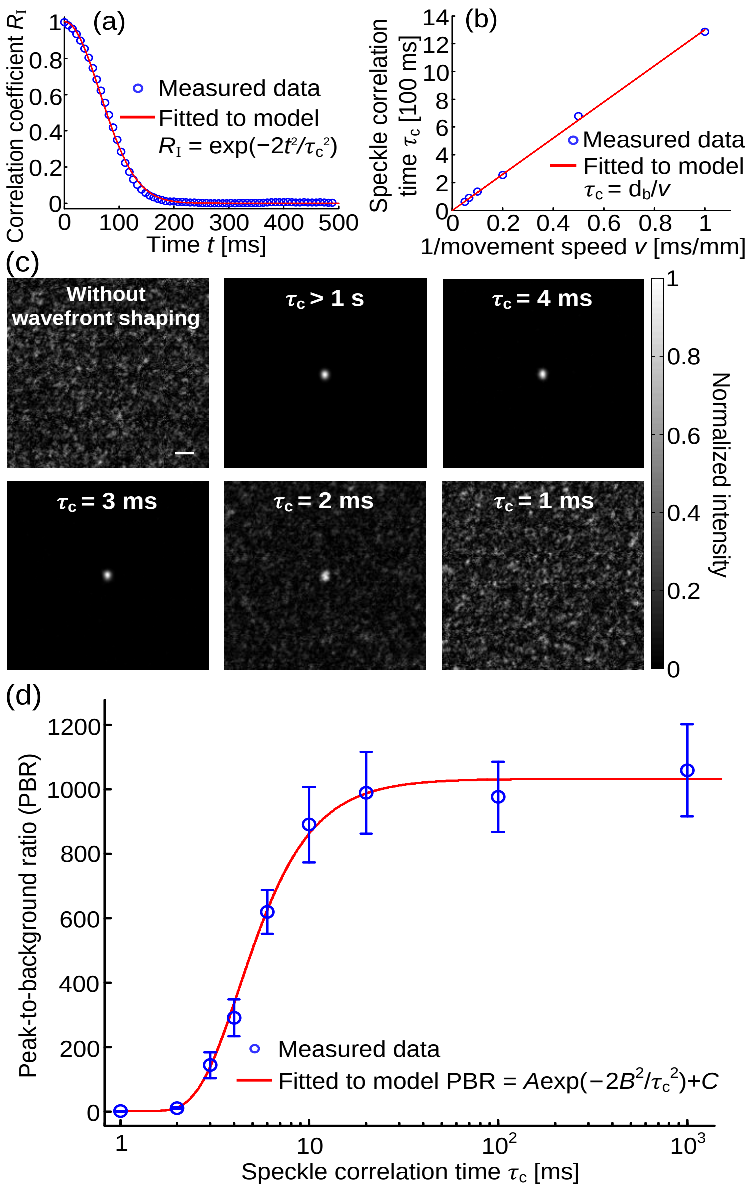

Figure 3.17 Focusing light through moving scattering tissue. (a) The correlation coefficient between the speckle patterns as a function of time, when a 3 mm thick slice of chicken tissue was moved at 0.01 mm/s. Speckle correlation time $\tau_c = 1.3 \times 10^2$ ms was determined for this speed. (b) The relationship between the speckle correlation time and the tissue movement speed. Errors bars are not plotted due to their indiscernible lengths in the figure. (c) Images of the DOPC foci after light passed through the tissue, when the tissue was moved at different speeds. Scale bar, 100 μm. (d) The peak-to-background ratio as a function of the speckle correlation time. The error bar shows the standard deviation of three measurements.

Figure 3.17(c) shows images of the DOPC foci observed on Camera2 after light passed through the moving tissue, when the corresponding speckle correlation time was varied from 1 ms to greater than 1 s (corresponding to zero movement speed). A high-contrast focus was achieved when the speckle correlation time τ_c was no shorter than 2 ms. The PBRs for τ_c > 1 s, = 4 ms, = 3 ms, and = 2 ms are 1076, 271, 166, and 12, respectively. As a control, when a random phase map was displayed on the SLM, no focus was observed. When τ_c = 1 ms, we could not observe a focus since the DOPC system was not fast enough. Because the PBR is proportional to the speckle correlation coefficient R_I (see Supplementary notes for a proof, also see [86]), the experimental PBR as a function of the speckle correlation time τ_c, shown in Fig. 3.17(d), can be fitted by a theoretical model PBR = $A\exp(-2B^2/\tau_c^2)+C$ (see Supplementary notes). From the fitting, we obtain the time constant B = 3.0 ms, which is the actual system latency [80]. When τ_c = B, the PBR reduces to ~1/e^2 of the PBR achieved when the sample is static.

Focusing light inside moving scattering tissue

To quantify the actual system latency for focusing light inside scattering media, we used our DOPC system to focus light inside a dynamic scattering medium comprising two pieces of chicken breast tissue, each 20 mm × 25 mm × 1 mm along the x, y and z directions (see Fig. 3.14(e) for the orientations of the axes). The second piece of tissue (the one in between the ultrasonic focus and the SLM) was moved at different speeds by a motorized stage to control the speckle correlation time on the SLM plane. Following the same procedure as described in the preceding section, we calibrated the relationship between the speckle correlation time and the tissue movement speed, and obtained τ_c = 1.5/v [ms] (the unit of v is mm/s). Fig. 3.18(a) shows Camera2 recorded images of the foci achieved by TRUE focusing at speckle correlation times ranging from 4 ms to longer than 1 s (corresponding to zero movement speed). The FWHM focal spot size along the y direction was 66 μm, which is close to the measured acoustic focal spot size along the transverse direction (47 μm). The FWHM focal spot size along the x direction (the acoustic axis direction) was 324 μm, which is close to the measured depth of focus of the acoustic focal zone (336 μm). The PBR of the focus decreases with decreasing speckle correlation time. As a control, when a random phase map was displayed on the SLM, no focus was observed. In Supplementary notes, we mathematically prove that for a speckle field such as the case in TRUE focusing, the PBR is still proportional to the speckle correlation coefficient R_{I}. Thus, the experimental PBR as a function of the speckle correlation time τ_{c}, shown in Fig. 3.18(b), can again be fitted by the theoretical model PBR = $A\exp(-2B^2/\tau_{\mathrm{c}}^2)+C$. From the fitting, we obtain the time constant B = 6.0 ms, which is the actual system latency for focusing light inside scattering media.

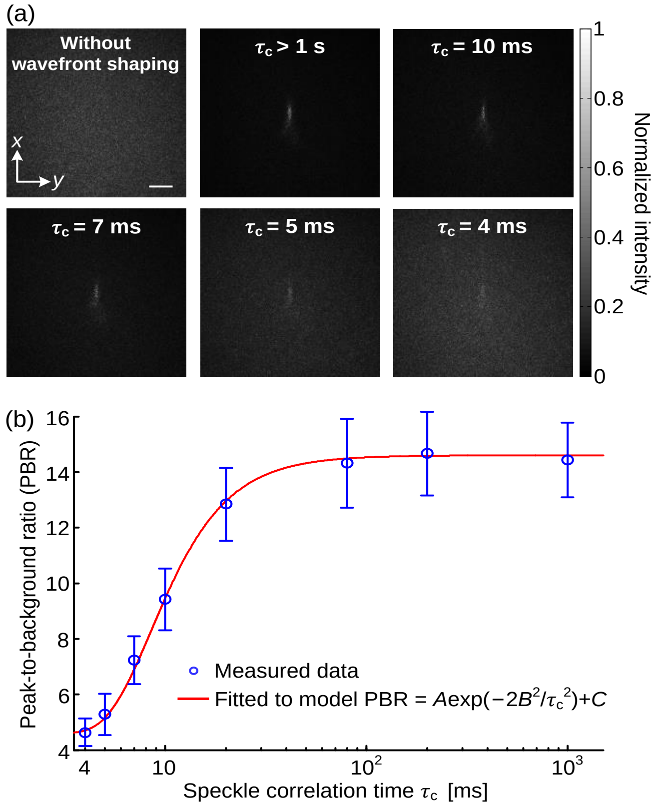

Figure 3.18 Focusing light inside a dynamic scattering medium comprising two pieces of chicken tissue. (a) Images of the foci achieved by TRUE focusing at different speckle correlation times (τ_{c}). Scale bar, 500 μm. (b) The peak-

to-background ratio as a function of the speckle correlation time. The error bar shows the standard deviation of three measurements.

3.3.4 Discussion and Conclusion

Currently, the speed bottleneck of our DOPC system is the low camera frame rate during wavefront measurement. Cameras with faster readout and data transfer will reduce the system runtime. Here, we used a camera exposure time of 0.5 ms, which is the minimum for this camera. By using a camera such as pco.edge 4.2, we can reduce the exposure time to 0.1 ms while roughly maintaining the frame rate. This change can reduce the system runtime by ~0.4 ms. For TRUE focusing, since the signal is often buried in a large background, it is ideal to use a lock-in camera to digitize only the signal after rejecting the background [32, 33, 98, 99]. We have used a commercial lock-in camera to measure the wavefront in TRUE focusing within 0.3 ms, but the data transfer of this camera takes longer than 10 ms, limited by the low data transfer speed of USB 2.0. To achieve better performance, the pixel count of the lock-in camera needs to be increased (currently there are 300 × 300 pixels), and the data transfer rate needs to be improved by using a faster interface.

Because of its spontaneous electric polarization, ferroelectric liquid crystals respond to an external electric field much faster than nematic liquid crystals. Although the FLC molecules in the SLM we use have a response time of ~0.45 ms, FLC molecules with a much shorter response time (e.g., 0.04 ms) are available in other commercial FLC-SLMs (e.g., from Forth Dimension Displays). However, since these SLMs are mainly developed for display applications that do not require a speed as high as DOPC does, the net speed (<= 240 Hz) is currently limited by the data transfer speed of the display interface and needs to be increased. Also, for these FLC-SLMs, the image transfer protocol that is designed for transferring 24-bit RGB images needs to be modified to enable high-speed transfer of a binary image.

To obtain the phase map in TRUE focusing, our double-exposure binary wavefront measurement method reduces the phase computation load dramatically compared with the traditional phase-shifting holography method [30, 31], since our approach needs only to compare two numbers to get the binary phase for each pixel, without the need to calculate the four-quadrant inverse tangent.

In conclusion, we developed a high-speed DOPC system using a ferroelectric liquid crystal based SLM that achieves binary-phase modulation. Compared with DMDs that perform binary amplitude modulation, FLC-SLMs double the PBR, have a higher malfunction threshold for pulsed lasers, and simplify the alignment of a DOPC system (because FLC-SLMs do not have oblique reflection angles as DMDs do). To take full advantage of the FLC-SLM and improve the speed of TRUE focusing, we developed a double-exposure binary wavefront measurement method. Our system focuses light through and inside scattering media, with system latencies of 3.0 ms and 6.0 ms, respectively. Since the demonstrated speed approaches tissue decorrelation rates, this work is an important step towards *in vivo* deep-tissue non-invasive optical imaging, manipulation, and therapy.

3.3.5 Supplementary notes

Peak-to-background ratio of binary-phase modulation based wavefront shaping

Here, we derive the theoretical peak-to-background ratio **(**PBR) of the focus when the playback wavefront is achieved by a ferroelectric liquid crystal based spatial light modulator (FLC-SLM) that performs binary-phase modulation. For a thick scattering medium, the incident light field $\mathbf{E}_{\mathbf{in}}$

and the scattered light field $\mathbf{E_S}$ are connected by a transmission matrix $\mathbf{T} = \left(a_{ij}\right)_{N\times S}$, whose element a_{ij} follows a circular Gaussian distribution. For an incident field $\mathbf{E_{in}} = (1\ 0\ \cdots\ 0)^T_{1\times S}$ that has only one nonzero element (one input mode [12]), the scattered light field is computed as $\mathbf{E_S} = \mathbf{T}\mathbf{E_{in}} = \left(a_{11}\ a_{21}\ \cdots\ a_{N1}\right)^T$, where the upper case T stands for matrix transposition. After the scattered light field is measured, the playback field under binary-phase modulation takes the following form: $\mathbf{E_P} = \mathrm{BP}(\mathbf{E_S^*}) = \left(\mathrm{BP}\left(a_{11}^*\right)\ \mathrm{BP}\left(a_{21}^*\right)\ \cdots\ \mathrm{BP}\left(a_{N1}^*\right)\right)^T$, where * denotes complex conjugation, and the binary-phase operator $\mathrm{BP}\left(z = x + iy\right)$ is defined as

$$\mathrm{BP}\left(z\right) = \begin{cases} \mathrm{e}^{i0} = 1, & \text{if } y \geq 0 \\ e^{i\pi} = -1, & \text{if } y < 0 \end{cases}. \tag{S3.1}$$

After passing through the scattering medium in the backward direction, the phase conjugated field becomes $\mathbf{E_{OPC}} = \mathbf{T}^T\mathbf{E_P}$. Among all the elements of $\mathbf{E_{OPC}}$, the first element represents the electric field at the focus, which can be calculated by

$$E_{\mathrm{peak}} = \sum_{m=1}^{N} a_{m1}\mathrm{BP}\left(a_{m1}\right). \tag{S3.2}$$

Thus, the intensity of the focus is calculated by

$$\begin{aligned} I_{\mathrm{peak}} &= \left\langle \left|E_{\mathrm{peak}}\right|^2 \right\rangle \\ &= \left| \frac{N}{2\pi\sigma^2} \int_{-\infty}^{+\infty}\int_{-\infty}^{+\infty} dxdy\left(x+iy\right)\left[\theta\left(y\right)-\theta\left(-y\right)\right] e^{-\left(x^2+y^2\right)/\left(2\sigma^2\right)} \right|^2, \\ &= \left| \frac{iN}{2\pi\sigma^2} \int_{-\infty}^{+\infty}\int_{-\infty}^{+\infty} dxdy\left[y\theta\left(y\right)-y\theta\left(-y\right)\right] e^{-\left(x^2+y^2\right)/\left(2\sigma^2\right)} \right|^2, \\ &= \left| \frac{2iN}{\sqrt{2\pi\sigma^2}} \int_{0}^{+\infty} dyye^{-y^2/\left(2\sigma^2\right)} \right|^2, \\ &= \left| \frac{2iN\sigma}{\sqrt{2\pi}}\Gamma\left(1\right) \right|^2 = \frac{2}{\pi}\sigma^2 N^2, \end{aligned} \tag{S3.3}$$

where $\theta(\cdot)$ is the Heaviside step function, $\Gamma(x)=\int_0^{+\infty} t^{x-1}e^{-t}dt$ is the gamma function, and $\langle\bullet\rangle$ denotes ensemble averaging. In the above derivation, we have converted the summation into an integration. Moreover, for the matrix element a_{ij}, we have used the fact that both its real part (*x*) and its imaginary part (*y*) obey the same Gaussian distribution with a mean of zero and a standard deviation of σ.

The remaining elements of **E_{OPC}** represent the fields of the background, and are calculated by $E_{\text{background}}=\sum_{m=1}^{N} a_{mn}\text{BP}\left(a_{m1}\right),\ n\neq 1.$ Thus, the background intensity can be obtained by

$$\begin{aligned}
I_{\text{background}} &= \left\langle \left| \sum_{m=1}^{N} a_{mn}\text{BP}\left(a_{m1}\right) \right|^2 \right\rangle, n\neq 1,\\
&= N\text{Var}\left(a_{mn}\text{BP}(a_{m1})\right),\\
&= N\text{Var}(a_{mn})\text{Var}\left(\text{BP}(a_{m1})\right),\\
&= N\times 2\sigma^2\times 1\\
&= 2\sigma^2 N, \qquad \text{(S3.4)}
\end{aligned}$$

where $\text{Var}(\bullet)$ sums the variances of both the real part and the imaginary part of a random variable. Combining the results given by Eqs. (S3.3) and (S3.4), we obtain the theoretical PBR of the focus achieved with binary-phase modulation:

$$\text{PBR}_1 = I_{\text{peak}}/I_{\text{background}} = \frac{1}{\pi}N. \qquad \text{(S3.5)}$$

When there are *M* input modes, it can be proved that the theoretical PBR is scaled down by a factor of *M*:

$$\text{PBR}_M = \frac{1}{\pi}\frac{N}{M}. \qquad \text{(S3.6)}$$

When a scattering medium is sufficiently thick, polarization can be completely scrambled by scattering. However, DOPC systems, except the one presented in Ref. [34], phase-conjugates only a single polarization of the sample light. In this case, by using a vector transmission matrix in the derivation [34, 100], we can find that the PBRs derived in Eqs. (S3.5) and (S3.6) are reduced by half. Such a PBR reduction can be understood by considering the background elevation due to the field polarized orthogonally to the incident polarization direction.

Relationship between the PBR and the speckle correlation time when there are multiple input modes

For dynamic scattering media, the influence of speckle decorrelation on the PBR of a DOPC-achieved focus was studied in Ref. [86]. However, only a single input mode was considered in the authors' derivation. As time-reversed ultrasonically encoded (TRUE) optical focusing typically encounters a large number of input modes *M*, we extend the previous work to the case of *M* greater than 1. We also derive the relationship between the PBR and the speckle correlation time τ_{c}.

Consider an incident field $\mathbf{E}_{\mathbf{in}}(t) = (p_1\ p_2\ \cdots p_M\ 0 \cdots 0)^T_{S\times 1}$ which has *M* non-zero elements. After passing through a scattering medium, the scattered light field $\mathbf{E}_{\mathbf{S}}(t)$ can be calculated by

$$\mathbf{E}_{\mathbf{S}}(t) = \mathbf{T}(t)\mathbf{E}_{\mathbf{in}}(t) = \begin{pmatrix} a_{11}(t) & a_{12}(t) & \cdots & a_{1S}(t) \\ a_{21}(t) & a_{22}(t) & \cdots & a_{2S}(t) \\ \vdots & \vdots & & \vdots \\ a_{N1}(t) & a_{N2}(t) & \cdots & a_{NS}(t) \end{pmatrix}_{N\times S} \begin{pmatrix} p_1 \\ \vdots \\ p_M \\ 0 \\ \vdots \\ 0 \end{pmatrix}_{S\times 1}$$

$$
=\begin{pmatrix} a_{11}(t)\,p_1+a_{12}(t)\,p_2+\cdots+a_{1M}(t)\,p_M \\ a_{21}(t)\,p_1+a_{22}(t)\,p_2+\cdots+a_{2M}(t)\,p_M \\ \vdots \\ a_{N1}(t)\,p_1+a_{N2}(t)\,p_2+\cdots+a_{NM}(t)\,p_M \end{pmatrix}_{N\times 1}. \qquad \text{(S3.7)}
$$

Hence, the first-order correlation function of the light field of the *i*-th output mode can be calculated by

$$
g^{(1)}(\tau)=\frac{\left\langle E^*(t)E(t+\tau)\right\rangle_t}{\sqrt{\left\langle |E(t)|^2\right\rangle_t}\sqrt{\left\langle |E(t+\tau)|^2\right\rangle_t}}
$$

$$
=\frac{\left\langle\left[a_{i1}(t)\,p_1+a_{i2}(t)\,p_2+\cdots+a_{iM}(t)\,p_M\right]^*\left[a_{i1}(t+\tau)\,p_1+a_{i2}(t+\tau)\,p_2+\cdots+a_{iM}(t+\tau)\,p_M\right]\right\rangle_t}{\left\langle\left[a_{i1}(t)\,p_1+a_{i2}(t)\,p_2+\cdots+a_{iM}(t)\,p_M\right]^*\left[a_{i1}(t)\,p_1+a_{i2}(t)\,p_2+\cdots+a_{iM}(t)\,p_M\right]\right\rangle_t}, \qquad \text{(S3.8)}
$$

where $\langle\bullet\rangle_t$ takes an ensemble average over time, and we assume the random process is stationary and ergodic. Since $\langle a_{ij}(t)a_{ik}(t)\rangle_t=\langle a_{ij}(t)a_{ik}(t+\tau)\rangle_t=0$ for any $j\neq k$, we have

$$
g^{(1)}(\tau)=\frac{\left\langle\left[a_{i1}{}^*(t)a_{i1}(t+\tau)|p_1|^2+a_{i2}{}^*(t)a_{i2}(t+\tau)|p_2|^2+\cdots+a_{iM}{}^*(t)a_{iM}(t+\tau)|p_M|^2\right]\right\rangle_t}{\left\langle\left[a_{i1}{}^*(t)a_{i1}(t)|p_1|^2+a_{i2}{}^*(t)a_{i2}(t)|p_2|^2+\cdots+a_{iM}{}^*(t)a_{iM}(t)|p_M|^2\right]\right\rangle_t}
$$

$$
=\frac{\frac{1}{M}\left(|p_1|^2+|p_2|^2+\cdots+|p_M|^2\right)M\overline{a^*(t)a(t+\tau)}}{\frac{1}{M}\left(|p_1|^2+|p_2|^2+\cdots+|p_M|^2\right)M\overline{a^*(t)a(t)}}
$$

$$
=\frac{\overline{a^*(t)a(t+\tau)}}{\overline{a^*(t)a(t)}}, \qquad \text{(S3.9)}
$$

where $\overline{A}$ denotes the mean of random variable *A*, and $a(t)$ denotes a random variable that follows a circular Gaussian distribution. For the second equality, we used the fact that $|p|^2$ and $a^*(t)a(t+\tau)$ are independent.

After passing through the scattering medium, the phase-conjugated light field at $t+\tau$ is computed as

$$\begin{aligned}\mathbf{E}_{\mathbf{OPC}}\left(t+\tau\right)&=\left[\mathbf{T}\left(t+\tau\right)\right]^{T}\mathbf{E}_{\mathbf{S}}^{*}\left(t\right)\\&=\begin{pmatrix}a_{11}\left(t+\tau\right) & a_{21}\left(t+\tau\right) & \cdots & a_{N1}(t+\tau)\\ a_{12}\left(t+\tau\right) & a_{22}\left(t+\tau\right) & \cdots & a_{N2}(t+\tau)\\ \vdots & \vdots & & \vdots\\ a_{1S}\left(t+\tau\right) & a_{2S}\left(t+\tau\right) & \cdots & a_{NS}(t+\tau)\end{pmatrix}\begin{pmatrix}a_{11}\left(t\right)p_{1}+a_{12}\left(t\right)p_{2}+\cdots+a_{1M}\left(t\right)p_{M}\\ a_{21}\left(t\right)p_{1}+a_{22}\left(t\right)p_{2}+\cdots+a_{2M}\left(t\right)p_{M}\\ \vdots\\ a_{N1}\left(t\right)p_{1}+a_{N2}\left(t\right)p_{2}+\cdots+a_{NM}\left(t\right)p_{M}\end{pmatrix}^{*}.\end{aligned}\tag{S3.10}$$

So, the *i*-th element of $\mathbf{E}_{\mathbf{OPC}}\left(t+\tau\right)$ can be calculated by

$$\begin{aligned}E_{\mathrm{OPC}i}\left(t+\tau\right)&=(a_{1i}\left(t+\tau\right)\ a_{2i}\left(t+\tau\right)\ \cdots\ a_{Ni}(t+\tau))\begin{pmatrix}\sum_{j=1}^{M}a_{1j}^{*}\left(t\right)p_{j}^{*}\\ \sum_{j=1}^{M}a_{2j}^{*}\left(t\right)p_{j}^{*}\\ \vdots\\ \sum_{j=1}^{M}a_{Nj}^{*}\left(t\right)p_{j}^{*}\end{pmatrix}\\&=\sum_{k=1}^{N}a_{ki}\left(t+\tau\right)\sum_{j=1}^{M}a_{kj}^{*}\left(t\right)p_{j}^{*}=\sum_{k=1}^{N}\sum_{j=1}^{M}a_{ki}\left(t+\tau\right)a_{kj}^{*}\left(t\right)p_{j}^{*}.\end{aligned}\tag{S3.11}$$

Then, we have

$$\left\langle E_{\mathrm{OPC}i}\left(t+\tau\right)\right\rangle_{t}=\left\langle\sum_{k=1}^{N}a_{ki}\left(t+\tau\right)a_{ki}^{*}\left(t\right)p_{i}^{*}\right\rangle_{t}=p_{i}^{*}N\overline{a^{*}\left(t\right)a\left(t+\tau\right)}.\tag{S3.12}$$

Thus, the ratio of the PBRs at time *t* and $t+\tau$ can be calculated by

$$\frac{\mathrm{PBR}\left(t+\tau\right)}{\mathrm{PBR}\left(t\right)}=\frac{\sum_{i=1}^{M}I_{\mathrm{OPC}i}\left(t+\tau\right)}{\sum_{i=1}^{M}I_{\mathrm{OPC}i}\left(t\right)}=\frac{\sum_{i=1}^{M}\left|\left\langle E_{\mathrm{OPC}i}\left(t+\tau\right)\right\rangle_{t}\right|^{2}}{\sum_{i=1}^{M}\left|\left\langle E_{\mathrm{OPC}i}\left(t\right)\right\rangle_{t}\right|^{2}}=\left|\frac{\overline{a^{*}\left(t\right)a\left(t+\tau\right)}}{\overline{a^{*}\left(t\right)a\left(t\right)}}\right|^{2}.\tag{S3.13}$$

Based on Eqs. (S3.9) and (S3.13), we get

$$\frac{\mathrm{PBR}(t+\tau)}{\mathrm{PBR}(t)}=\left|g^{(1)}(\tau)\right|^2. \tag{S3.14}$$

On the other hand, the correlation coefficient R_I of two speckle patterns $I(\vec{r},t)$ and $I(\vec{r},t+\tau)$, recorded at t and $t+\tau$, is defined as

$$R_\mathrm{I}(\tau)=\frac{\left\langle\left(I(\vec{r},t)-\left\langle I(\vec{r},t)\right\rangle_{\vec{r}}\right)\left(I(\vec{r},t+\tau)-\left\langle I(\vec{r},t+\tau)\right\rangle_{\vec{r}}\right)\right\rangle_{\vec{r}}}{\sqrt{\left\langle\left[I(\vec{r},t)-\left\langle I(\vec{r},t)\right\rangle_{\vec{r}}\right]^2\right\rangle_{\vec{r}}}\sqrt{\left\langle\left[I(\vec{r},t+\tau)-\left\langle I(\vec{r},t+\tau)\right\rangle_{\vec{r}}\right]^2\right\rangle_{\vec{r}}}}, \tag{S3.15}$$

where $\langle\bullet\rangle_{\vec{r}}$ takes an average over all the pixels. We assume the random process is stationary, then,

$$\begin{aligned}R_\mathrm{I}(\tau)&=\frac{\left\langle\left(I(\vec{r},t)-\left\langle I(\vec{r},t)\right\rangle_{\vec{r}}\right)\left(I(\vec{r},t+\tau)-\left\langle I(\vec{r},t+\tau)\right\rangle_{\vec{r}}\right)\right\rangle_{\vec{r}}}{\left\langle\left[I(\vec{r},t)-\left\langle I(\vec{r},t)\right\rangle_{\vec{r}}\right]^2\right\rangle_{\vec{r}}}\\&=\frac{\left\langle\left(I(\vec{r},t)-\left\langle I(\vec{r},t)\right\rangle_{\vec{r}}\right)\left(I(\vec{r},t+\tau)-\left\langle I(\vec{r},t+\tau)\right\rangle_{\vec{r}}\right)\right\rangle_{\vec{r}}}{\left[\left\langle I(\vec{r},t)\right\rangle_{\vec{r}}\right]^2},\end{aligned} \tag{S3.16}$$

where the last equal sign holds because $\sqrt{\left\langle\left[I(\vec{r},t)-\left\langle I(\vec{r},t)\right\rangle_{\vec{r}}\right]^2\right\rangle_{\vec{r}}}=\left\langle I(\vec{r},t)\right\rangle_{\vec{r}}$ for polarized fully developed speckles [101].

For a given output mode, the second-order correlation function of light is written as

$$\begin{aligned}g^{(2)}(\tau)&=\frac{\left\langle I(t)I(t+\tau)\right\rangle_t}{\left\langle I(t)\right\rangle_t\left\langle I(t+\tau)\right\rangle_t}=\frac{\left\langle I(t)I(t+\tau)\right\rangle_t}{\left[\left\langle I(t)\right\rangle_t\right]^2}=\frac{\left\langle I(t)I(t+\tau)\right\rangle_t-\left[\left\langle I(t)\right\rangle_t\right]^2}{\left[\left\langle I(t)\right\rangle_t\right]^2}+1\\&=\frac{\left\langle\left(I(t)-\left\langle I(t)\right\rangle_t\right)\left(I(t+\tau)-\left\langle I(t+\tau)\right\rangle_t\right)\right\rangle_t}{\left[\left\langle I(t)\right\rangle_t\right]^2}+1.\end{aligned} \tag{S3.17}$$

Because of ergodicity, the ensemble average over time for the intensity of one output mode in Eq. (S3.17) can be calculated by averaging the intensities over all output modes (camera pixels). Then, from Eqs. (S3.16) and (S3.17), we have

$$g^{(2)}(\tau)=R_{\mathrm{I}}(\tau)+1. \tag{S3.18}$$

According to the Siegert relation, we have

$$g^{(2)}(\tau)=\beta\left|g^{(1)}(\tau)\right|^{2}+1, \tag{S3.19}$$

where β is a constant depending on the experimental conditions. From Eqs. (3.18) and (3.19), we get

$$R_{\mathrm{I}}(\tau)=\beta\left|g^{(1)}(\tau)\right|^{2}. \tag{S3.20}$$

Based on the results in Eqs. (S3.14) and (S3.20), we obtain

$$\frac{\mathrm{PBR}(t+\tau)}{\mathrm{PBR}(t)}=\frac{1}{\beta}R_{\mathrm{I}}(\tau). \tag{S3.21}$$

Eq. (S3.21) shows that the PBR is proportional to the correlation coefficient R_{I} of speckle patterns. From Eq. (S3.18), for polarized fully developed speckles, $R_{\mathrm{I}}(t,\tau_{\mathrm{c}})=g^{(2)}(\tau)-1=\exp(-2t^{2}/\tau_{\mathrm{c}}{}^{2})$ [24, 58, 59], so we get

$$\mathrm{PBR}(t,\tau_{\mathrm{c}})=A\exp(-2t^{2}/\tau_{\mathrm{c}}{}^{2}), \tag{S3.22}$$

where $A=\mathrm{PBR}(t/\tau_{\mathrm{c}}\to 0)/\beta$, and $\mathrm{PBR}(t/\tau_{\mathrm{c}}\to 0)$ is the PBR achieved when the system runtime is infinitely small compared with the speckle correlation time of the sample.

Chapter 4: Improving the quality of the focus achieved by optical phase conjugation (OPC)

4.1 Full-polarization digital OPC

4.1.1 Introduction

When the scattering medium is optically thick, the polarization of the scattered light becomes spatially randomized and its representation on the Poincare sphere is distributed randomly and evenly. Thus, in any OPC experiment, it is ideal to first record all the information about the scattered light, including its phase, amplitude, and polarization at all positions. Next, to rigorously follow the time-reversal principle, scattered light needs to be phase conjugated with the original position-dependent polarizations maintained. Using a nonlinear crystal, a full-polarization analog OPC system has been developed to restore images through multimode fibers [102]. However, in practice, the SLMs used in digital OPC (DOPC) systems can modulate only linearly polarized light along a fixed direction, and thus are incapable of faithfully phase-conjugating scattered light with different polarization states. To address this problem, we have developed the first full-polarization DOPC system which is able to record and phase-conjugate light with random polarizations.

4.1.2 Methods

The process of full-polarization DOPC includes a recording step and a playback step (Fig. 4.1). In the recording step [Fig. 4.1(a)], as a concrete example, the incident light $E^{(1)}(x, y)$ is chosen to be a narrow collimated beam with a linear polarization. The light then passes through a scattering medium and evolves into a fully developed speckle pattern on the x'-y' plane, with spatially non-uniform polarizations. In order to record the information about scattered light with various polarizations, the scattered light is decomposed into two components: $E_{\mathrm{H}}^{(2)}(x', y')$ and $E_{\mathrm{V}}^{(2)}(x', y')$, and both are recorded using phase shifting holography [74]. Here, “H” denotes the horizontal polarization and “V” denotes the vertical polarization, and they form complete orthogonal bases that can represent an arbitrary polarization state. This procedure is superior to existing DOPC approaches, where only one component (either “H” or “V”) is recorded and phase conjugated. In general, the speckle patterns corresponding to the two orthogonal polarizations bear little resemblance, and the polarizations at two arbitrary positions that are not within the same speckle grain, i.e., position 1 and position 2 [Fig. 4.1(a)], are completely uncorrelated in both amplitude ratio $[|E_{\mathrm{H}}^{(2)}(x_1', y_1')| / |E_{\mathrm{V}}^{(2)}(x_1', y_1')| \neq |E_{\mathrm{H}}^{(2)}(x_2', y_2')| / |\mathrm{E}_{\mathrm{V}}^{(2)}(x_2', y_2')|]$ and relative phase $[\Delta\phi_1 = \arg(E_{\mathrm{H}}^{(2)}(x_1', y_1')/E_{\mathrm{V}}^{(2)}(x_1', y_1')) \neq \Delta\phi_2 = \arg(E_{\mathrm{H}}^{(2)}(x_2', y_2')) / E_{\mathrm{V}}^{(2)}(x_2', y_2'))]$. Here, $|\cdot|$ denotes taking the absolute value and $\arg(\cdot)$ denotes taking the argument. Next, in the playback step [Fig. 4.1(b)], both OPC fields, with orthogonal polarizations, are produced and directed to the scattering medium. After they pass through the scattering medium, an output collimated beam that is phase-conjugated to the input beam is obtained.

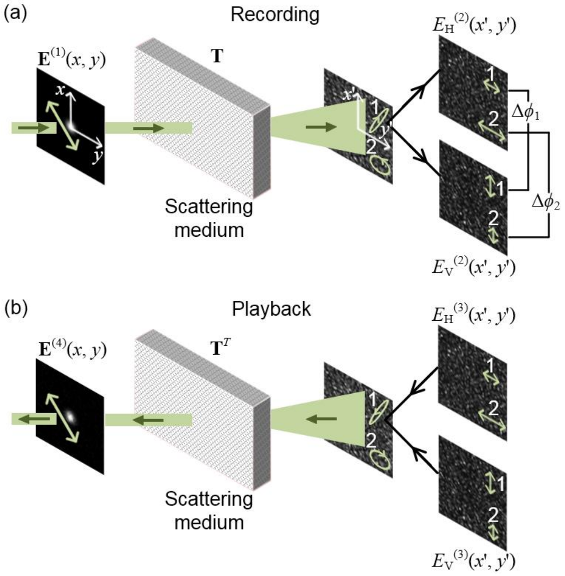

Figure 4.1 Schematic of the processes in full-polarization DOPC. (a) In the recording step, the scattered light is recorded along the horizontal (H) and vertical (V) polarization directions. (b) In the playback step, OPC fields along

the two orthogonal polarizations are produced and become phase-conjugated to the input light field after passing through the scattering medium.

We theoretically studied full-polarization DOPC by extending the existing scalar-field-based random matrix theory [57]. The input light field $\mathbf{E}^{(1)}(x, y)$ is expressed as a Jones column vector concatenated by two components $E_{\mathrm{H}}{}^{(1)}(x, y)$ and $E_{\mathrm{V}}{}^{(1)}(x, y)$:

$$\mathbf{E}^{(1)}(x,y)=\begin{pmatrix} E_{\mathrm{H}}{}^{(1)}(x,y) \\ E_{\mathrm{V}}{}^{(1)}(x,y) \end{pmatrix}_{2N\times 1}, \tag{4.1}$$

where each component comprises N spatial modes and is represented by an $N\times 1$ column vector. Since light transmission through the scattering medium and the subsequent optics is represented by a vector transmission matrix $\mathbf{T}$ [100, 103], the scattered light field on the SLM $\mathbf{E}^{(2)}(x',y')=\begin{pmatrix} E_{\mathrm{H}}{}^{(2)}(x',y') \\ E_{\mathrm{V}}{}^{(2)}(x',y') \end{pmatrix}_{2N\times 1}$ can be calculated as

$$\mathbf{E}^{(2)}(x',y')=\mathbf{T}\mathbf{E}^{(1)}(x,y). \tag{4.2}$$

Specifically, the vector transmission matrix T has the following form:

$$\mathbf{T}=\begin{pmatrix} \mathbf{T}_{\mathrm{HH}} & \mathbf{T}_{\mathrm{HV}} \\ \mathbf{T}_{\mathrm{VH}} & \mathbf{T}_{\mathrm{VV}} \end{pmatrix}_{2N\times 2N}, \tag{4.3}$$

in which $\mathbf{T}_{\mathrm{AB}}$ (A, B = H, V) is an N-by-N matrix that connects the input field with B polarization and the scattered field with A polarization. By using singular value decomposition, each $\mathbf{T}_{\mathrm{AB}}$ can be further decomposed as $\mathbf{T}_{\mathrm{AB}} = \mathbf{U}_{\mathrm{AB}}\mathbf{t}_{\mathrm{AB}}\mathbf{V}_{\mathrm{AB}}$, where $\mathbf{U}_{\mathrm{AB}}$ and $\mathbf{V}_{\mathrm{AB}}$ are independent unitary matrices. Physically, $\mathbf{U}_{\mathrm{AB}}$ and $\mathbf{V}_{\mathrm{AB}}$ are transformation matrices converting between coordinates in Cartesian bases and eigenmode bases. $\mathbf{t}_{\mathrm{AB}}$ is a diagonal matrix with non-negative elements, and each element quantifies the transmission coefficient of each eigenmode. Thus,

$\tau_{\mathrm{AB}} = \mathrm{tr}\left(\mathbf{t}_{\mathrm{AB}}^{2}\right) / N$ represents the average power transmission from polarization B to polarization A, where tr(·) denotes taking the trace of a matrix. In practice, only a fraction of the transmitted light is measured. Under this condition, the elements in each T_{AB} can be approximated by the corresponding circular Gaussian distributions [57].Thus, for scattering media that are sufficiently thick to randomize the polarization state, $\mathbf{T}_{\mathrm{AB}}\mathbf{T}_{\mathrm{AB}}^{\dagger} \approx \tau_{\mathrm{AB}}\,\mathrm{I}$, where the symbol † represents the adjoint of a matrix and I is an identity matrix. The playback OPC field is phase-conjugated to the recorded field:

$$\mathbf{E}^{(3)}(x', y') = \left[\mathbf{E}^{(2)}(x', y')\right]^{*}, \tag{4.4}$$

where the symbol * denotes complex conjugation. This field is sent back to pass through the scattering medium again. Finally, the output field $\mathbf{E}^{(4)}(x, y) = \begin{pmatrix} E_{\mathrm{H}}{}^{(4)}(x, y) \\ E_{\mathrm{V}}{}^{(4)}(x, y) \end{pmatrix}$ after scattering is estimated by

$$\mathbf{E}^{(4)}(x, y) = \mathbf{T}^{T}\mathbf{E}^{(3)}(x', y'), \tag{4.5}$$

where the scattering matrix is modeled by the transpose of the forward transmission matrix. Combining Eqs. (4.1)-(4.5) yields

$$\mathbf{E}^{(4)}(x, y) \approx \begin{pmatrix} (\tau_{\mathrm{HH}} + \tau_{\mathrm{VH}})[E_{\mathrm{H}}{}^{(1)}(x, y)]^{*} \\ (\tau_{\mathrm{HV}} + \tau_{\mathrm{VV}})[E_{\mathrm{V}}{}^{(1)}(x, y)]^{*} \end{pmatrix} + \begin{pmatrix} (\mathbf{M}_{\mathrm{VHH}} + \mathbf{M}_{\mathrm{VVH}})[E_{\mathrm{V}}{}^{(1)}(x, y)]^{*} \\ (\mathbf{M}_{\mathrm{HHV}} + \mathbf{M}_{\mathrm{HVV}})[E_{\mathrm{H}}{}^{(1)}(x, y)]^{*} \end{pmatrix}. \tag{4.6}$$

Here, the first term on the right-hand side of Eq. (4.6) represents the phase-conjugated light, and the second term represents a background due to polarization coupling in partial OPC. Specifically, matrices $\mathbf{M}_{\mathrm{ABC}} \equiv \mathbf{T}_{\mathrm{BC}}^{T}\mathbf{T}_{\mathrm{BA}}^{*}$ with A, B, C = H, V and A ≠ C describe the mapping from the input light with A polarization to the scattered light with B polarization, followed by the mapping from the scattered light with B polarization to the output light with C polarization. The modulus of each element in $\mathbf{M}_{\mathrm{ABC}}$ is $O(1/N^{1/2})$. Physically, ($\tau_{\mathrm{HH}} + \tau_{\mathrm{VH}}$) and ($\tau_{\mathrm{HV}} + \tau_{\mathrm{VV}}$) are the total transmittances of the scattering medium when the incident light is purely horizontally polarized or purely vertically polarized, respectively. For most scattering media, these two values are very close. Therefore, $\mathbf{E}^{(4)(}x, y) \approx \beta\mathbf{E}^{(1)}(x, y)^*$, where $\beta = (\tau_{\mathrm{HH}} + \tau_{\mathrm{VH}})$ [or ($\tau_{\mathrm{HV}} + \tau_{\mathrm{VV}}$)] is a positive number. So, the full-polarization DOPC process faithfully produces the phase-conjugated field of the input light. However, if the DOPC process phase-conjugates scattered light only along the horizontal polarization direction (referred to as single-polarization DOPC), the output field is calculated as

$$\mathbf{E}^{(4)}(x,y)|_{\mathrm{H}} \approx \begin{pmatrix} \tau_{\mathrm{HH}}[E_{\mathrm{H}}{}^{(1)}(x,y)]^* \\ \tau_{\mathrm{HV}}[E_{\mathrm{V}}{}^{(1)}(x,y)]^* \end{pmatrix} + \begin{pmatrix} \mathbf{M}_{\mathrm{VHH}}[E_{\mathrm{V}}{}^{(1)}(x,y)]^* \\ \mathbf{M}_{\mathrm{HHV}}[E_{\mathrm{H}}{}^{(1)}(x,y)]^* \end{pmatrix}. \tag{4.7}$$

Again, the first term on the right hand side of Eq. (4.7) represents the phase-conjugated light, while the second term corresponds to the background. In cases when τ_{HH} and τ_{HV} are not the same, the resultant field is not phase-conjugated to the input light field.

To compare the performance of full-polarization DOPC and single-polarization DOPC, we performed numerical simulations based on the above matrix analysis. In the simulation, N was set to be 2500, and the input light was chosen to be horizontally polarized with the central pixel being 1 for the electric field amplitude and the other pixels being 0. Each element in the transmission matrix $\mathbf{T}_{\mathrm{AB}}$ was drawn from a circular Gaussian distribution with mean $\mu = 0$ and variance $\sigma^2 = \tau_{\mathrm{AB}}$. Specifically, τ_{HH} was varied from 0 to 1, and we assumed $\tau_{\mathrm{VV}} = \tau_{\mathrm{HH}}$ and $\tau_{\mathrm{HV}} = \tau_{\mathrm{VH}} = 1 - \tau_{\mathrm{HH}}$. Figure 4.2 plots the peak-to-background ratio (PBR) normalized by N as a function of the polarization coupling coefficient α. PBR is defined as the ratio between the average intensities within and outside the targeted region of the phase-conjugated light; α

quantifies the average energy transfer between the two orthogonal polarizations, and is defined as

$$\alpha \equiv \tau_{\mathrm{VH}} / (\tau_{\mathrm{HH}} + \tau_{\mathrm{VH}}). \tag{4.8}$$

Figure 4.2 shows that the normalized PBRs for full-polarization DOPC are 1 for all values of α. In contrast, the normalized PBRs for single polarization DOPC change linearly with α. Such an observation is in accord with the theoretical expression of the normalized PBRs for single-polarization DOPC (= $1 - \alpha$ and α for horizontal and vertical polarization DOPC respectively, which can be derived by following the same procedures in [57] but using the vector transmission matrix). Specifically, when α approaches 0.5, the PBRs achieved by horizontal-polarization DOPC and vertical-polarization DOPC are the same, and they are half of the PBR achieved by full polarization DOPC. An intuitive explanation is that in the full polarization scenario, the peak intensity is enhanced by a factor of 4 due to constructive interference, while the background is doubled by summing the background intensities corresponding to the two orthogonal polarizations. When α approaches 0 or 1, if the correct polarization state is not chosen to record and phase-conjugate the scattered light, the PBR of single polarization DOPC can become extremely low. In practice, $\alpha \sim 1$ corresponds to a strongly birefringent sample with a small optical thickness, such as the retina of the eye [104]. Based on the above analysis, it is highly desired to develop a full-polarization DOPC system. The performance of such a system is not sensitive to the properties of the scattering media, and the system can always achieve a higher PBR than that achieved by single-polarization DOPC systems.

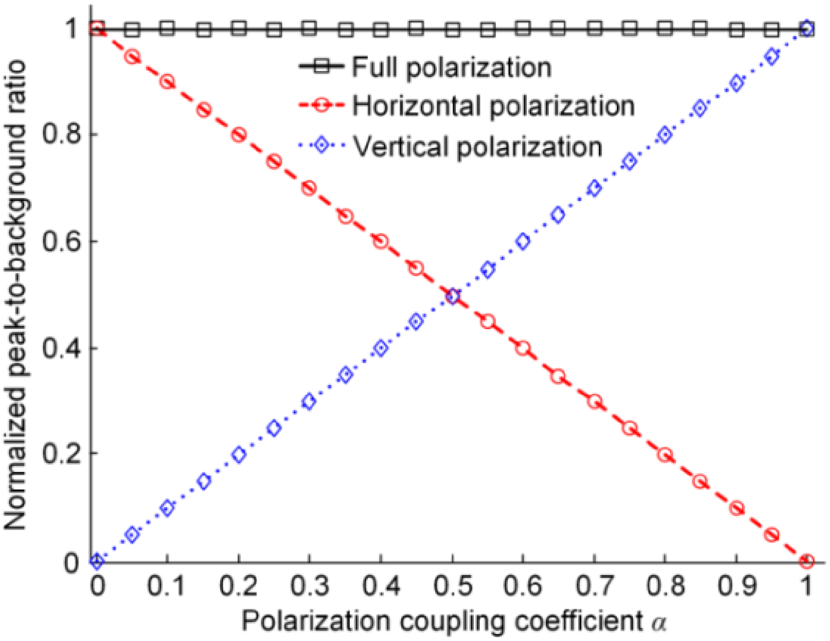

Figure 4.2 The normalized peak-to-background ratio as a function of the polarization coupling coefficient α for three different DOPC schemes. Discrete data points are from numerical simulation results, while the lines are plotted using analytical expressions.

Based on the positive results from the numerical simulations, we developed a full-polarization DOPC system schematically shown in Fig. 4.3. In the phase recording step, the input light was split into a planar reference beam (R) and a sample beam (S) by a polarizing beamsplitter (PBS); R was vertically polarized and S was horizontally polarized. Each beam was subsequently modulated by an acousto-optic modulator to induce a 12 Hz frequency difference between R and S. The polarization direction of R was then rotated by a half wave plate (HWP) to 45 degrees. In the sample arm, S illuminated an ex vivo chicken breast tissue slice, and its polarization state became spatially inhomogeneous after tissue scattering. Then, the two beams were combined by a 50:50 beamspliter (BS) for interferometry. Since the scattered light took various polarization states, we used a PBS to spatially separate it into components with horizontal and vertical polarizations. Each component then impinged on the surface of an SLM whose pixels displayed all zeros at this step. Both SLMs had a resolution of 1920×1080 pixels, and were imaged onto a scientific complementary metal–oxide–semiconductor (sCMOS) camera (resolution 2560×2160) by a camera lens. Each pixel in the SLMs corresponded to one pixel on the sCMOS camera. To use a single camera to image both SLMs simultaneously, the SLMs were rotated 90 degrees clockwise. Since both SLMs could modulate light only with vertical polarization, HWP4 was inserted before SLM1 to rotate the polarization of the light to vertical direction. The phase maps corresponding to the horizontally polarized scattered light and the vertically polarized scattered light were measured using phase-shifting holography [31, 74], made possible by making the camera run at a frame rate of 48 Hz (=4×12 Hz).

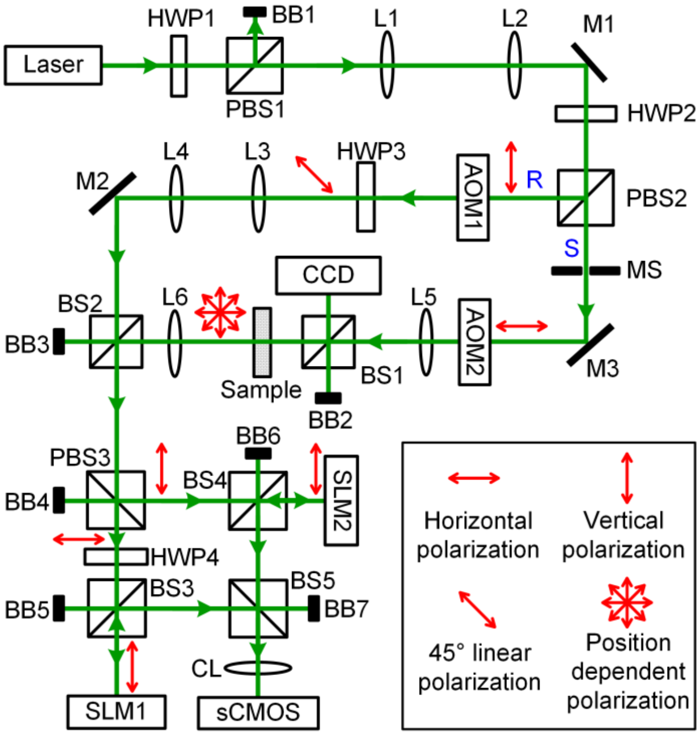

Figure 4.3 Schematic of the full-polarization DOPC set-up. Polarization states are indicated by the red arrows. AOM, acousto-optic modulator (AOM-505AF1, IntraAction); BB, beam block; BS, beamsplitter; CCD, CCD camera (GS3-U3-50S5M-C, Point Grey; pixel size 3.45 μm); CL, camera lens; HWP, half wave plate; L, lens; Laser, Verdi V5, Coherent, 532 nm; M, mirror; MS, mechanical shutter; PBS, polarizing beamspliter; R, reference beam; S, sample beam; sCMOS, scientific CMOS camera (pco.edge 5.5, pco; pixel size 6.5 μm); SLM, spatial light modulator (Pluto NIR-II, Holoeye; pixel size 8 μm).

In the playback step, the conjugate phase maps were displayed on the respective SLMs. An experimentally determined constant phase offset was added to one of the phase maps to compensate for the difference between the path length from PBS3 to SLM1 and from PBS3 to SLM2. The sample beam was blocked by a mechanical shutter in this step, and the planar reference beam illuminated the two SLMs to acquire the conjugate phase map. The two branches of phase conjugated light were then combined by PBS3 and were directed to the scattering sample. After they passed through the sample, a bright focus was formed on the focal plane of lens L5. To observe the focus, a 10:90 BS was inserted to create a copy of the focus, which was captured by a charge-coupled device (CCD) camera.

4.1.3 Results

In our experiment, we used 2 mm and 4 mm thick chicken breast tissue as scattering samples, and α was close to 0.5 for both samples, which is expected for thick scattering media. Images of the focal spots achieved by single-polarization DOPC and full-polarization DOPC are shown in Fig. 4.4. Specifically, Figs. 4.4(a), (b), and (c) show the imaged foci when only horizontal polarization, only vertical polarization, and full polarization were used for DOPC through 2 mm thick chicken breast tissue. All three images are shown using the same intensity scale. The peak intensity of the focus achieved by full-polarization DOPC is ~ 4 times as high as that achieved by single-polarization DOPC. Moreover, the PBRs for the three images are 141, 135, and 262, respectively. This result illustrates that the PBR achieved by full-polarization DOPC is roughly twice that achieved by single-polarization DOPC, which is in good agreement with our theoretical predictions. To better visualize the shape of the focus, each image is zoomed in and is normalized by its own peak intensity, as shown in Figs. 4.4 (d), (e), and (f). It can be seen that all three foci maintain nearly circular shapes, which shows that when the sample is not too thick, single-polarization DOPC can still achieve high OPC fidelity. For the 4 mm thick chicken tissue, the images of the foci achieved by horizontal polarization, vertical polarization, and full polarization DOPC are shown in Figs. 4.4 (g), (h), and (i), respectively. Again, the intensity of the focus achieved by full-polarization DOPC is roughly 4 times as high as that achieved by single-polarization DOPC. Due to the increased thickness, the PBRs for the three images are lower and are calculated to be 21, 18, and 37. However, full-polarization DOPC still approximately doubles the PBR achieved by single-polarization DOPC. Figures 4.4 (j), (k), and (l) show the enlarged images of the foci after normalization by their own peak intensities. Among all three foci, the one achieved by full-polarization DOPC has a nearly circular shape that most closely resembles the shape of the input focus. Such a result indicates that when the sample is thick, full-polarization DOPC can achieve higher OPC fidelity than that achieved by single-polarization DOPC [102]. We note that the increased size of the foci for 4 mm thick chicken tissue is due to different experimental conditions.

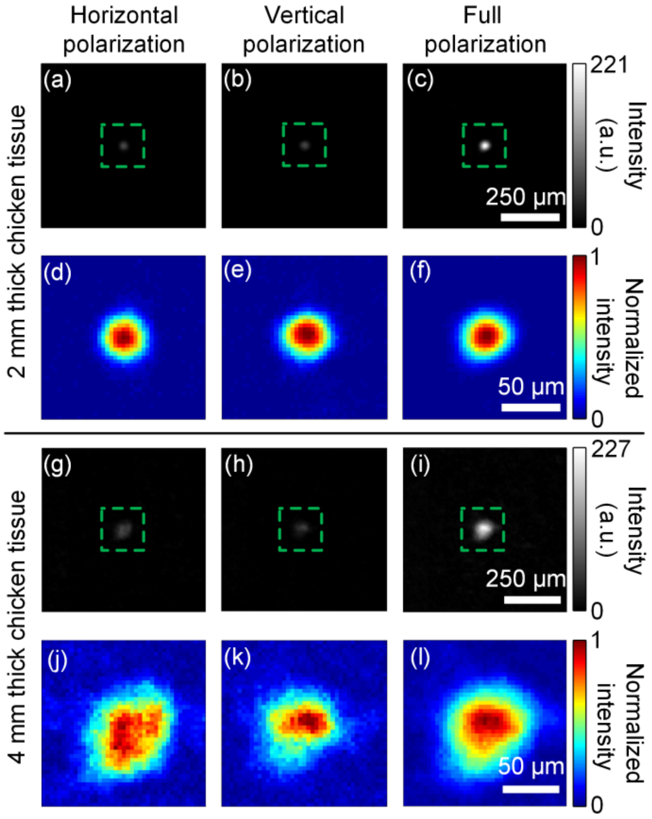

Figure 4.4 Images of the foci achieved by single-polarization and full-polarization DOPC. (a)-(c) Images of the foci through 2 mm thick chicken breast tissue when only horizontal-polarization, only vertical-polarization, and full-polarization DOPC were employed. (d)-(f) Enlarged images of (a)-(c). To better visualize the shape of the focus, each image is normalized by its own peak intensity. (g)-(i) Images of the foci through 4 mm thick chicken breast tissue when only horizontal-polarization, only vertical-polarization, and full-polarization DOPC were employed. (j)-(l) Enlarged images of (g)-(i). Again, to better visualize the shape of the focus, each image is normalized by its own peak intensity.

4.1.4 Discussion and Conclusion

Here, we briefly discuss the polarization states of the OPC field in our experiments. Currently, the two SLMs in the set-up modulate only the phase but not the amplitude of light. Thus, the SLM-generated OPC field before illuminating the sample does not have the same polarization as that of the scattered light. Nonetheless, compared with the ideal case when both phase and amplitude are modulated, due to the scrambling nature of the thick scattering medium, the phase-modulated light still constructively interferes in the same polarization state as that of the recording-phase input light (though the amplitude is reduced), while there is no constructive interference in the orthogonal polarization state. Thus, after the SLM-generated OPC field passes through the scattering medium, the polarization of the electric field at the focus is approximately the same as that of the input field. In our experiments, the input electric field at the focus was set to be horizontally polarized. Using a polarizer, we confirmed that the electric field at the focus achieved by full-polarization DOPC was also horizontally polarized.

In conclusion, we developed the first DOPC system that can record and phase-conjugate the scattered light with various polarization states. When the scattering sample is optically thick, our system doubles the PBR achieved by single-polarization DOPC systems, improves the OPC fidelity, and maintains the polarization of the input light field. The method described here can be easily applied to existing DOPC systems to improve their performance.

4.2 Sub-Nyquist sampling of speckle grains in digital OPC

4.2.1 Introduction

The pixel sizes of the digital cameras and SLMs constituting digital PCMs (several microns to tens of microns) are ~20 times larger than the wavelength of light, so speckle grains are under-sampled (sub-Nyquist sampled) if a PCM is placed adjacent to the rear surface of a thick scattering medium to collect more scattered light from the sample [Figs. 4.5(a) and (b)]. Since the Nyquist sampling criterion [105] is not followed, the phase map of the measured wavefront [Fig. 4.5(b)] looks different from the real one in Fig. 4.5(a). Such an under-sampled wavefront cannot be exactly time reversed, because it is not a proper representation of the true wavefront. Therefore, in all previous time-reversal–based optical focusing experiments, speckle grains are magnified [Fig. 4.5(c)] and are well-sampled by PCM pixels [Fig. 4.5(d)], to correctly measure the wavefront of the scattered light [26, 30, 80, 96, 106]. The measured wavefront is then used for phase conjugation.

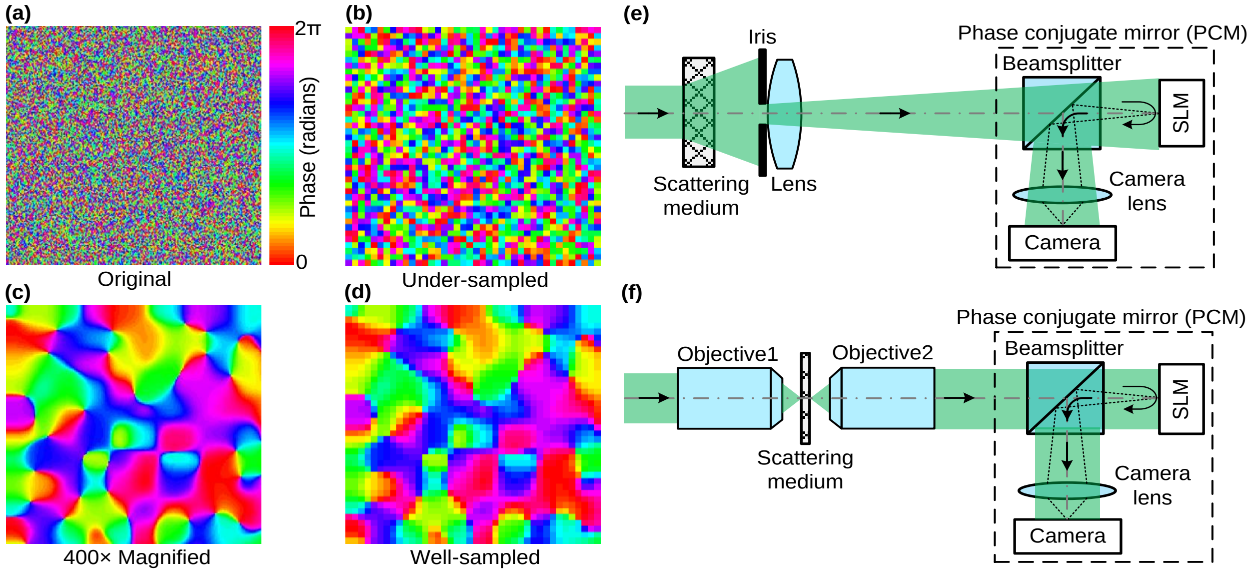

Figure 4.5 Sampling of speckle grains in optical time-reversal experiments. (a). Phase map of the scattered light on the rear surface of a scattering medium. (b). Phase map of the under-sampled speckle grains, which looks different from the real one in a. (c). Phase map of the 400× magnified speckle grains. (d). Phase map of the well-sampled speckle grains. (e). Magnifying the speckle size by an iris and a lens. (f). Magnifying the speckle size by two objective lenses.

However, two problems exist with well-sampling speckle grains in time-reversal–based optical focusing experiments. First, the SLM pixels are not efficiently used, since multiple pixels are correlated to represent a single speckle grain. When speckle grains are well-sampled, it has been proved [30] that the peak-to-background ratio (PBR) of the focus (with one speckle inside) is expected to follow

$$\mathrm{PBR} = N_S, \tag{4.9}$$

where N_S is the number of speckle grains intercepted by the PCM. The PBR is used to quantify the contrast of the focus and is defined as the ratio between the peak intensity of the focus and the average intensity of the speckles when a random wavefront is applied (background). Given that 3×3 pixels to 5×5 pixels have usually been used to sample one speckle grain in previous experiments [26, 30, 80, 96, 106], N_S is usually 9 – 25 times smaller than the pixel count of an SLM (N_P). Ideally, the PBR should be increased to N_p, so that all the degrees of freedom of an SLM can be utilized. Second, to ensure well-sampling speckle grains by magnifying the speckle size, a lens with an iris [82] [Fig. 4.5(e)], or two high-magnification objective lenses [20, 107, 108] [Fig. 4.5(f)], are usually employed, and the PCM is always placed far from the rear surface of the scattering medium. Consequently, these two approaches detect only a tiny portion of the scattered light exiting the sample and thus have much reduced light collection efficiencies. Moreover, magnifying the speckle size by focusing light onto a scattering medium with an objective [Fig. 4.5(f)] works only for thin samples.

In this work, we theoretically predict and experimentally verify that by under-sampling speckle grains, we can not only focus light through scattering media, but also significantly increase the PBR by 9 – 25 times, compared with that achieved with the conventional well-sampling conditions (3×3 to 5×5 pixels to sample one speckle grain on average). This discovery overturns the conventional belief that well-sampling speckle grains is required to achieve time-reversal–based optical focusing [26, 30, 80, 96, 106]. Besides improving the PBR, since our method does not require magnification of speckle grains, we remove the need to use an iris or objective lenses in the set-up and improve the light collection efficiency. We also proved that under-sampling speckle grains improves the signal-to-noise ratio (SNR) by at least 3 times.

4.2.2 Results

First, by analyzing the time-reversal process, we present a relatively simple argument to show that the expected PBR can be increased to the SLM pixel count N_P when speckle grains are under-sampled in optical time-reversal experiments. A rigorous proof can be found in

Supplementary notes. The incident light field $\mathbf{E_{in}}$ is represented by a vector with N_I elements, whose first element is set to 1, and the rest of the elements are set to 0 for simplicity without losing generality. The scattering medium is described by a transmission matrix $\mathbf{T}$ with dimensions of $N_\mathrm{S} \times N_\mathrm{I}$, whose element t_{ij} is independently drawn from a circular Gaussian distribution [101]. Hence, the scattered light field intercepted by a PCM is computed as

$$\mathbf{E_S} = \mathbf{TE_{in}} = \begin{pmatrix} t_{11} & t_{12} & \cdots & t_{1N_\mathrm{I}} \\ t_{21} & t_{22} & \cdots & t_{2N_\mathrm{I}} \\ \vdots & \vdots & \ddots & \vdots \\ t_{N_\mathrm{S}1} & t_{N_\mathrm{S}2} & \ldots & t_{N_\mathrm{S}N_\mathrm{I}} \end{pmatrix}_{N_\mathrm{S}\times N_\mathrm{I}} \begin{pmatrix} 1 \\ 0 \\ \vdots \\ 0 \end{pmatrix}_{N_\mathrm{I}\times 1} = \begin{pmatrix} t_{11} \\ t_{21} \\ \vdots \\ t_{N_\mathrm{S}1} \end{pmatrix}_{N_\mathrm{S}\times 1} . \tag{4.10}$$

Since speckle grains were well-sampled by a digital camera in previous digital optical phase conjugation experiments, each element of $\mathbf{E_S}$ can be accurately determined by phase-shifting holography [31, 74, 109]. However, when speckle grains are under-sampled, it is unclear what quantity is measured by phase-shifting holography and whether optical focusing using phase conjugation can still be achieved. In Supplementary notes, we first prove that when speckle grains are under-sampled, the reconstructed quantity of each pixel in phase-shifting holography is the summation of the electric fields of all the speckle grains within that pixel. As an illustration, Fig. 4.6(a) shows a case where 16 speckle grains are within one pixel. Each speckle grain is assumed to have the same size and shape for simplicity, and the amplitude and the phase of its electric field are represented by the length and the angle of an arrow (the phasor expression). The phase is also encoded by color for better visualization. Using phase-shifting holography, the reconstructed quantity for this pixel equals the summation of the electric fields of all 16 speckle grains [Fig. 4.6(b)]. We emphasize that it is this field summation, rather than intensity summation, that retains the field information of each speckle grain (although not resolved) and makes optical focusing achievable. With the knowledge that phase-shifting holography measures the summation of the electric fields of all the speckle grains within one pixel, the experimentally measurable scattered field $\mathbf{E}_{\mathbf{S,under\text{-}sampled}}$ has the following form when F speckle grains occupy one camera pixel on average:

$$\mathbf{E}_{\mathbf{S,under\text{-}sampled}} = \begin{pmatrix} \left.\begin{matrix} t_{11}+t_{21}+\cdots+t_{F1} \\ t_{11}+t_{21}+\cdots+t_{F1} \\ \vdots \\ t_{11}+t_{21}+\cdots+t_{F1} \end{matrix}\right\} F \text{ rows} \\ \vdots \\ \left.\begin{matrix} t_{N_\mathrm{S}-F+1,1}+t_{N_\mathrm{S}-F+2,1}+\cdots+t_{N_\mathrm{S},1} \\ t_{N_\mathrm{S}-F+1,1}+t_{N_\mathrm{S}-F+2,1}+\cdots+t_{N_\mathrm{S},1} \\ \vdots \\ t_{N_\mathrm{S}-F+1,1}+t_{N_\mathrm{S}-F+2,1}+\cdots+t_{N_\mathrm{S},1} \end{matrix}\right\} F \text{ rows} \end{pmatrix}_{N_\mathrm{S}\times 1} . \tag{4.11}$$

By multiplying the backward transmission matrix $\mathbf{T}^T$ (the upper case T stands for matrix transpose) by the conjugated scattered field $\mathbf{E}^{*}_{\mathbf{S,under\text{-}sampled}}$, the optical phase conjugated field $\mathbf{E}_{\mathbf{OPC}}$ exiting the scattering medium can be computed as $\mathbf{E}_{\mathbf{OPC}} = \mathbf{T}^T\mathbf{E}^{*}_{\mathbf{S,under\text{-}sampled}}$. Each element of $\mathbf{E}_{\mathbf{OPC}}$ contains a summation of $F\times N_\mathrm{S}$ terms. Among the elements of $\mathbf{E}_{\mathbf{OPC}}$, only the first element (corresponding to the peak) contains a constructive summation of N_S terms ($t_{11}\times t^{*}_{11}+t_{21}\times t^{*}_{21}+\cdots+t_{N_\mathrm{s}1}\times t^{*}_{N_\mathrm{s}1}$) plus a random summation (random phasor sum) of $(F-1)\times N_\mathrm{S}$ terms, while each of the rest of the elements (corresponding to the background) contains a random summation of $F\times N_\mathrm{S}$ terms. Thus, the theoretical PBR can be estimated by

$$\mathrm{PBR} = \frac{\left|E_{\mathrm{peak}}\right|^2}{\left|E_{\mathrm{background}}\right|^2} = \frac{\left(N_\mathrm{S}\right)^2 + \left(\sqrt{(F-1)\times N_\mathrm{S}}\right)^2}{\left(\sqrt{F\times N_\mathrm{S}}\right)^2} \approx \frac{N_\mathrm{S}}{F} = N_\mathrm{P}. \tag{4.12}$$

We note that the estimated PBR in Eq. (4.12) is exactly the same as the PBR obtained from a rigorous mathematical derivation (see Supplementary notes). The above analysis considers using an SLM that achieves full-field (amplitude plus phase) modulation. When other types of SLMs are employed and when speckle grains are under-sampled, we prove that

$$\mathrm{PBR} = \alpha N_{\mathrm{P}}, \tag{4.13}$$

and $\alpha = \pi/4$, $1/\pi$, and $1/(2\pi)$ for phase-only, binary-phase, and binary-amplitude modulation SLMs, respectively (see Supplementary notes). The analytical results in Eqs. (4.12) and (4.13) are also validated by numerical simulations (see Supplementary notes). We conclude from the above results that, regardless of the wavefront modulation schemes, light focusing through scattering media can still be achieved even when speckle grains are under-sampled. Moreover, since 3×3 pixels to 5×5 pixels were typically used to sample one speckle grain in previous experiments, the PBR achieved by under-sampling is 9 − 25 times higher than the PBR achieved by well-sampling, and in this case all the degrees of freedom of an SLM are fully utilized.

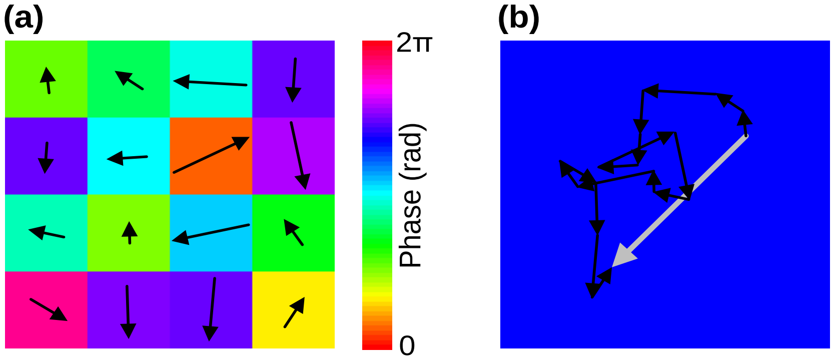

Figure 4.6 Physical meaning of the reconstructed quantity in phase-shifting holography when speckle grains are under-sampled. (a). An illustration of 16 speckle grains occupying one digital PCM pixel. A phasor expression is used to represent the electric field of each speckle grain. (b). The reconstructed quantity (the large gray arrow) is a vector sum of the 16 independent phasors (the small black arrows).

We then performed experiments to investigate time-reversal–based optical focusing through scattering media when speckle grains are under-sampled. The experimental set-up is schematically shown in Fig. 4.7. The output of a continuous-wave laser (Verdi V10, Coherent) was split into a reference beam (R) and a sample beam (S). Then, each beam was modulated by an acousto-optic modulator (AOM), to induce a f_b =12 Hz frequency difference between R and S. After that, R was expanded by a lens pair, while S was scattered by a scattering medium (SM) composed of three ground glass diffusers (DG-120, Thorlabs). An iris was placed before collecting lens L3 to control the speckle size. S was then combined with R by a beamsplitter (BS), and their interference pattern was recorded by a camera (pco.edge 5.5, PCO-Tech) running at a frame rate of $4f_b$. In this way, we measured the wavefront of S using phase-shifting holography. In the playback process, S was blocked by a mechanical shutter (MS), and the conjugation of the measured phase map was displayed on an SLM (Pluto NIR-II, Holoeye, 1920 × 1080 pixels) whose pixels were one-to-one matched with the camera pixels. Upon reflection off the SLM, R was wavefront shaped and was expected to become a collimated beam after passing through the scattering medium SM. To quantify the quality of time reversal, the light exiting the scattering medium was reflected by a 10:90 BS and focused by lens L4 onto another camera (Camera2, pco.edge 5.5, PCO-Tech).

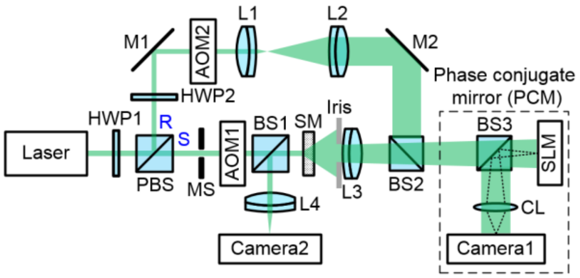

Figure 4.7 Schematic of the experimental setup for time-reversal–based optical focusing through scattering media. AOM, acousto-optic modulator; BS, beamsplitter; CL, camera lens; HWP, half-wave plate; L, lens; M, mirror; MS, mechanical shutter; PBS, polarizing beamsplitter; R, reference beam; S, sample beam; SLM, spatial light modulator; SM, scattering medium.

Two experiments were performed to investigate the effect of sampling speckle grains on the quality of time-reversal–based optical focusing through scattering media. In the first experiment, we varied the pixel size of the PCM through pixel binning (the same binning was performed for both Camera1 and the SLM), while fixing the speckle size on the PCM. Without binning, each speckle grain occupied 3.5×3.5 pixels on average. As the pixel size gradually increased by binning pixels, the sampling of speckle grains changed from well-sampled to under-sampled. Figure 4.8(a) shows the normalized PBR/N_P as a function of the under-sampling factor F. As long as F is no smaller than 1 (speckle grains are under-sampled), PBR/N_P remains close to a constant of 0.117, which is normalized to 1. When F is smaller than 1 (speckle grains are not under-sampled), the normalized PBR/N_P is also smaller than 1, which shows an inefficient utilization of SLM pixels. These experimental results agree with our aforementioned theoretical analysis. In the extreme case when 15×15 pixels are binned to one pixel, corresponding to, on average, 19 speckle grains in one PCM pixel (the far right data point in Fig. 4.8(a)), a bright focus with a PBR ~1100 was achieved [Fig. 4.8(b)]. As a control, when a random phase map was displayed on the SLM, no focus was observed [Fig. 4.8(c)].

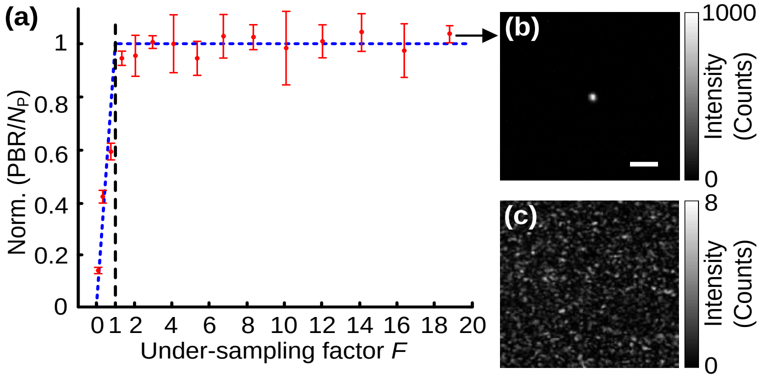

Figure 4.8 Experimental results obtained by varying the pixel size of a PCM while fixing the speckle size on the PCM. a. Plot of normalized PBR/N_P as a function of the under-sampling factor F. The error bars show the standard deviations obtained from three realizations of the scattering medium. The blue dashed line indicates the theoretical

prediction based on Eqs. (4.9) and (4.13). b. Image of the achieved focus captured by Camera2 when the under-sampling factor F was 19. The experimental PBR is ~1100 (theortical PBR is πNP/4/(15×15) ~ 7200). The PBR is ~1100. Scale bar, 200 µm. c. No focus was observed when a random phase map was displayed on the SLM.

In the second experiment, we varied the speckle size on the PCM while fixing the pixel size. Super-pixels binned from 5×5 pixels were used throughout this experiment to measure the under-sampling factor when speckle grains were under-sampled. The speckle size was controlled by varying the aperture size of an iris. Although the number of photons reaching the camera sensor varied as we changed the aperture size of the iris, the SNR during wavefront measurement was always kept well above one. In this case, the PBR will not be affected by the variation in the number of photons reaching the camera (see Fig. 9 of Ref. [36]). When the iris was fully opened, a speckle grain occupied ~0.48 super-pixel on average, so it was under-sampled. By gradually closing the iris, the speckle size increased accordingly and finally surpassed the super-pixel size. Figure 4.9 shows the measured PBR of the focus (normalized by 9100) as a function of the speckle area. When the speckle area is smaller than the super-pixel area (speckle grains are under-sampled), the PBRs are around a constant value of 9100. This observation is consistent with Eq. (4.13), because the PBR is theoretically determined only by the fixed pixel count and is independent of the under-sampling factor. When the speckle area surpasses the super-pixel area (speckle grains are well-sampled), the PBR is inversely proportional to the speckle area. This observation indicates that the PBR is proportional to N_S, which agrees with Eq. (4.9). Having checked all the PBRs obtained with different speckle areas, we note that higher PBRs were achieved when speckle areas were smaller than the super-pixel area, corresponding to under-sampling speckle grains. Compared with the PBR achieved by using 4.2 × 4.2 super-pixels to well-sample speckle grains, the PBR was improved by 16 times with under-sampling speckle-grains. When the speckle area was 0.48× the super-pixel area (the far left data point in Fig.

4.9(a)), a bright focus with a PBR of 9100 was achieved [Fig. 4.9(b)]. As a control, when a random phase map was displayed on the SLM, no focus was observed [Fig. 4.9(c)]. Using focused-ultrasound–guided digital optical phase conjugation (TRUE focusing), we focused light inside a scattering medium comprising two diffusers. Again, the PBR of the focus is higher with under-sampling compared with well-sampling (see Supplementary notes).

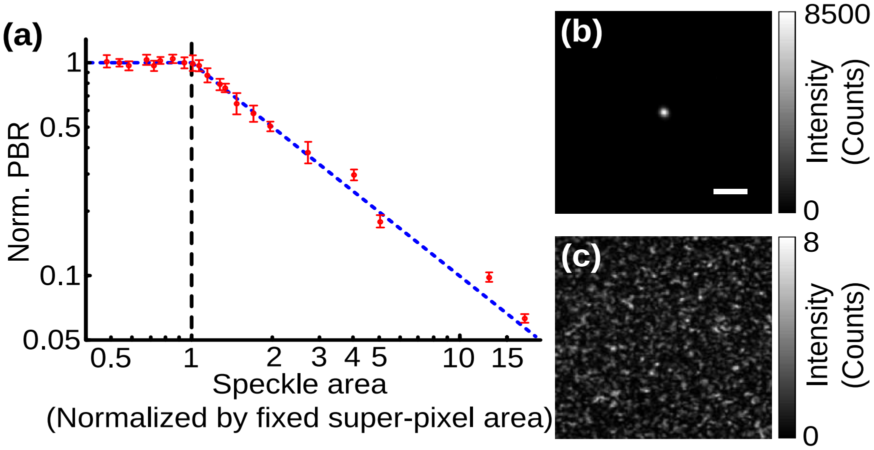

Figure 4.9 Experimental results obtained by varying the speckle size on a PCM while fixing the pixel size. (a). Plot of normalized PBR as a function of speckle area. The horizontal and vertical axes are shown in the log scale. The blue dashed line indicates the theoretical prediction based on Eqs. (4.9) and (4.13). The error bars show the standard deviations obtained from three realizations of the scattering medium. (b). Image of the achieved focus when the speckle area was 0.48× the pixel area. The PBR is 9100. Scale bar, 200 µm. c. No focus was observed when a random phase map was displayed on the SLM.

Here, we improved the focusing quality by pushing the upper limit of theoretical PBR to N_P. Although great efforts have been made [96, 106], experimentally achieved PBRs were always lower than their theoretical values, due to misalignment of the system (including imperfect matching between the pixels of the camera and the pixels of the SLM, non-uniformity of the reference beam, imperfect perpendicularity between the reference beam and the SLM, etc.) and the surface curvature of the SLM. In our experiments, when speckle grains were under-sampled and N_P was 83000 (5×5 binning), the achieved PBR was 9100, which is still seven times lower than its theoretical value ($\pi N_P/4 \sim 65000$).

Besides improving the PBR, under-sampling speckle grains also improves the SNR of wavefront measurement. When speckle grains are under-sampled and the main noise source is shot noise, it is proved in Supplementary notes that the SNR of wavefront measurement is given by

$$\mathrm{SNR}_{\textbf{under-sampled}} = 2\sqrt{\mathrm{NPS}}, \tag{4.14}$$

where NPS is the average number of photoelectrons induced by the light exiting the sample per speckle grain. On the other hand, when speckle grains are well-sampled, it has been proved that the SNR is given by [75]

$$\mathrm{SNR}_{\textbf{well-sampled}} = 2\sqrt{\mathrm{NPP}} = 2\sqrt{\mathrm{NPS}/G}. \tag{4.15}$$

Here, NPP is the average number of photoelectrons induced by the light exiting the sample per camera pixel, and $G = 1/F$ describes the average number of pixels used to sample one speckle grain, which is larger than 1. When an iris is used to control the speckle size [Fig. 4.5(e)], both the light power and the total number of speckle grains intercepted by the PCM are proportional to the area of the iris aperture, so NPS is a constant, independent of the speckle size. Thus, from Eqs. (4.14) and (4.15), we conclude that under-sampling speckle grains increase the SNR of wavefront measurement by a factor of $\sqrt{G}$, compared with well-sampling speckle grains. Considering that 3×3 pixels to 5×5 pixels have usually been used to sample one speckle grain in previous experiments, the SNR can be enhanced by 3 – 5 times with under-sampling speckle grains.

4.2.3 Discussion and Conclusion

It was proved theoretically that feedback-based and time-reversal–based wavefront shaping find the same optimum wavefront [110]. However, before our work, the experimentally determined wavefronts by these two approaches were not the same. Since speckle grains were well-sampled, neighboring pixels were correlated in previous time-reversal–based wavefront shaping, while neighboring (super) pixels were uncorrelated in feedback-based wavefront shaping [15]. Under-sampling speckle grains in time-reversal–based wavefront shaping bridges this gap between theoretical prediction and experimental observation, since neighboring pixels are not correlated any longer.

Moreover, we note that when a scattering medium is thick, polarization can be completely scrambled by scattering. By using a vector transmission matrix in the derivation [34, 100], it is straightforward to see that all the conclusions we obtained in this work are still valid, except that all the PBRs are reduced by half. Such a PBR reduction can be understood by considering the enhanced background due to the field along a polarization direction orthogonal to the incident polarization direction.

In acoustic time-reversal, Fink *et al.* stated that “the transducers can be spaced as far apart as half the smallest wavelength without impairing the quality of the reproduction” [111, 112], suggesting that well-sampling is preferred in acoustic time-reversal. Even though the pitch of a transducer array is two or three times larger than half the acoustic wavelength in some experiments [113, 114], it was unclear whether the ultrasonic wavefront was under-sampled in these experiments, since the ultrasonic wave exiting a scattering medium propagated some distance before reaching the array and the ultrasonic coherence area at the array location was not reported. Fink *et al.* later realized that “the best situation would be one in which all array elements receive totally independent information" [115], however, he also stated that "this is not physically possible" [115]. Regardless, to the best of our knowledge, this paper is the first to point out and demonstrate that under-sampling the wavefront is better than well-sampling in optical time-reversal experiments.

In summary, we theoretically and experimentally demonstrate that even when speckle grains are under-sampled, light can still be focused through or inside opaque scattering media. In fact, we proved that sub-Nyquist sampling can boost the PBR by more than ten times than conventional well-sampling conditions and also increase the SNR of wavefront measurement. Moreover, since our method does not require magnification of speckle grains, we remove the need to use an iris or objective lenses in the set-up and are able to place the PCM closer to the sample, thus greatly improving the collection efficiency of the scattered light. We anticipate that our discovery will transform the understanding of optical time-reversal and boost the performance of light focusing through opaque media for optical imaging, manipulation, therapy and communication.

4.2.4 Supplementary notes

The physical meaning of the reconstructed quantity in phase-shifting holography when speckle grains are under-sampled

Phase-shifting holography has been widely used to measure the phase of scattered light. However, in all previous experiments, the speckle grains were well-sampled by camera pixels. When speckle grains are under-sampled, it is still unclear what quantity is measured by phase-shifting holography and whether optical focusing through optical phase conjugation can still be achieved. We investigate this problem here. In one implementation of phase-shifting holography [31, 74, 109], a planar reference beam and a sample beam with a distorted wavefront beat at a frequency of f_b, and a digital camera records their interference pattern at a frame rate of $4f_\mathrm{b}$. Four successive frames are used to reconstruct the phase and amplitude of the sample beam. When speckle grains are under-sampled, the light power on a single pixel of the camera in each frame can be written as

$$P_k = AE_\mathrm{R}^2 + \frac{A}{F}\sum_{j=1}^{F} E_\mathrm{S}^2\left(\vec{r}_j\right) + \frac{A}{F}\sum_{j=1}^{F} 2E_\mathrm{R}E_\mathrm{S}\left(\vec{r}_j\right)\cos\left[\phi_\mathrm{S}\left(\vec{r}_j\right) + \left(k-1\right)\pi/2\right],\ k = 1,2,3,4. \tag{S4.1}$$

Here, A is the area of one pixel; F is the number of speckle grains within one pixel, which corresponds to the under-sampling factor in the main text; E_R is the amplitude of the reference beam, and we assume that the phase of the reference beam is 0 for simplicity; and $E_\mathrm{S}\left(\vec{r}_j\right)$ and $\phi_\mathrm{S}\left(\vec{r}_j\right)$ are the amplitude and phase of the electric field (along the polarization direction of the reference beam) of the j-th speckle grain located at $\vec{r}_j$ within one pixel. Each speckle grain is assumed to have the same size. Since the camera samples the beat at 4× the beat frequency, the interference term in each successive frame has a $\pi/2$ phase shift, which is reflected in the cosine term. Based on Eq. (S4.1), the reconstructed quantity in phase-shifting holography can be found by

$$E \equiv \left(P_1 - P_3\right) + i\left(P_4 - P_2\right) = \frac{4E_\mathrm{R}A}{F}\sum_{j=1}^{F} E_\mathrm{S}\left(\vec{r}_j\right)e^{i\phi_\mathrm{S}\left(\vec{r}_j\right)} = C \times \sum_{j=1}^{F} E_\mathrm{S}(\vec{r}_j)e^{i\phi_\mathrm{S}\left(\vec{r}_j\right)}, \tag{S4.2}$$

where C is a constant prefactor. From Eq. (S4.2), we conclude that when speckle grains are under-sampled, the reconstructed quantity on each pixel in phase-shifting holography is proportional to the summation of the electric fields of all the speckle grains within that pixel.

Derivation of peak-to-background ratios of optical time reversal under different speckle sampling conditions

Here, we provide an analytical analysis of theoretical peak-to-background ratios (PBRs) of time-reversal–based wavefront shaping when speckle grains are well-sampled and under-sampled. For simplicity without losing generality, the incident field $\mathbf{E_{in}}$ is set to be 1 for the first element and 0 for the rest of the elements. The total number of elements in the incident field is N_I. To model the scattering process, a transmission matrix $\mathbf{T}$ that connects the incident field $\mathbf{E_{in}}$ and the scattered field $\mathbf{E_S}$ is introduced. The matrix elements t_{ij} satisfy a circular Gaussian distribution. That is to say, the real part (x) and the imaginary part (y) of each element are independent variables, and they satisfy the Gaussian distribution $f_x\left(\mu=0,\sigma\right)=e^{-x^2/\left(2\sigma^2\right)}\Big/\sqrt{2\pi\sigma^2}$, $f_y\left(\mu=0,\sigma\right)=e^{-y^2/\left(2\sigma^2\right)}\Big/\sqrt{2\pi\sigma^2}$, with a mean of zero and a standard deviation of σ . The dimensions of the matrix are set to be $N_\mathrm{S}\times N_\mathrm{I}$, with $N_\mathrm{S} < N_\mathrm{I}$. The scattered field $\mathbf{E_S}$ intercepted by the phase conjugation mirror (PCM) can be computed as follows:

$$\mathbf{E_S}=\mathbf{TE_{in}}=\begin{pmatrix} t_{11} & t_{12} & \cdots & t_{1N_\mathrm{I}} \\ t_{21} & t_{22} & \cdots & t_{2N_\mathrm{I}} \\ \vdots & \vdots & \ddots & \vdots \\ t_{N_\mathrm{S}1} & t_{N_\mathrm{S}2} & \ldots & t_{N_\mathrm{S}N_\mathrm{I}} \end{pmatrix}_{N_\mathrm{S}\times N_\mathrm{I}} \begin{pmatrix} 1 \\ 0 \\ \vdots \\ 0 \end{pmatrix}_{N_\mathrm{I}\times 1} = \begin{pmatrix} t_{11} \\ t_{21} \\ \vdots \\ t_{N_\mathrm{S}1} \end{pmatrix}_{N_\mathrm{S}\times 1} . \qquad \text{(S4.3)}$$

We note that each element in $\mathbf{E_S}$ describes the electric field of an independent speckle grain, and the total number of speckle grains on the PCM is N_S.

a. When speckle grains are well-sampled

We start by describing the wavefront measurement and wavefront reconstruction in the well-sampling situation, because similar mathematics will be adopted in the description of the under-sampling situation. When speckle grains are well-sampled, so that one speckle grain occupies multiple pixels, the experimentally measureable scattered field $\mathbf{E}_{\mathbf{S,well\text{-}sampled}}$ is identical to $\mathbf{E}_{\mathbf{S}}$:

$$\mathbf{E}_{\mathbf{S,well\text{-}sampled}} = \begin{pmatrix} t_{11} \\ t_{21} \\ \vdots \\ t_{N_\mathrm{S}1} \end{pmatrix}_{N_\mathrm{S}\times 1} . \tag{S4.4}$$

By multiplying the backward transmission matrix $\mathbf{T}^{T}$ (the upper case T stands for matrix transpose) by the conjugated scattered field $\mathbf{E}^{*}_{\mathbf{S,well\text{-}sampled}}$, the optical phase conjugated field $\mathbf{E}_{\mathbf{OPC}}$ exiting the scattering medium can be computed as

$$\mathbf{E}_{\mathbf{OPC}} = \begin{pmatrix} t_{11} & t_{21} & \cdots & t_{N_\mathrm{S}1} \\ t_{12} & t_{22} & \cdots & t_{N_\mathrm{S}2} \\ \vdots & \vdots & \ddots & \vdots \\ t_{1N_\mathrm{I}} & t_{2N_\mathrm{I}} & \ldots & t_{N_\mathrm{S}N_\mathrm{I}} \end{pmatrix}_{N_\mathrm{I}\times N_\mathrm{S}} \begin{pmatrix} t^{*}_{11} \\ t^{*}_{21} \\ \vdots \\ t^{*}_{N_\mathrm{S}1} \end{pmatrix}_{N_\mathrm{S}\times 1} . \tag{S4.5}$$

The first element of $\mathbf{E}_{\mathbf{OPC}}$ corresponds to the electric field of the peak of the focus, and is calculated by

$$E_{\mathrm{peak}} = \sum_{m=1}^{N_\mathrm{S}} t_{m1} t^{*}_{m1} = \sum_{m=1}^{N_\mathrm{S}} \left| t_{m1} \right|^{2}, \tag{S4.6}$$

By taking the absolute square of the electric field and then performing an ensemble average $\langle \bullet \rangle$, the peak intensity of the focus is

$$\begin{aligned} I_{\text{peak}} &= \left\langle \left| E_{\text{peak}} \right|^2 \right\rangle, \\ &= \left| N_{\text{S}} \int_{-\infty}^{+\infty} \int_{-\infty}^{+\infty} dxdy \left(x^2 + y^2 \right) f_x\left(0,\sigma\right) f_y\left(0,\sigma\right) \right|^2, \\ &= \left| N_{\text{S}} \int_{0}^{2\pi} \int_{-\infty}^{+\infty} drd\theta r^3 \frac{1}{2\pi\sigma^2} e^{-r^2 / 2\sigma^2} \right|^2, \\ &= \left| N_{\text{S}} 2\sigma^2 \Gamma(2) \right|^2 = 4\sigma^4 N_{\text{S}}^2, \end{aligned} \tag{S4.7}$$

Here, the discrete summation is approximated by a continuous integration when N_{S} is large; $x+iy$ and $r\exp(i\theta)$ are the expressions of t_{m1} in Cartesian and polar coordinates, respectively; and $\Gamma\left(x\right) = \int_{0}^{+\infty} t^{x-1} e^{-t} dt$ is the gamma function. The rest of the elements of $\mathbf{E}_{\mathbf{OPC}}$ correspond to the fields of the background, and can be calculated as follows, based on Eq. (S4.5):

$$E_{\text{background}} = \sum_{m=1}^{N_{\text{S}}} t_{mn} t_{m1}^{*},\ n \neq 1. \tag{S4.8}$$

Thus, the background intensity is calculated by

$$I_{\text{background}} = \left\langle \left| E_{\text{background}} \right|^2 \right\rangle = \left\langle \left| \sum_{m=1}^{N_{\text{S}}} t_{mn} t_{m1}^{*} \right|^2 \right\rangle, n \neq 1. \tag{S4.9}$$

To proceed, we define

$$\begin{aligned} V_m &\equiv t_{mn} t_{m1}^{*},\ n \neq 1, \\ U &\equiv \sum_{m=1}^{N_{\text{S}}} V_m, \end{aligned} \tag{S4.10}$$

where both V_m and U have zero mean. Then, Eq. (S4.9) can be rewritten as

$$I_{\text{background}} = \left\langle \left| U \right|^2 \right\rangle = \text{Var}\left(U\right), \tag{S4.11}$$

where $\mathrm{Var}(\bullet) \equiv \mathrm{Var}^{\mathrm{real}}(\bullet) + \mathrm{Var}^{\mathrm{imag}}(\bullet)$ expresses the summation of the variance for both the real part and the imaginary part of a complex random variable. From the central limit theorem, the variance of U is N_S times the variance of V_m, so we have

$$I_{\mathrm{background}} = \mathrm{Var}(U) = N_\mathrm{S}\,\mathrm{Var}(V_m) = N_\mathrm{S}\,\mathrm{Var}\left(t_{mn}t_{m1}^{*}\right). \tag{S4.12}$$

Since t_{mn} and t_{m1}^{*} are independent complex random variables with mean values of zero, it can be shown that the variance of their product equals the product of their variances. Thus, we have

$$\begin{aligned} I_{\mathrm{background}} &= N_\mathrm{S}\,\mathrm{Var}\left(t_{mn}t_{m1}^{*}\right), \\ &= N_\mathrm{S}\,\mathrm{Var}\left(t_{mn}\right)\mathrm{Var}\left(t_{m1}^{*}\right), \\ &= N_\mathrm{S} \times 2\sigma^2 \times 2\sigma^2 = 4\sigma^4 N_\mathrm{S}. \end{aligned} \tag{S4.13}$$

From the results in Eq. (S4.7) and Eq. (S4.13), the theoretical peak-to-background ratio (PBR) is

$$\mathrm{PBR} = I_{\mathrm{peak}} / I_{\mathrm{background}} = N_\mathrm{S}. \tag{S4.14}$$

The same result when speckle grains are well-sampled has also been reported [30, 57]. Eq. (S4.14) shows that when speckle grains are well-sampled, the theoretical PBR of the focus is determined by the number of speckle grains intercepted by the PCM. Since 3×3 pixels to 5×5 pixels were typically used to sample one speckle grain in previous experiments, N_S is usually 9 − 25 times smaller than the number of pixels (N_P) of a spatial light modulator (SLM).

b. When speckle grains are under-sampled

Now, we investigate the situation when speckle grains are under-sampled with under-sampling factor $F \equiv N_\mathrm{S}/N_\mathrm{P}$. In this case, multiple speckle grains are within one PCM pixel. With the knowledge that phase-shifting holography reconstructs the summation of the electric fields of all the speckle grains within one pixel, the experimentally measurable scattered field $\mathbf{E}_{\mathbf{S,undersampled}}$ has the following form:

$$\mathbf{E}_{\mathbf{S,undersampled}} = \begin{pmatrix} \left.\begin{matrix} t_{11}+t_{21}+\cdots+t_{F1} \\ t_{11}+t_{21}+\cdots+t_{F1} \\ \vdots \\ t_{11}+t_{21}+\cdots+t_{F1} \end{matrix}\right\} F \text{ rows} \\ \vdots \\ \left.\begin{matrix} t_{N_S-F+1,1}+t_{N_S-F+2,1}+\cdots+t_{N_S,1} \\ t_{N_S-F+1,1}+t_{N_S-F+2,1}+\cdots+t_{N_S,1} \\ \vdots \\ t_{N_S-F+1,1}+t_{N_S-F+2,1}+\cdots+t_{N_S,1} \end{matrix}\right\} F \text{ rows} \end{pmatrix}_{N_S\times 1} . \qquad \text{(S4.15)}$$

By multiplying the backward transmission matrix $\mathbf{T}^T$ by the conjugated scattered field $\mathbf{E}^*_{\mathbf{S,undersampled}}$, the optical phase conjugated field $\mathbf{E}_{\mathbf{OPC}}$ exiting the scattering medium is computed as

$$\mathbf{E}_{\mathbf{OPC}} = \mathbf{T}^T\mathbf{E}_{\mathbf{P}} = \begin{pmatrix} t_{11} & t_{21} & \cdots & t_{N_S 1} \\ t_{12} & t_{22} & \cdots & t_{N_S 2} \\ \vdots & \vdots & \ddots & \vdots \\ t_{1N_I} & t_{2N_I} & \ldots & t_{N_S N_I} \end{pmatrix}_{N_I\times N_S} \begin{pmatrix} \left.\begin{matrix} t^*_{11}+t^*_{21}+\cdots+t^*_{F1} \\ t^*_{11}+t^*_{21}+\cdots+t^*_{F1} \\ \vdots \\ t^*_{11}+t^*_{21}+\cdots+t^*_{F1} \end{matrix}\right\} F \text{ rows} \\ \vdots \\ \left.\begin{matrix} t^*_{N_S-F+1,1}+t^*_{N_S-F+2,1}+\cdots+t^*_{N_S,1} \\ t^*_{N_S-F+1,1}+t^*_{N_S-F+2,1}+\cdots+t^*_{N_S,1} \\ \vdots \\ t^*_{N_S-F+1,1}+t^*_{N_S-F+2,1}+\cdots+t^*_{N_S,1} \end{matrix}\right\} F \text{ rows} \end{pmatrix}_{N_S\times 1} . \qquad \text{(S4.16)}$$

To simplify the mathematical calculation, we introduce a new set of variables b_{ij} ($i = 1, 2, \ldots, N_P$, $j = 1, 2, \ldots, N_I$):

$$\begin{aligned} b_{1,j} &= t_{1,j} + t_{2,j} + \cdots + t_{F,j}, \\ b_{2,j} &= t_{F+1,j} + t_{F+2,j} + \cdots + t_{2F,j}, \\ &\ \vdots \\ b_{N_\mathrm{P},j} &= t_{N_\mathrm{S}-F+1,j} + t_{N_\mathrm{S}-F+2,j} + \cdots + t_{N_\mathrm{S},j}. \end{aligned} \tag{S4.17}$$

Since t_{ij} satisfies a circular Gaussian distribution, b_{ij} automatically satisfies another circular Gaussian distribution. Using the above transformations, Eq. (S4.16) can be re-formulated as

$$\mathbf{E_{OPC}} = \begin{pmatrix} b_{11} & b_{21} & \cdots & b_{N_\mathrm{P}1} \\ b_{12} & b_{22} & \cdots & b_{N_\mathrm{P}2} \\ \vdots & \vdots & \ddots & \vdots \\ b_{1N_\mathrm{I}} & b_{2N_\mathrm{I}} & \ldots & b_{N_\mathrm{P}N_\mathrm{I}} \end{pmatrix}_{N_\mathrm{I}\times N_\mathrm{P}} \begin{pmatrix} b_{11}^* \\ b_{21}^* \\ \vdots \\ b_{N_\mathrm{P}1}^* \end{pmatrix}_{N_\mathrm{P}\times 1} . \tag{S4.18}$$

We note that Eq. (S4.18) shares the same mathematical form as Eq. (S4.5), except that N_S becomes N_P. Hence, following the same procedures described for Eqs. (S4.6) – (S4.14), the theoretical PBR when speckle grains are under-sampled can be found by

$$\mathrm{PBR} = N_\mathrm{P}. \tag{S4.19}$$

Eq. (S4.19) shows that when speckle grains are under-sampled, the theoretical PBR equals the number of SLM pixels, which is usually 9 − 25 times higher than the theoretical PBR achieved when speckle grains are well-sampled.

Derivation of peak-to-background ratios of optical time reversal using different wavefront modulation schemes when speckle grains are under-sampled

To achieve a large pixel count or a fast modulation speed, many types of SLMs do not support full-field (amplitude plus phase) electric field modulation. For example, nematic liquid crystal based SLMs provide phase-only modulation, ferroelectric liquid crystal based SLMs provide binary-phase modulation, and digital micromirror devices provide binary-amplitude modulation. Thus, it is important to investigate the performance of time-reversal–based wavefront shaping under various modulation schemes, especially when speckle grains are under-sampled. Here, we start by describing various modulation schemes in the well-sampled condition. We note that when speckle grains are well-sampled, the PBRs under different wavefront modulation schemes were reported in the literature [30, 57, 91, 93].

a. When speckle grains are well-sampled

a1 Phase-only modulation

Based on Eq. (S4.4), when only the phase of the electric field is modulated, the conjugated scattered field is

$$\mathbf{E}^{*}_{\text{S,well-sampled,phase-only}} = \begin{pmatrix} t^{*}_{11}/|t_{11}| \\ t^{*}_{21}/|t_{21}| \\ \vdots \\ t^{*}_{N_\text{S}1}/|t_{N_\text{S}1}| \end{pmatrix}_{N_\text{S}\times 1}. \tag{S4.20}$$

Thus, the optical phase conjugated field $\mathbf{E}_{\mathbf{OPC}}$ exiting the scattering medium can be obtained by multiplying the backward transmission matrix $\mathbf{T}^{T}$ by $\mathbf{E}^{*}_{\text{S,well-sampled,phase-only}}$. Specifically, the first element, which corresponds to the electric field of the peak of the focus, is computed as

$$E_{\text{peak}} = \sum_{m=1}^{N_\text{S}} t_{m1} \frac{t^{*}_{m1}}{|t_{m1}|} = \sum_{m=1}^{N_\text{S}} |t_{m1}|. \tag{S4.21}$$

Thus, the peak intensity of the focus is computed by

$$\begin{aligned} I_{\text{peak}} &= \left\langle \left| E_{\text{peak}} \right|^2 \right\rangle \\ &= \left| N_{\text{S}} \int_{-\infty}^{+\infty} \int_{-\infty}^{+\infty} dxdy \left| x + iy \right| f_x\left(0, \sigma\right) f_y\left(0, \sigma\right) \right|^2, \\ &= \left| N_{\text{S}} \int_0^{2\pi} \int_0^{+\infty} drd\theta \frac{r^2}{2\pi\sigma^2} e^{-r^2 / 2\sigma^2} \right|^2, \\ &= \left| N_{\text{S}} \sqrt{2}\sigma\Gamma\left(\frac{3}{2}\right) \right|^2 = \frac{1}{2}\sigma^2 \pi N_{\text{S}}^2. \end{aligned} \tag{S4.22}$$

The remaining elements of $\mathbf{E_{OPC}}$ correspond to the fields of the background, and can be calculated as

$$E_{\text{background}} = \sum_{m=1}^{N_{\text{S}}} t_{mn} \frac{t_{m1}^*}{\left| t_{m1} \right|}, n \neq 1. \tag{S4.23}$$

Thus, the background intensity is expressed as

$$I_{\text{background}} = \left\langle \left| \sum_{m=1}^{N_{\text{S}}} t_{mn} \frac{t_{m1}^*}{\left| t_{m1} \right|} \right|^2 \right\rangle, n \neq 1, \tag{S4.24}$$

which can be computed by following the same procedures as for Eqs. (S4.9) – (S4.12):

$$\begin{aligned} I_{\text{background}} &= N_{\text{S}} \text{Var}\left(t_{mn} \frac{t_{m1}^*}{\left| t_{m1} \right|} \right), \\ &= N_{\text{S}} \text{Var}\left(t_{mn}\right) \text{Var}\left(\frac{t_{m1}^*}{\left| t_{m1} \right|} \right), \\ &= N_{\text{S}} \times 2\sigma^2 \times 1 = 2\sigma^2 N_{\text{S}}. \end{aligned} \tag{S4.25}$$

From the results in Eq. (S4.22) and Eq. (S4.25), the theoretical PBR for phase-only modulation is

$$\text{PBR} = I_{\text{peak}} / I_{\text{background}} = \frac{\pi}{4} N_{\text{S}}. \qquad \text{(Phase-only modulation)} \tag{S4.26}$$

a2 Binary-phase modulation

When an SLM provides binary-phase modulation, the conjugated scattered field is

$$\mathbf{E}^{*}_{\text{S,well-sampled, binary phase}} = \begin{pmatrix} BP\left(t_{11}\right) \\ BP\left(t_{21}\right) \\ \vdots \\ BP\left(t_{N_{\mathrm{S}}1}\right) \end{pmatrix}_{N_{\mathrm{S}}\times 1}, \tag{S4.27}$$

In the above equation, the binary-phase operator $BP\left(z = x + iy\right)$ is defined as

$$BP\left(z\right) = \begin{cases} 1, & \text{if } y > 0, \\ -1, & \text{if } y < 0. \end{cases} \tag{S4.28}$$

By multiplying the backward transmission matrix by $\mathbf{E}^{*}_{\text{S,well-sampled, binary phase}}$, the optical phase conjugated field $\mathbf{E}_{\mathbf{OPC}}$ exiting the scattering medium can be obtained. Again, the first element of $\mathbf{E}_{\mathbf{OPC}}$ corresponds to the electric field of the peak of the focus, and it can be calculated as

$$E_{\text{peak}} = \sum_{m=1}^{N_{\mathrm{S}}} t_{m1} BP\left(t_{m1}\right), \tag{S4.29}$$

Thus, the peak intensity of the focus is

$$\begin{aligned} I_{\text{peak}} &= \left\langle \left| E_{\text{peak}} \right|^{2} \right\rangle \\ &= \left| N_{\mathrm{S}} \int_{-\infty}^{+\infty} \int_{-\infty}^{+\infty} dxdy \left(x + iy\right) \left[\theta\left(y\right) - \theta\left(-y\right)\right] f_{x}\left(0,\sigma\right) f_{y}\left(0,\sigma\right) \right|^{2}, \\ &= \left| iN_{\mathrm{S}} \int_{-\infty}^{+\infty} \int_{-\infty}^{+\infty} dxdy \left(y\theta\left(y\right) - y\theta\left(-y\right)\right) f_{x}\left(0,\sigma\right) f_{y}\left(0,\sigma\right) \right|^{2}, \\ &= \left| 2iN_{\mathrm{S}} \int_{0}^{+\infty} dy y f_{y}\left(0,\sigma\right) \right|^{2}, \\ &= \left| \frac{2iN_{\mathrm{S}}\sigma}{\sqrt{2\pi}} \Gamma\left(1\right) \right|^{2} = \frac{2}{\pi} \sigma^{2} N_{\mathrm{S}}^{2}, \end{aligned} \tag{S4.30}$$

where $\theta\left(\bullet\right)$ is the Heaviside step function. The remaining elements of $\mathbf{E}_{\mathbf{OPC}}$ correspond to the fields of the background, and can be calculated as

$$E_{\text{background}} = \sum_{m=1}^{N_{\text{S}}} t_{mn} BP\left(t_{m1}\right),\ n \neq 1 \tag{S4.31}$$

Thus, the background intensity is expressed as

$$I_{\text{background}} = \left\langle \left| \sum_{m=1}^{N_{\text{S}}} t_{mn} BP\left(t_{m1}\right) \right|^2 \right\rangle, n \neq 1, \tag{S4.32}$$

which can be computed by following the same procedures as for Eqs. (S4.9) – (S4.12):

$$\begin{aligned} I_{\text{background}} &= N_{\text{S}} \text{Var}\left(t_{mn} BP(t_{m1})\right), \\ &= N_{\text{S}} \text{Var}(t_{mn}) \text{Var}\left(BP(t_{m1})\right), \\ &= N_{\text{S}} \times 2\sigma^2 \times 1 = 2\sigma^2 N_{\text{S}}. \end{aligned} \tag{S4.33}$$

From the results in Eq. (S4.30) and Eq. (S4.33), the theoretical PBR for binary-phase modulation is

$$\text{PBR} = I_{\text{peak}} \big/ I_{\text{background}} = \frac{1}{\pi} N_{\text{S}}. \qquad \text{(Binary-phase modulation)} \tag{S4.34}$$

a3 Binary-amplitude modulation

When an SLM provides binary-amplitude modulation, the conjugated scattered field is

$$\mathbf{E}^*_{\textbf{S,well-sampled, binary amplitude}} = \begin{pmatrix} BA\left(t_{11}\right) \\ BA\left(t_{21}\right) \\ \vdots \\ BA\left(t_{N_{\text{S}}1}\right) \end{pmatrix}_{N_{\text{S}} \times 1}, \tag{S4.35}$$

where the binary-amplitude operator $BA\left(z = x + iy\right)$ is defined as

$$BA(z) = \begin{cases} 1, & \text{if } y > 0, \\ 0, & \text{if } y < 0. \end{cases} \tag{S4.36}$$

By multiplying the backward scattering matrix $\mathbf{T}^T$ by $\mathbf{E}^*_{\mathbf{S,well\text{-}sampled,binary\,amplitude}}$, the optical phase conjugated field $\mathbf{E_{OPC}}$ exiting the scattering medium can be obtained. The electric field of the peak of the focus corresponds to the first element of $\mathbf{E_{OPC}}$, and can be calculated as

$$E_{\mathrm{peak}} = \sum_{m=1}^{N_{\mathrm{S}}} t_{m1} BA(t_{m1}). \tag{S4.37}$$

Thus, the peak intensity can be calculated as

$$\begin{aligned} I_{\mathrm{peak}} &= \left\langle \left| E_{\mathrm{peak}} \right|^2 \right\rangle \\ &= \left| N_{\mathrm{S}} \int_{-\infty}^{+\infty} \int_{-\infty}^{+\infty} dxdy \left(x + iy\right) \theta\left(y\right) f_x\left(0,\sigma\right) f_y\left(0,\sigma\right) \right|^2, \\ &= \left| iN_{\mathrm{S}} \int_{-\infty}^{+\infty} \int_{-\infty}^{+\infty} dxdyy\theta\left(y\right) f_x\left(0,\sigma\right) f_y\left(0,\sigma\right) \right|^2, \\ &= \left| iN_{\mathrm{S}} \int_{0}^{+\infty} dyyf_y\left(0,\sigma\right) \right|^2, \\ &= \left| \frac{iN_{\mathrm{S}}\sigma}{\sqrt{2\pi}} \Gamma\left(1\right) \right|^2 = \frac{N_{\mathrm{S}}^2 \sigma^2}{2\pi}. \end{aligned} \tag{S4.38}$$

The remaining elements of $\mathbf{E_{OPC}}$ correspond to the fields of the background, and can be calculated as

$$E_{\mathrm{background}} = \sum_{m=1}^{N_{\mathrm{S}}} t_{mn} BA(t_{m1}), n \neq 1. \tag{S4.39}$$

Thus, the background intensity is expressed as

$$I_{\mathrm{background}} = \left\langle \left| \sum_{m=1}^{N_{\mathrm{S}}} t_{mn} BA(t_{m1}) \right|^2 \right\rangle, n \neq 1, \tag{S4.40}$$

which can be computed by following the same procedures as for Eqs. (S4.9) – (S4.12):

$$\begin{aligned} I_{\text{background}} &= N_{\text{S}}\operatorname{Var}\left(t_{mn}BA(t_{m1})\right), \\ &= N_{\text{S}}\frac{1}{2}\operatorname{Var}(t_{mn}), \\ &= N_{\text{S}} \times 2\sigma^2 \times \frac{1}{2} = \sigma^2 N_{\text{S}}. \end{aligned} \tag{S4.41}$$

From the results in Eq. (S4.38) and Eq. (S4.41), the theoretical PBR for binary-amplitude modulation is

$$\text{PBR} = I_{\text{peak}} \big/ I_{\text{background}} = \frac{1}{2\pi} N_{\text{S}}. \qquad \text{(Binary-amplitude modulation)} \tag{S4.42}$$

We note that when speckle grains are well-sampled, same results for the PBRs under different wavefront modulation schemes were also reported [91].

b. When speckle grains are under-sampled

Using the transformations in Eq. (S4.17) and following the same procedures for Eqs. (S4.20) – (S4.42), when multiple speckle grains are within one pixel, the theoretical PBRs can be derived as

$$\begin{aligned} \text{PBR}_{\textbf{under-sampled}} &= \frac{\pi}{4} N_{\text{P}}, && \text{(phase-only modulation)} \\ \text{PBR}_{\textbf{under-sampled}} &= \frac{1}{\pi} N_{\text{P}}, && \text{(binary-phase modulation)} \\ \text{PBR}_{\textbf{under-sampled}} &= \frac{1}{2\pi} N_{\text{P}}. && \text{(binary-amplitude modulation)} \end{aligned} \tag{S4.43}$$

Numerical simulations of peak-to-background ratios of optical time reversal using various wavefront modulation schemes when speckle grains are under-sampled

To verify the analytical results in Eqs. (S4.19) and (S4.43), we performed numerical simulation based on random matrix theory. In the simulation, the pixel count of the PCM was fixed to be 100, while the under-sampling factor F, which is the number of speckle grains within one pixel, was varied from 1 to 100 ($F = N_S/N_P$). Figure 4.10 shows the simulated PBR/N_P as a function of F for different wavefront modulation schemes. We observe that PBR/N_P remains close to a constant value independent of F, and the constant values are close to their theoretical values of 1, $\pi/4$, $1/\pi$, and $1/(2\pi)$, for full-field, phase-only, binary-phase, and binary-amplitude modulation, respectively.

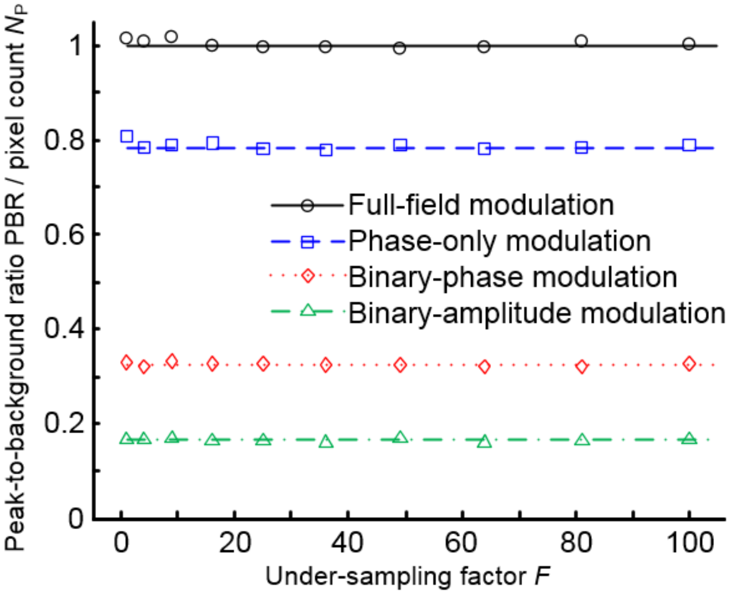

Figure 4.10 Numerical simulation of peak-to-background ratios (PBRs) when speckle grains are under-sampled with different factors F ($1 \leq F \leq 100$). The black circles, blue squares, red diamonds, and green triangles denote PBR/N_P for full-field, phase-only, binary-phase, and binary-amplitude modulation, respectively. Each data point was obtained by averaging 200 independent simulation results. Error bars are not plotted due to their indiscernible lengths in the figure. The black solid line, blue dashed line, red dotted line, and green dash-dot line denote theoretical values obtained from the analytical theory for full-field, phase-only, binary-phase, and binary-amplitude modulation, respectively.

Under-sampling speckle grains improves the PBR of the focus when focusing light inside a scattering medium

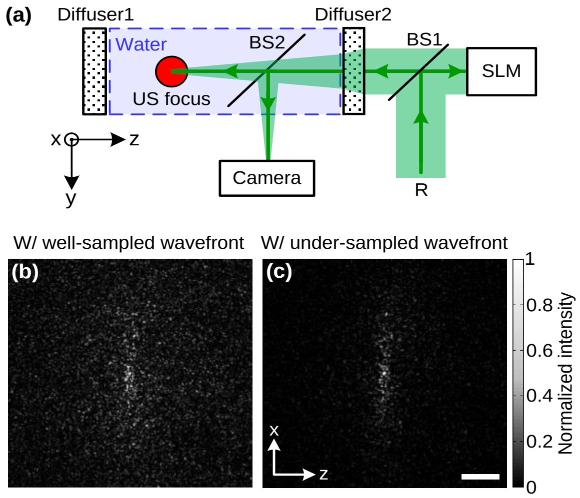

Figure 4.11 Focusing light inside a scattering medium comprising two diffusers using TRUE focusing. (a). Schematic of the set-up for observing the focus. A beamsplitter creates a copy of the focus so we can measure it with a camera outside the water tank. (b). The observed focus when speckle grains were well-sampled (2.8 × 2.8 pixels per speckle grain on average) during wavefront measurement. (c). The observed focus when speckle grains were under-sampled (F = 5) during wavefront measurement. The PBR of the focus was improved by 4 times compared with that in b. Because a 2.9-ms-long burst of ultrasound was employed, the focus was elongated along the x direction (the acoustic axis direction). BS, beamsplitter; R, reference beam; SLM, spatial light modulator; US, ultrasound (50 MHz, numerical aperture = 0.4). Scale bar, 200 µm.

Signal-to-noise ratio (SNR) of wavefront measurement when speckle grains are under-sampled

To investigate the SNR of wavefront measurement when speckle grains are under-sampled, Eq. (S4.1) is converted into a representation of the number of photoelectrons:

$$N_k = n_\mathrm{R} + \sum_{j=1}^{F} n_\mathrm{S}\left(\vec{r}_j\right) + \sum_{j=1}^{F} 2\sqrt{\frac{n_\mathrm{R}}{F} n_\mathrm{S}\left(\vec{r}_j\right)} \cos\left[\phi_\mathrm{S}\left(\vec{r}_j\right) + \left(k-1\right)\pi/2\right], k = 1,2,3,4. \tag{S4.44}$$

Here, N_k is the number of photoelectrons per pixel in each successive frame, $n_\mathrm{R} \equiv \eta A E_\mathrm{R}^2 t / \left(h\nu\right)$ is the number of photoelectrons induced by the reference beam per pixel, $n_\mathrm{S}(\vec{r}_j) \equiv \eta \left(A/F\right) E_\mathrm{S}^2\left(\vec{r}_j\right) t / \left(h\nu\right)$ is the number of photoelectrons induced by the j-th speckle grain, η is the quantum efficiency, t is the exposure time, h is Plank's constant, and v is the frequency of a photon. Considering that $\phi_\mathrm{S}\left(\vec{r}_j\right)$ is uniformly distributed between 0 and 2π, the interference component $\sum_{j=1}^{F} 2\sqrt{\frac{n_\mathrm{R}}{F} n_\mathrm{S}\left(\vec{r}_j\right)} \cos\left[\phi_\mathrm{S}\left(\vec{r}_j\right)\right]$ is a random summation of F terms. Thus,

$$\text{the signal amplitude} = \max\left\{\sum_{j=1}^{F} 2\sqrt{\frac{n_\mathrm{R}}{F} n_\mathrm{S}\left(\vec{r}_j\right)} \cos\left[\phi_\mathrm{S}\left(\vec{r}_j\right)\right]\right\} \sim \sqrt{F} \times 2\sqrt{\frac{n_\mathrm{R}}{F}\mathrm{NPS}} = 2\sqrt{n_\mathrm{R} \times \mathrm{NPS}}, \tag{S4.45}$$

where NPS is the average number of photoelectrons induced by the light exiting the sample per speckle grain. Since the major noises during wavefront measurement are the shot-noise of the reference beam and the camera readout noise, the SNR can be estimated as

$$\mathrm{SNR}_{\textbf{under-sampled}} = \frac{2\sqrt{n_\mathrm{R} \times \mathrm{NPS}}}{\sqrt{\left(\sqrt{n_\mathrm{R}}\right)^2 + {n_\mathrm{camera}}^2}}, \tag{S4.46}$$

where n_camera is the readout noise of the camera sensor. When detection is shot-noise limited ($n_\mathrm{R} >> n_\mathrm{camera}$), the SNR can be further simplified as

$$\mathrm{SNR}_{\textbf{under-sampled}} = 2\sqrt{\mathrm{NPS}}. \tag{S4.47}$$

This result indicates that when speckle grains are under-sampled, the SNR is determined only by the average photoelectron number induced by speckle grains, and is not directly related to the under-sampling factor F.

Chapter 5: Improving the focusing depth of OPC

5.1 Introduction

The thicknesses of samples used in previous OPC experiments were limited to only a few millimeters or several transport mean free paths (l_t'), which is still relatively shallow for many pre-clinical and clinical applications. For example, the thickest biological tissue used in the feedback-based wavefront shaping was 5 mm thick chicken breast tissue [69]. In an analog OPC experiment based on a photorefractive crystal, 7 mm thick chicken breast tissue [71] was used. Recently, 4 mm thick chicken breast tissue was used in a digital OPC experiment based on an electronic camera and spatial light modulators [116]. Although the principle of wavefront shaping does not impose an upper bound on the number of scattering events that can be tolerated, practical considerations such as an insufficiently strong light signal, a short speckle correlation time, and an inadequate laser coherence length can restrict the thickness of the sample through which light can be focused.

Compared with analog OPC, digital OPC (DOPC) achieves a much higher fluence reflectivity, hence is able to deliver more energy to the focus. Here, using a laser with a long coherence length and an optimized DOPC system that can safely deliver more light power, we demonstrate focusing 532 nm light through *ex vivo* chicken breast tissue up to 2.5 cm thick and through tissue-mimicking phantoms up to 9.6 cm thick. Although multiple-centimeter depth has been reached by imaging modalities such as ultrasound-modulated optical tomography [117] and photoacoustic imaging [118], the nearly 10 cm (~100 l_t') penetration has never been achieved before by any optical focusing technique.

5.2 Methods

A schematic of the DOPC set-up is shown in Fig. 5.1. A continuous-wave laser (Verdi V10, Coherent) with a coherence length longer than 100 m was used as the light source. A long coherence length is desired because OPC relies on constructive interference among different optical paths. Since the optical path-length difference is proportional to the square of the thickness of the scattering medium (as derived in Supplementary notes), the required coherence length increases quadratically with the thickness of the medium.

5.2.1 Wavefront measurement

The incident light was split into a reference beam (R) and a sample beam (S) by a polarizing beamsplitter (PBS), PBS2, with the splitting ratio controlled by a half-wave plate (HWP), HWP2. Two acousto-optic modulators (AOMs) shifted the frequency of R and S by 50 MHz + 12 Hz and 50 MHz, respectively. Thus, a beat with a frequency of f_b = 12 Hz was generated between R and S. Then, a lens pair composed of L3 and L4 expanded the beam diameter of R to 25 mm, which is able to cover the entire surface of a spatial light modulator (SLM) (Pluto NIR II, Holoeye). For S, a mirror (M), M4, mounted on a motorized linear stage (MLS) was initially moved out of the light path to position 1 (see Fig. 5.1), and a lens pair composed of L5 and L6 expanded the beam diameter of S to 34 mm. Because tissue damage is determined by the light intensity on the sample surface, a broad incident beam can safely deliver much more light power than a narrow beam, thus enhancing the signal-to-noise ratio (SNR) of wavefront measurement. In principle, to efficiently deliver power, there is an optimum illuminating beam size dependent on the property of each sample [119]. In practice, we chose a beam size that was reasonably good for most samples. The collecting lens L8, which was used in all previous OPC set-ups to collect the scattered light, was removed in our set-up to avoid focusing the reading beam onto the tissue surface in the playback step, which might otherwise cause tissue damage. After passing through the sample, S was combined with R using a 50/50 beamsplitter (BS), BS2. Their interference pattern on the SLM was imaged onto a scientific CMOS camera (sCMOS), sCMOS1 (Pco.edge 5.5, PCO-TECH), by a camera lens with a magnification of 1:1.23. To measure the phase map of S using heterodyne holography [31, 120] (see Supplementary notes for details), the camera took four successive measurements I_1, I_2, I_3, I_4 at a frame rate of 4 times the beat frequency f_b (= 48 Hz). Based on these four measurements, the phase map of the sample beam $\varphi_S(x,y)$ was calculated by $\varphi_S(x,y)=\text{Arg}[(I_1-I_3)+i(I_4-I_2)]$, where $\text{Arg}[\cdot]$ computes the principal value of the argument of a complex number. To make our technique applicable to future in vivo applications that need to accommodate the fast speckle decorrelation of living tissue (on a time scale of milliseconds [121]), the camera exposure time was set to 1 ms in all our experiments, and no averaging was used.

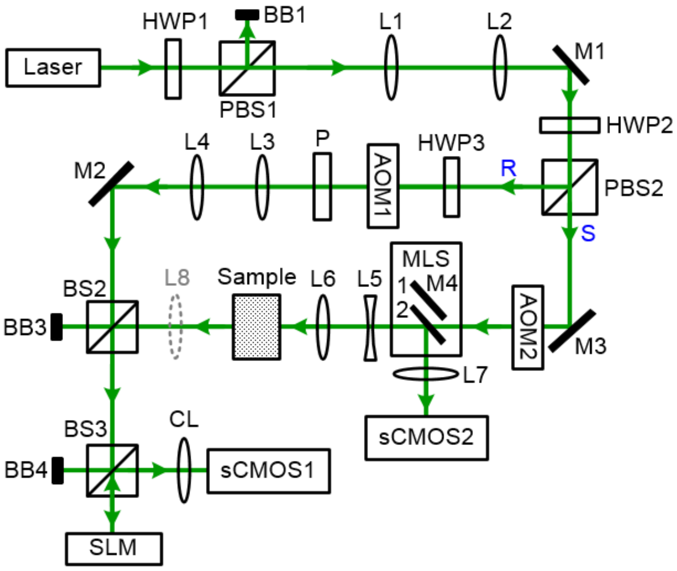

Figure 5.1 Schematic of the digital optical phase conjugation system. AOM, acousto-optic modulator; BB, beam block; BS, beamsplitter; CL, camera lens; HWP, half wave plate; L, lens; M, mirror; MLS, motorized linear stage; PBS, polarizing beamsplitter; R, reference beam; S, sample beam; sCMOS, scientific CMOS camera; SLM, spatial light modulator.

5.2.2 Wavefront reconstruction

To achieve OPC, in the playback step, the SLM displayed the conjugation of the measured phase map. In addition, S was blocked, and M4 was moved to position 2. After reflection from the SLM, R was phase modulated and became the phase conjugated light S*. Passing through the sample again, S* became collimated, reflected by M4, and focused by lens L7 onto sCMOS2. To compensate for the aberrations in the wavefront of R and the substrate curvature of the SLM, we digitally added orthogonal rectangular polynomials [122] to the SLM display, using the calibration method described in Ref. [123]. It is estimated that the entire process, starting from the beginning of the wavefront measurement to the appearance of the focus on sCMOS2, took around 0.7 second (system runtime).

5.3 Results

5.3.1 Focusing light through chicken breast tissue

We demonstrate focusing light through chicken breast tissue in Fig. 5.2. The side view of two chicken samples with 2.5 cm and 2.0 cm thickness is shown in Fig. 5.2(a). The effective areas in the left and right surfaces for light input and output were 7.2 cm × 7.2 cm, and all the other areas were masked with black aluminum foil tapes (T205-2.0, Thorlabs) to make sure that all the detected light had passed through the full thickness of the sample. All the experiments were performed within two days after sample preparation. The light intensity on the chicken tissue surface was 200 mW/cm^2, which is the same as American National Standards Institute (ANSI) safety limit. Figure 5.2(b) shows images of the OPC foci after light passed through chicken samples with thicknesses ranging from 0.5 cm to 3.0 cm. With increasing sample thickness, the speckles in the background become more and more pronounced relative to the peak intensity of the focus. When the sample was 3.0 cm thick, no focus was observed. We quantified the contrast of the focus by the peak-to-background ratio (PBR), defined as the ratio between the average intensities within and outside the focal spot (whose size is defined by the full width at half maximum). Figure 5.2(c) shows that the PBR decreases with increasing sample thickness. Theoretically, the PBR for phase-only OPC can be calculated by $\pi N/(4M)$, where N is the number of optical modes intercepted by the SLM and M is the number of optical modes in the conjugated focus [30]. Since N/M was kept roughly the same during our experiments, the PBRs should, in theory, be a constant independent of the sample thickness.

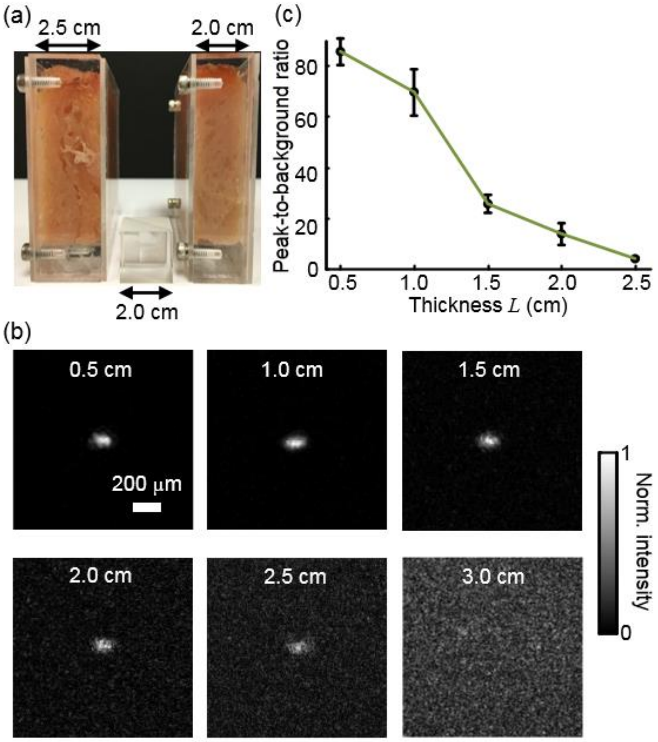

Figure 5.2 Focusing light through centimeter thick chicken breast tissue. (a) Side view of two chicken breast tissue samples with 2.5 cm and 2.0 cm thickness. A cubic beamsplitter with a side length of 2.0 cm is also shown for comparison. (b) Images of the OPC foci after light has passed through chicken breast tissue of various thicknesses. (c) Peak-to-background ratio (PBR) as a function of sample thickness. The error bar shows the standard deviation obtained from three samples of the same thickness.

To explain the observed PBR drop, we examined two possibilities. The first probability is an insufficient SNR during wavefront measurement. Since the light power transmitted through the sample decreases exponentially with increasing sample thickness (see Supplementary notes, Fig. 5.6), when the transmitted light is too weak, errors in the measured phase map may become too large, which reduces the PBR. However, by using the numerical approach described in Supplementary notes, we found that even for the 2.5 cm thick sample, the reduction of PBR due to phase errors was only around 10%. Therefore, the PBR drop is not primarily due to insufficient SNR. The second possibility is a faster speckle decorrelation rate with increasing sample thickness. The thicker the sample, the more scattering events the photons experience, and thus the shorter the speckle correlation time is [124]. In theory, the speckle correlation time is inversely proportional to the square of the sample thickness [125]. In our experiments, for samples thicker than 1.0 cm, the speckle correlation times were shorter than the system runtime. That is to say, the wavefront changed rapidly with time, and the measured wavefront was different from the correct one at the moment of playback. In this case, the PBR reduces to $\eta \times$ PBRc, where PBRc is the PBR achieved by using the correct wavefront, and η is the PBR reduction coefficient, which, in the noise-free case, is determined by the absolute square of the correlation coefficient between the measured wavefront and the correct wavefront at the moment of playback [86]. The fast speckle decorrelation for chicken tissue is due to both the intrinsic and the laser-heating induced Brownian motion of scatterers. We note that although the SNR is not the primary factor that causes the PBR drop for the 2.5 cm thick chicken sample, it can become the dominant factor for samples thicker than 3.7 cm. It is shown in Supplementary notes that in the decorrelation-free case, the PBR reduction coefficient η starts to drop exponentially when the SNR becomes smaller than 1 (SNR = 1 when thickness = 3.7 cm). For 5.0 cm and 6.0 cm thick samples, η drops to 0.017 and 0.0012, respectively, showing that insufficient SNR can significantly degrade the performance of DOPC.

5.3.2 Focusing light through tissue-mimicking phantoms

Since red blood cells in biological tissue absorb green light strongly, 532 nm is not an optimal wavelength for thick tissue [126]. To reduce the light absorption by the sample, we switched to widely-used tissue-mimicking intralipid-gelatin phantoms [55]. These phantoms have an absorption coefficient of 0.07 cm^{-1} at 532 nm, which is close to that of chicken tissue at 800 nm (0.08 cm^{-1}), but their reduced scattering coefficient at 532 nm is larger than that of chicken tissue at 800 nm (10 cm^{-1} vs. 3.5 cm^{-1}) [126]. Their scattering anisotropy g is 0.9. Compared with chicken tissue, the phantoms are more mechanically stable. Figure 5.3(a) shows two phantoms with thicknesses of 9.6 cm and 8.5 cm, along with a forearm of a 28-year-old male adult. It can be seen that our samples are even thicker than the human arm. In our experiments, the light intensity on the phantom surface was 1.2 W/cm^2, six times as high as the ANSI safety limit. However, no damage was observed in the sample after the experiment. It is worth noting that the ANSI safety limit is usually more than 10 times below the observed damage threshold. Figure 5.3(b) shows images of the OPC foci after light has passed through phantoms with thicknesses ranging from 0.8 cm to 10.0 cm. We could focus light through a sample even with a thickness of 9.6 cm, although no focus was observed when the thickness was 10.0 cm. Focusing light through a 9.6 cm thick sample by DOPC is quite remarkable, because the transmitted photons have experienced on average at least 1000 scattering events, and moreover, only a tiny portion of the entire scattered wavefront is phase conjugated (The collected light power was only 10^{-9} of the incident power on the sample). Figure 5.3(c) shows the PBR as a function of sample thickness. When the thickness is no greater than 55 mm, the values of PBRs are very similar (~170). For thicker samples, the PBR drops with increasing thickness, because the speckle correlation time becomes shorter than the system runtime for these samples. Since the transmitted light power for the 9.6 cm thick phantom is 23 times stronger than that for the 2.5 cm thick chicken sample, insufficient SNR is not a major factor that causes the PBR drop.

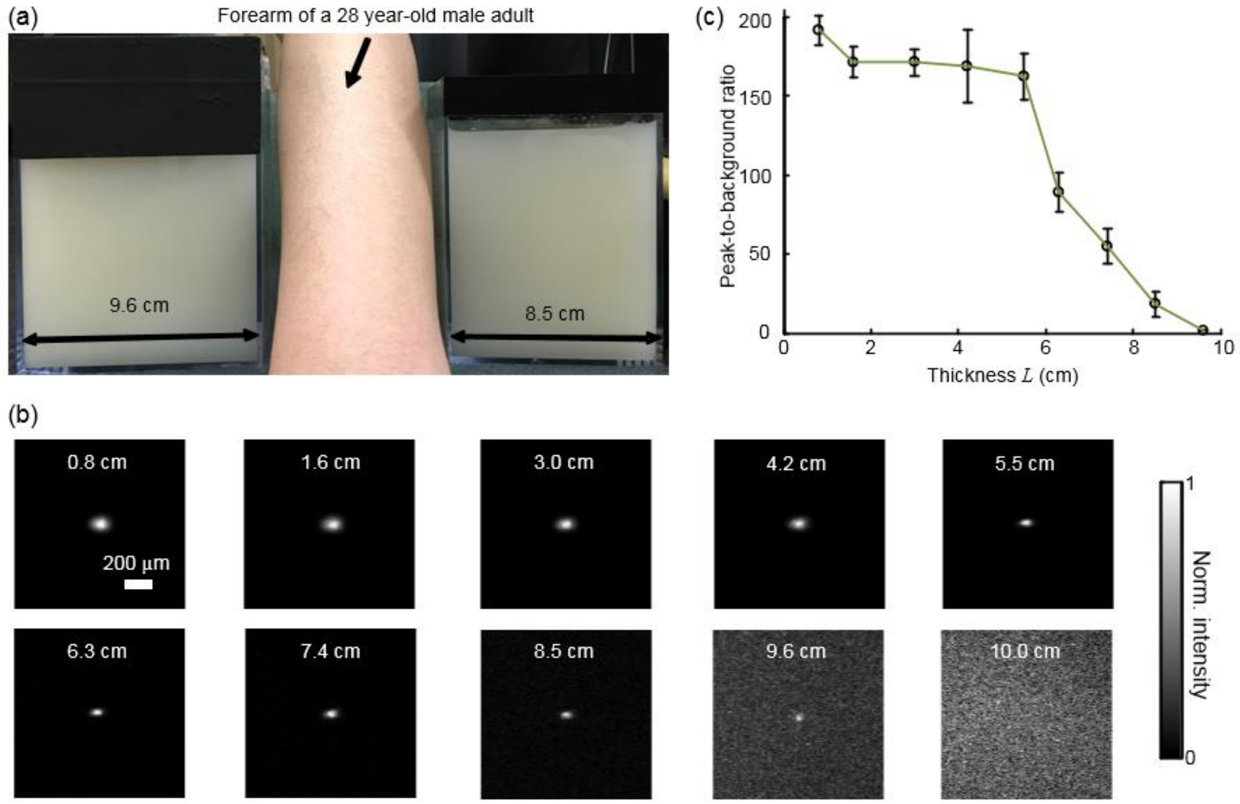

Figure 5.3 Focusing light through centimeter thick tissue-mimicking phantom. (a) Side view of the intralipid-galetin phantoms with 9.6 cm and 8.5 cm thickness. A forearm of a 28-year-old male adult is also shown for comparison. (b) Images of the OPC foci after light has passed through phantoms of various thicknesses. (c) Peak-to-background ratio (PBR) as a function of sample thickness. The error bar shows the standard deviation obtained from three samples of the same thickness.

5.4 Discussion and Conclusion

Here, we discuss the limitations of our study and potential improvements to the DOPC system. First, the fast speckle decorrelation of thick samples is the major factor that prohibits us from focusing light through thicker samples. To reduce the system runtime, we can use a faster motorized linear stage, and further optimize the data processing code. We may also use a digital micromirror device as a fast SLM, and employ single-shot phase measurement to speed up the wavefront measurement [80, 127]. Second, we note that πN/(4M) describes the PBR in which the background intensity is calculated from the average intensity within the focal spot after ensemble averaging over many illuminating wavefronts. However, when applying optical focusing in real applications, the ratio between the average intensities within and outside the focal spot is more relevant and useful, and we define this ratio as the PBR. In our definition of the PBR, the background intensity is calculated from the average intensity outside the focal spot when the incident wavefront is optimal, and it is higher than the background intensity ensemble averaged over many illuminating wavefronts (in our case it is ~5 times higher) [110]. Thus, the measured PBR is smaller than πN/(4M). For example, for a 0.8 cm thick phantom, $\pi N/(4M) \sim 9.0 \times 10^4$, while the measured PBR is only around 200. The misalignment of the system also makes the measured PBR smaller than πN/(4M). Third, assuming that we have a perfectly aligned system and extremely stable samples, the ultimate limit on the thickness of the sample that we can focus light through by OPC is determined by the SNR in the wavefront measurement (see Supplementary notes) [75]. Therefore, when the SNR is limited by shot noise rather than laser's technical noise, it is desirable to have a strong laser that delivers as much light as possible while keeping the intensity on the sample surface under the safety limit.

In conclusion, using an optimized DOPC system, we focused 532 nm light through chicken tissue up to 2.5 cm thick and through tissue-mimicking phantoms up to 9.6 cm thick. The 9.6 cm (~100 l_t') penetration has never been achieved before by any optical focusing technique, and it shows the promise of OPC-based wavefront shaping techniques to revolutionize biomedicine with deep-tissue non-invasive optical imaging, manipulation, and therapy.

5.5 Supplementary notes

5.5.1 Requirement of laser coherence length in OPC experiments

Since focusing light through or inside scattering media by OPC relies on constructive interference of light that has propagated through different optical paths inside a scattering medium, a long laser coherence length is required. Ideally, the laser coherence length should be longer than the optical path-length difference among the various paths. Here, we develop an analytical model to estimate the path-length difference in a scattering medium. Based on diffusion theory for an infinite medium, under a first-order approximation, a pencil beam illuminating a scattering medium can be modeled as an isotropic source located one transport mean free path (1 l_t') beneath the sample surface [8, 128] (see Fig. 5.4(a)). At time t, the laser fluence rate at a distance *r* from the isotropic point source can be calculated by [8]

$$\phi(r,t>r/c)=\frac{c}{(4\pi Dct)^{3/2}}\exp(-\frac{r^2}{4Dct}-\mu_a ct), \tag{S5.1}$$

where *c* is the speed of light in the scattering medium and *D* is the diffusion coefficient. *D* = $1/[3(\mu_a+\mu_s')]$, where μ_a and μ_s' are the absorption coefficient and the reduced scattering coefficient of the scattering medium. The point source is placed at the origin of the coordinate system. For mathematical convenience, we first assume that μa is zero. The effect of nonzero μa on the path-length difference will be discussed at the end of this section. At a given location *r*, Fig. 5.4(b) shows the normalized $\phi(r,t)$ with respect to the time delay *t*. By setting the partial derivative with respect to t to zero, we find that the time delay for the maximum fluence rate is $t_{\max}=r^2/6Dc$. That is to say, photons are most likely to spend time $t_{\max}$ to reach position *r*. In order to allow photons to interfere efficiently at position *r*, the laser coherence time should at least reach the full width at half maximum (FWHM) of the distribution. By multiplying the coherence time with *c*, the minimum laser coherence length is obtained.

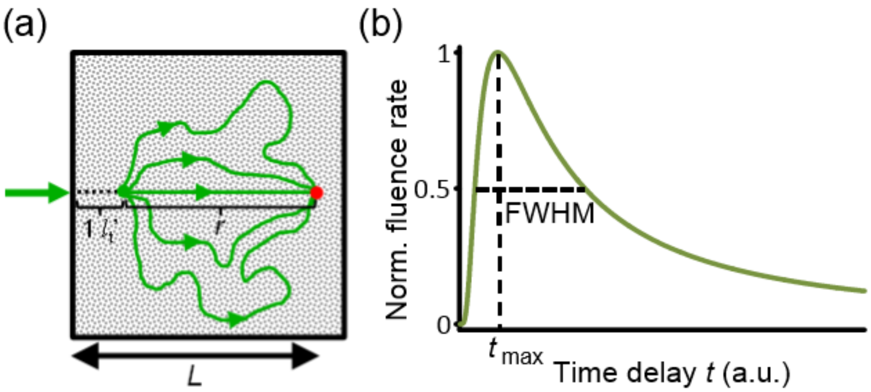

Figure 5.4 Path-length distribution of photons in scattering medium. (a) Schematic of photon paths to reach the location denoted by the red dot in a scattering medium. (b) Normalized photon fluence rate as a function of time delay *t* at a given position *r*.

To determine the two moments t_{left} and t_{right} when the normalized fluence rate drops to 0.5, based on Eq. (S5.1) and $t_{\max} = r^2/6Dc$, we write the following equation:

$$\frac{\phi}{\phi(t_{\max})} = \left(\frac{t_{\max}}{t}\right)^{3/2} \exp\left(-\frac{r^2}{4Dct}\right)\exp\left(\frac{3}{2}\right) = \frac{1}{2}, \qquad \text{(S5.2)}$$

which can be re-written as

$$\left(\frac{1}{t}\right)^{3/2} \exp\left(-\frac{r^2}{4Dct}\right) = \frac{1}{2}\left(\frac{1}{et_{\max}}\right)^{3/2}. \qquad \text{(S5.3)}$$

For equations in the format of $(1/t)^{3/2}\exp(-a/t) = b$, where *a* and *b* are constants, the solution is given by

$$\frac{1}{t} = -\frac{3}{2a} W\left(-\frac{2}{3}ab^{2/3}\right), \qquad \text{(S5.4)}$$

where $W(\cdot)$ is the multivalued Lambert-W function. After substituting $a = r^2/(4Dc)$ and $b = 0.5(et_{\max})^{-3/2}$ into Eq. (S5.4), we get

$$t = -\frac{t_{\max}}{W[-0.5^{2/3}/e]}. \tag{S5.5}$$

Thus,

$$\begin{aligned} t_{\text{left}} &= -\frac{t_{\max}}{W_{-1}\left[-0.5^{2/3}/e\right]} \approx -\frac{t_{\max}}{-2.291} \approx 0.4364 t_{\max}, \\ t_{\text{right}} &= -\frac{t_{\max}}{W_{0}\left[-0.5^{2/3}/e\right]} \approx -\frac{t_{\max}}{-0.3188} \approx 3.137 t_{\max}, \end{aligned} \tag{S5.6}$$

where W_{-1} and W_0 are the two main branches of the Lambert-W function. So, in order to focus light to a location at a depth L beneath the sample surface, the laser coherence length should be greater than $c(t_{\text{right}} - t_{\text{left}}) = 2.701 c t_{\max} = \frac{r^2}{2.2D} = \frac{\left(L - l_{\text{t}}'\right)^2}{2.2D}$. As an example, to focus light L = 10 cm deep inside a scattering medium (l_{t}' = 1 mm, D = 0.33 mm), the laser coherence length should be at least 13.5 m. Since the optical path-length difference is roughly proportional to the square of the thickness of the scattering medium, the required coherence length should increase quadratically with the sample thickness.

When a nonzero absorption coefficient is taken into account, we numerically find that the FWHM time span shown in Fig. 5.4(b) becomes narrower. In general, the larger the absorption coefficient, the narrower the FWHM time span. This can be understood by the fact that a photon with a longer time of arrival is more likely to be absorbed by the scattering medium, compared with a photon with a shorter time of arrival. Therefore, absorption in the scattering medium can reduce the required laser coherence length.

5.5.2 Effects of phase errors in the measured wavefront on the quality of DOPC

Here, we discuss the effect of the accuracy of the measured phase map on the quality of DOPC. To quantify the phase errors in the measured phase map, we start by describing the heterodyne holography method [31, 120] that we used to reconstruct the phase map. In our experiment, the reference beam and the sample beam beat at a frequency of f_b (= 12 Hz), so the light intensity can be written as

$$I(x,y,t) = E_R^2 + E_S^2(x,y) + 2E_R E_S(x,y)\cos\left[2\pi f_b t + \varphi_S(x,y) - \varphi_R\right], \qquad \text{(S5.7)}$$

where E_R and $E_S(x,y)$ are the amplitudes of the electric fields of the reference beam and the sample beam, and φ_R and $\varphi_S(x,y)$ are the phases of the electric fields of the reference beam and the sample beam. The constant prefactor that converts the electric field to intensity is neglected here, and φ_R is assumed to be a constant value of 0 for simplicity. To determine $\varphi_S(x,y)$, the camera takes four successive measurements at a frame rate of 4 f_b:

$$\begin{aligned}
I_1(x,y) &= {E_R}^2 + E_S^2(x,y) + 2E_R E_S(x,y)\cos[\varphi_S(x,y)],\\
I_2(x,y) &= {E_R}^2 + E_S^2(x,y) + 2E_R E_S(x,y)\cos[\pi/2 + \varphi_S(x,y)],\\
I_3(x,y) &= {E_R}^2 + E_S^2(x,y) + 2E_R E_S(x,y)\cos[\pi + \varphi_S(x,y)],\\
I_4(x,y) &= {E_R}^2 + E_S^2(x,y) + 2E_R E_S(x,y)\cos[3\pi/2 + \varphi_S(x,y)].
\end{aligned} \qquad \text{(S5.8)}$$

Based on these four measurements, the phase of the sample beam $\varphi_S(x,y)$ can be calculated by

$$\varphi_S(x,y) = \mathrm{Arg}[(I_1 - I_3) + i(I_4 - I_2)], \qquad \text{(S5.9)}$$

where $\mathrm{Arg}[\cdot]$ computes the principal value of the argument of a complex number.

When the scattering medium is thick, the intensity of the sample beam after passing through the scattering medium is orders of magnitude weaker than the intensity of the reference beam, so the major noises in the above measurements are the shot noise of the reference beam and the readout noise of the camera. After converting Eq. (S5.8) into a representation of the photoelectron number, we express the SNR as

$$\mathrm{SNR}=\frac{2\sqrt{N_R N_S}}{\sqrt{(\sqrt{N_R})^2+{N_{\mathrm{camera}}}^2}}, \tag{S5.10}$$

where N_R, N_S, and N_{camera} are the number of photoelectrons corresponding to the reference beam, the sample beam, and the camera readout noise, respectively. By using a numerical method similar to that reported in Ref. [75], we estimated the phase errors in the measured phase map. As an example, we used the experimental data obtained from the 2.5 cm thick chicken tissue sample to set the parameters in the following simulation. For the sample beam, the average number of photoelectrons per pixel was 5.7 (exposure time = 1 ms). So, to mimic fully developed speckles, N_S was drawn from an exponential distribution with a mean value of 5.7, and $\varphi_S(x,y)$ was drawn from a uniform distribution ranging from 0 to 2π. For the reference beam, the average number of photoelectrons per pixel was roughly 6000, which satisfied a Poisson distribution [129]. To take the shot noise into consideration, N_R was drawn from a Poisson distribution with a mean value of 6000 for each measurement. N_{camera} was also added to each measurement by drawing from a normal distribution with a mean of 0 and a standard deviation of 3.6. By substituting the above parameters into Eqs. (S5.8 – S5.9), we obtained the phase map under the influence of noise. The phase errors, defined as the differences between the computed phase values and the preset phase values, were then calculated.

Figure 5.5 shows the probability density function (PDF) of the phase errors for the 2.5 cm thick chicken tissue sample calculated from 10^6 data points in one simulated phase map. The standard deviation of the phase errors was found to be 0.115π. Using this phase map in the playback, the focal peak-to-background ratio (PBR) can be calculated as

$$\mathrm{PBR} = \eta \times \mathrm{PBR_c} = \left| \sum_{j=1}^{10^6} e^{i\varphi_j} \Big/ \sum_{j=1}^{10^6} 1 \right|^2 \times \mathrm{PBR_c}, \tag{S5.11}$$

where PBRc is the PBR achieved by using the correct wavefront and η is the PBR reduction coefficient, which is determined by the absolute square of the correlation coefficient between the measured wavefront and the correct wavefront. Based on Eq. (S5.11), η = 90%, so the reduction of PBR due to phase errors was only around 10%.

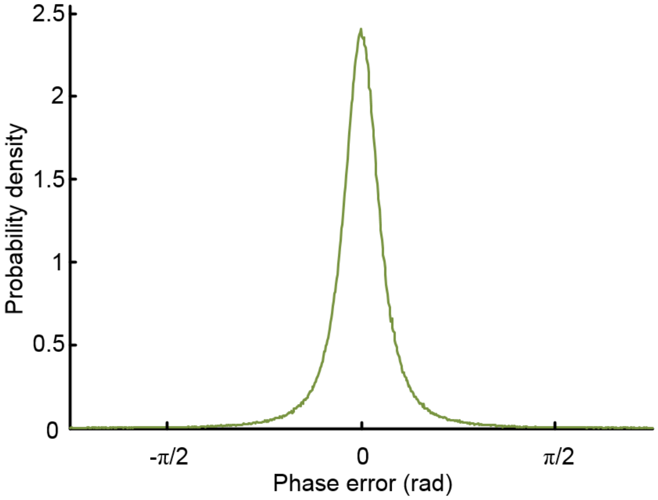

Figure 5.5 Probability density function of the phase errors calculated from 10^6 data points in one simulated phase map. The simulation parameters were chosen based on the experimental conditions with the 2.5 cm thick chicken tissue sample.

We can further apply this numerical approach to predict the PBRs for chicken tissue samples beyond 3.0 cm. Figure 5.6 shows the experimentally measured transmitted light power (expressed in number of photoelectrons per camera pixel) for chicken tissue samples with thicknesses ranging from 0.5 cm to 2.5 cm. The transmitted light power decayed exponentially with a decay constant of 2.7 cm^{-1}, which is close to the effective attenuation coefficient of chicken tissue at 532 nm [126]. Through extrapolation, this exponential relation enables us to obtain the transmitted light levels for samples thicker than 3.0 cm, which are too small to be measured accurately. Although the average number of photoelectrons detected on each camera pixel corresponding to the sample beam can be well below unity for samples thicker than 3.0 cm, the heterodyne gain provided by the reference beam boosts the signal above the noise level of the camera. In this case, the measurement becomes shot-noise limited, rather than camera readout noise limited.

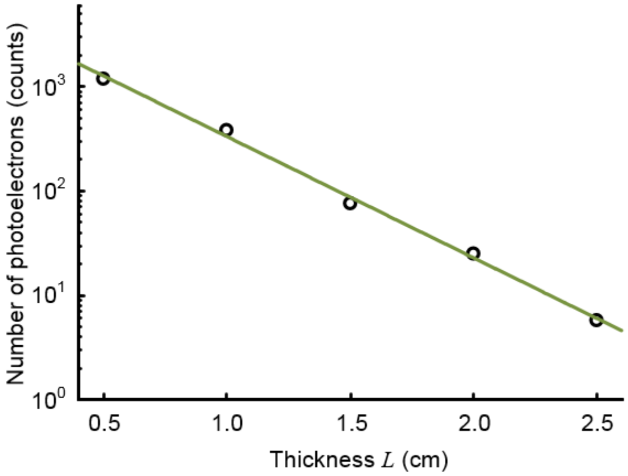

Figure 5.6 Experimentally measured average transmitted sample light power detected on each camera pixel (expressed in number of photoelectrons) as a function of sample thickness. Based on curve fitting, the decay constant is 2.7 cm^{-1}.

Figure 5.7 shows the simulated PDFs of the phase errors for chicken tissue samples with thicknesses ranging from 3.0 cm to 6.0 cm. The phase errors become more and more uniformly distributed between $-\pi$ and π with increasing thickness. In order to quantify how these phase errors affect the performance of DOPC, we used Eq. (S5.11) to calculate the PRB reduction coefficient η as a function of sample thickness, which is shown in Fig. 5.8. When the sample thickness is smaller than 3.7 cm, η is roughly a constant value close to 1. However, when the samples are thicker than 3.7 cm, η starts to decrease exponentially. Thus, a turning point is observed around thickness L = 3.7 cm, which actually corresponds to the SNR being 1. Based on Eq. (S5.10), when the camera readout noise is much smaller than the shot noise, the expression for the SNR can be simplified to $2\sqrt{N_S}$. Since N_S decreases exponentially with increasing sample thickness, SNR also decreases exponentially with increasing sample thickness. When the sample is thicker than 3.7 cm, the SNR becomes smaller than 1, and η starts to drop exponentially and reaches 0.017 at 5.0 cm and 0.0012 at 6.0 cm. These small values of η beyond the turning point demonstrate that insufficient transmitted sample light power can significantly degrade the performance of DOPC when focusing light through samples thicker than 3.7 cm.

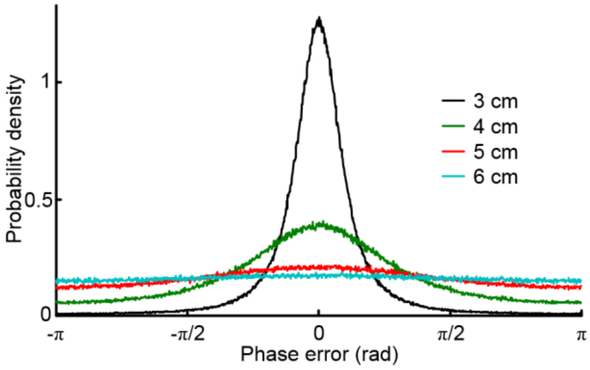

Figure 5.7 Probability density functions of phase errors in the simulated phase maps for chicken tissue samples with thicknesses ranging from 3.0 cm to 6.0 cm.

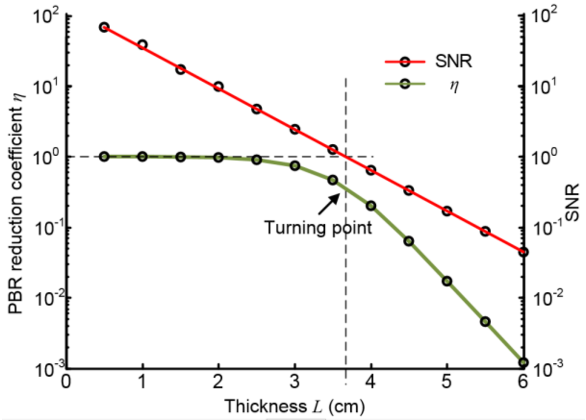

Figure 5.8 Peak-to-background ratio (PBR) reduction coefficient η and the SNR as a function of chicken tissue sample thickness.

References

1. W. Denk, J. Strickler, and W. Webb, "Two-photon laser scanning fluorescence microscopy," Science **248**, 73-76 (1990).

2. J. Pawley, *Handbook of biological confocal microscopy* (Springer, 2010).

3. D. Huang, E. A. Swanson, C. P. Lin, J. S. Schuman, W. G. Stinson, W. Chang, M. R. Hee, T. Flotte, K. Gregory, and C. A. Puliafito, "Optical coherence tomography," Science **254**, 1178-1181 (1991).

4. D. G. Grier, "A revolution in optical manipulation," Nature **424**, 810-816 (2003).

5. E. S. Boyden, F. Zhang, E. Bamberg, G. Nagel, and K. Deisseroth, "Millisecond-timescale, genetically targeted optical control of neural activity," Nat Neurosci **8**, 1263-1268 (2005).

6. M. F. Yanik, H. Cinar, H. N. Cinar, A. D. Chisholm, Y. Jin, and A. Ben-Yakar, "Neurosurgery: Functional regeneration after laser axotomy," Nature **432**, 822-822 (2004).

7. X. Huang, W. Qian, I. H. El-Sayed, and M. A. El-Sayed, "The potential use of the enhanced nonlinear properties of gold nanospheres in photothermal cancer therapy," Lasers in surgery and medicine **39**, 747-753 (2007).

8. L. V. Wang and H. Wu, *Biomedical optics : principles and imaging* (Wiley-Interscience, Hoboken, N.J., 2007), pp. xiv, 362 p.

9. V. Ntziachristos, "Going deeper than microscopy: the optical imaging frontier in biology," Nat Methods **7**, 603-614 (2010).

10. Y. Liu, C. Zhang, and L. V. Wang, "Effects of light scattering on optical-resolution photoacoustic microscopy," J Biomed Opt **17**, 126014 (2012).

11. L. V. Wang and G. Liang, "Absorption distribution of an optical beam focused into a turbid medium," Appl Optics **38**, 4951-4958 (1999).

12. A. P. Mosk, A. Lagendijk, G. Lerosey, and M. Fink, "Controlling waves in space and time for imaging and focusing in complex media," Nat Photonics **6**, 283-292 (2012).

13. R. Horstmeyer, H. Ruan, and C. Yang, "Guidestar-assisted wavefront-shaping methods for focusing light into biological tissue," Nat Photon **9**, 563-571 (2015).

14. I. M. Vellekoop, "Feedback-based wavefront shaping," Opt Express **23**, 12189-12206 (2015).

15. I. M. Vellekoop and A. P. Mosk, "Focusing coherent light through opaque strongly scattering media," Opt Lett **32**, 2309-2311 (2007).

16. S. Popoff, G. Lerosey, R. Carminati, M. Fink, A. Boccara, and S. Gigan, "Measuring the transmission matrix in optics: an approach to the study and control of light propagation in disordered media," Phys Rev Lett **104**, 100601 (2010).

17. M. Cui, "A high speed wavefront determination method based on spatial frequency modulations for focusing light through random scattering media," Opt Express **19**, 2989-2995 (2011).

18. Z. Yaqoob, D. Psaltis, M. S. Feld, and C. Yang, "Optical phase conjugation for turbidity suppression in biological samples," Nat Photonics **2**, 110-115 (2008).

19. M. Cui and C. Yang, "Implementation of a digital optical phase conjugation system and its application to study the robustness of turbidity suppression by phase conjugation," Opt Express **18**, 3444-3455 (2010).

20. C.-L. Hsieh, Y. Pu, R. Grange, G. Laporte, and D. Psaltis, "Imaging through turbid layers by scanning the phase conjugated second harmonic radiation from a nanoparticle," Opt Express **18**, 20723-20731 (2010).

21. C. Ma, F. Zhou, Y. Liu, and L. V. Wang, "Single-exposure optical focusing inside scattering media using binarized time-reversed adapted perturbation," Optica **2**, 869-876 (2015).

22. A. Yariv, "Phase conjugate optics and real-time holography," IEEE Journal of Quantum Electronics **14**, 650-660 (1978).

23. G. S. He, "Optical phase conjugation: principles, techniques, and applications," Progress in Quantum Electronics **26**, 131-191 (2002).

24. Y. Liu, P. Lai, C. Ma, X. Xu, A. A. Grabar, and L. V. Wang, "Optical focusing deep inside dynamic scattering media with near-infrared time-reversed ultrasonically encoded (TRUE) light," Nat Commun **6**, 5904 (2015).

25. B. Judkewitz, Y. M. Wang, R. Horstmeyer, A. Mathy, and C. Yang, "Speckle-scale focusing in the diffusive regime with time reversal of variance-encoded light (TROVE)," Nat Photon **7**, 300-305 (2013).

26. C. Ma, X. Xu, Y. Liu, and L. V. Wang, "Time-reversed adapted-perturbation (TRAP) optical focusing onto dynamic objects inside scattering media," Nat Photon **8**, 931-936 (2014).

27. E. H. Zhou, H. Ruan, C. Yang, and B. Judkewitz, "Focusing on moving targets through scattering samples," Optica **1**, 227-232 (2014).

28. H. Ruan, M. Jang, and C. Yang, "Optical focusing inside scattering media with time-reversed ultrasound microbubble encoded light," Nat Commun **6**, 8968 (2015).

29. X. Xu, H. Liu, and L. V. Wang, "Time-reversed ultrasonically encoded optical focusing into scattering media," Nat Photonics **5**, 154-157 (2011).

30. Y. M. Wang, B. Judkewitz, C. A. DiMarzio, and C. Yang, "Deep-tissue focal fluorescence imaging with digitally time-reversed ultrasound-encoded light," Nat Commun **3**, 928 (2012).

31. K. Si, R. Fiolka, and M. Cui, "Fluorescence imaging beyond the ballistic regime by ultrasound-pulse-guided digital phase conjugation," Nat Photon **6**, 657-661 (2012).

32. Y. Liu, C. Ma, Y. Shen, and L. V. Wang, "Bit-efficient, sub-millisecond wavefront measurement using a lock-in camera for time-reversal based optical focusing inside scattering media," Opt Lett **41**, 1321-1324 (2016).

33. Y. Liu, Y. Shen, C. Ma, J. Shi, and L. V. Wang, "Lock-in camera based heterodyne holography for ultrasound-modulated optical tomography inside dynamic scattering media," Applied Physics Letters **108**, 231106 (2016).

34. Y. Shen, Y. Liu, C. Ma, and L. V. Wang, "Focusing light through scattering media by full-polarization digital optical phase conjugation," Opt Lett **41**, 1130-1133 (2016).

35. Y. Shen, Y. Liu, C. Ma, and L. V. Wang, "Sub-Nyquist sampling boosts targeted light transport through opaque scattering media," arXiv preprint arXiv:1611.01404 (2016).

36. Y. Shen, Y. Liu, C. Ma, and L. V. Wang, "Focusing light through biological tissue and tissue-mimicking phantoms up to 9.6 cm in thickness with digital optical phase conjugation," J Biomed Opt **21**, 085001 (2016).

37. L. V. Wang, S. L. Jacques, and L. Q. Zheng, "MCML - Monte-Carlo Modeling of Light Transport in Multilayered Tissues," Comput Meth Prog Bio **47**, 131-146 (1995).

38. Y. Liu, C. Zhang, S. Hu, Y. Suzuki, Z. Xu, S. Ferradal, and L. V. Wang, "Effect of light scattering on optical-resolution photoacoustic microscopy," Proc. SPIE **8223**, 82233S (2012).

39. A. Tycho, T. M. Jorgensen, H. T. Yura, and P. E. Andersen, "Derivation of a Monte Carlo method for modeling heterodyne detection in optical coherence tomography systems," Appl Optics **41**, 6676-6691 (2002).

40. F. Zhang, M. Kinnunen, A. Popov, and R. Myllylä, "Monte Carlo method for simulating optical coherence tomography signal in homogeneous turbid media," Proceedings of SPIE, 702213-702213 (2007).

41. B. E. A. Saleh and M. C. Teich, *Fundamentals of photonics*, 2nd ed., Wiley series in pure and applied optics (Wiley-Interscience, Hoboken, N.J., 2007).

42. K. Maslov, H. F. Zhang, S. Hu, and L. V. Wang, "Optical-resolution photoacoustic microscopy for in vivo imaging of single capillaries," Opt Lett **33**, 929-931 (2008).

43. C. K. Hayakawa, V. Venugopalan, V. V. Krishnamachari, and E. O. Potma, "Amplitude and Phase of Tightly Focused Laser Beams in Turbid Media," Phys Rev Lett **103**(2009).

44. P. Theer and W. Denk, "On the fundamental imaging-depth limit in two-photon microscopy," J Opt Soc Am A **23**, 3139-3149 (2006).

45. L. Thrane, H. T. Yura, and P. E. Andersen, "Analysis of optical coherence tomography systems based on the extended Huygens-Fresnel principle," J Opt Soc Am A **17**, 484-490 (2000).

46. L. Thrane, M. H. Frosz, T. M. Jorgensen, A. Tycho, H. T. Yura, and P. E. Andersen, "Extraction of optical scattering parameters and attenuation compensation in optical coherence tomography images of multilayered tissue structures," Opt Lett **29**, 1641-1643 (2004).

47. N. J. Durr, C. T. Weisspfennig, B. A. Holfeld, and A. Ben-Yakar, "Maximum imaging depth of two-photon autofluorescence microscopy in epithelial tissues," J Biomed Opt **16**, 026008 (2011).

48. E. Alerstam, W. C. Y. Lo, T. D. Han, J. Rose, S. Andersson-Engels, and L. Lilge, "Next-generation acceleration and code optimization for light transport in turbid media using GPUs," Biomed Opt Express **1**, 658-675 (2010).

49. M. Gross, P. Goy, B. C. Forget, M. Atlan, F. Ramaz, A. C. Boccara, and A. K. Dunn, "Heterodyne detection of multiply scattered monochromatic light with a multipixel detector," Opt Lett **30**, 1357-1359 (2005).

50. A. Lev and B. Sfez, "In vivo demonstration of the ultrasound-modulated light technique," J. Opt. Soc. Am. A **20**, 2347-2354 (2003).

51. A. A. Grabar, I. V. Kedyk, I. M. Stoika, Y. M. Vysochanskii, M. Jazbinsek, G. Montemezzani, and P. Günter, "Enhanced photorefractive properties of Te-doped Sn2P2S6," in *Photorefractive Effects, Materials, and Devices*, OSA Trends in Optics and Photonics (Optical Society of America, 2003), 10.

52. A. A. Grabar, M. Jazbinšek, A. N. Shumelyuk, Y. M. Vysochanskii, G. Montemezzani, and P. Günter, "Photorefractive effects in Sn2P2S6," in *Photorefractive Materials and Their Applications 2* (Springer, 2007), pp. 327-362.

53. T. Bach, M. Jazbin?ek, G. Montemezzani, P. Günter, A. A. Grabar, and Y. M. Vysochanskii, "Tailoring of infrared photorefractive properties of Sn2P2S6 crystals by Te and Sb doping," J. Opt. Soc. Am. B **24**, 1535-1541 (2007).

54. R. Weissleder and V. Ntziachristos, "Shedding light onto live molecular targets," Nature medicine **9**, 123-128 (2003).

55. P. Lai, X. Xu, and L. V. Wang, "Dependence of optical scattering from Intralipid in gelatin-gel based tissue-mimicking phantoms on mixing temperature and time," J Biomed Opt **19**, 035002 (2014).

56. L. Wang and S. L. Jacques, "Use of a laser beam with an oblique angle of incidence to measure the reduced scattering coefficient of a turbid medium," Appl Optics **34**, 2362-2366 (1995).

57. I. M. Vellekoop, "Controlling the propagation of light in disordered scattering media," PhD thesis, 2008).

58. D. D. Duncan and S. J. Kirkpatrick, "Can laser speckle flowmetry be made a quantitative tool?," JOSA A **25**, 2088-2094 (2008).

59. M. Fox, *Quantum optics: an introduction* (OUP Oxford, 2006), Vol. 15.

60. W. Leutz and G. Maret, "Ultrasonic modulation of multiply scattered light," Physica B: Condensed Matter **204**, 14-19 (1995).

61. L. V. Wang, "Mechanisms of ultrasonic modulation of multiply scattered coherent light: an analytic model," Phys Rev Lett **87**, 043903 (2001).

62. P. Lai, X. Xu, H. Liu, Y. Suzuki, and L. V. Wang, "Reflection-mode time-reversed ultrasonically encoded optical focusing into turbid media," J Biomed Opt **16**(2011).

63. P. Lai, Y. Suzuki, X. Xu, and L. V. Wang, "Focused fluorescence excitation with time-reversed ultrasonically encoded light and imaging in thick scattering media," Laser Physics Letters **10**, 075604 (2013).

64. Y. Suzuki, X. Xu, P. Lai, and L. V. Wang, "Energy enhancement in time-reversed ultrasonically encoded optical focusing using a photorefractive polymer," J Biomed Opt **17**, 080507 (2012).

65. J. D. Briers and S. Webster, "Laser speckle contrast analysis (LASCA): a nonscanning, full-field technique for monitoring capillary blood flow," J Biomed Opt **1**, 174-179 (1996).

66. Y. Zhou, J. Liang, K. I. Maslov, and L. V. Wang, "Calibration-free in vivo transverse blood flowmetry based on cross correlation of slow time profiles from photoacoustic microscopy," Opt Lett **38**, 3882-3885 (2013).

67. J. Yao, K. I. Maslov, Y. Shi, L. A. Taber, and L. V. Wang, "In vivo photoacoustic imaging of transverse blood flow by using Doppler broadening of bandwidth," Opt Lett **35**, 1419-1421 (2010).

68. D. B. Conkey, A. M. Caravaca-Aguirre, and R. Piestun, "High-speed scattering medium characterization with application to focusing light through turbid media," Opt Express **20**, 1733-1740 (2012).

69. C. Stockbridge, Y. Lu, J. Moore, S. Hoffman, R. Paxman, K. Toussaint, and T. Bifano, "Focusing through dynamic scattering media," Opt Express **20**, 15086-15092 (2012).

70. P. Günter and J.-P. Huignard, *Photorefractive materials and their applications* (Springer, 2007).

71. M. Cui, E. J. McDowell, and C. Yang, "An in vivo study of turbidity suppression by optical phase conjugation (TSOPC) on rabbit ear," Opt Express **18**, 25-30 (2010).

72. R. Bonner and R. Nossal, "Model for laser Doppler measurements of blood flow in tissue," Appl Optics **20**, 2097-2107 (1981).

73. M. Lesaffre, F. Jean, F. Ramaz, A.-C. Boccara, M. Gross, P. Delaye, and G. Roosen, "In situ monitoring of the photorefractive response time in a self-adaptive wavefront holography setup developed for acousto-optic imaging," Opt Express **15**, 1030-1042 (2007).

74. I. Yamaguchi and T. Zhang, "Phase-shifting digital holography," Opt Lett **22**, 1268-1270 (1997).

75. M. Jang, H. Ruan, B. Judkewitz, and C. Yang, "Model for estimating the penetration depth limit of the time-reversed ultrasonically encoded optical focusing technique," Opt Express **22**, 5787-5807 (2014).

76. Y. Suzuki, J. W. Tay, Q. Yang, and L. V. Wang, "Continuous scanning of a time-reversed ultrasonically encoded optical focus by reflection-mode digital phase conjugation," Opt Lett **39**, 3441-3444 (2014).

77. Y. Suzuki and L. V. Wang, "Frequency-swept time-reversed ultrasonically encoded optical focusing," Applied Physics Letters **105**, 191108 (2014).

78. S. Bourquin, P. Seitz, and R. P. Salathé, "Optical coherence topography based on a two-dimensional smart detector array," Opt Lett **26**, 512-514 (2001).

79. R. Patel, S. Achamfuo-Yeboah, R. Light, and M. Clark, "Widefield heterodyne interferometry using a custom CMOS modulated light camera," Opt Express **19**, 24546-24556 (2011).

80. D. Wang, E. H. Zhou, J. Brake, H. Ruan, M. Jang, and C. Yang, "Focusing through dynamic tissue with millisecond digital optical phase conjugation," Optica **2**, 728-735 (2015).

81. K. Si, R. Fiolka, and M. Cui, "Breaking the spatial resolution barrier via iterative sound-light interaction in deep tissue microscopy," Scientific reports **2**, 748 (2012).

82. H. Ruan, M. Jang, B. Judkewitz, and C. Yang, "Iterative Time-Reversed Ultrasonically Encoded Light Focusing in Backscattering Mode," Scientific reports **4**, 7156 (2014).

83. A. M. Caravaca-Aguirre, E. Niv, D. B. Conkey, and R. Piestun, "Real-time resilient focusing through a bending multimode fiber," Opt Express **21**, 12881-12887 (2013).

84. D. Kim, J. Moon, M. Kim, T. D. Yang, J. Kim, E. Chung, and W. Choi, "Toward a miniature endomicroscope: pixelation-free and diffraction-limited imaging through a fiber bundle," Opt Lett **39**, 1921-1924 (2014).

85. X. Tao, Z. Dean, C. Chien, O. Azucena, D. Bodington, and J. Kubby, "Shack-Hartmann wavefront sensing using interferometric focusing of light onto guide-stars," Opt Express **21**, 31282-31292 (2013).

86. M. Jang, H. Ruan, I. M. Vellekoop, B. Judkewitz, E. Chung, and C. Yang, "Relation between speckle decorrelation and optical phase conjugation (OPC)-based turbidity suppression through dynamic scattering media: a study on in vivo mouse skin," Biomed Opt Express **6**, 72-85 (2015).

87. R. Fiolka, K. Si, and M. Cui, "Parallel wavefront measurements in ultrasound pulse guided digital phase conjugation," Opt Express **20**, 24827-24834 (2012).

88. A. Drémeau, A. Liutkus, D. Martina, O. Katz, C. Schülke, F. Krzakala, S. Gigan, and L. Daudet, "Reference-less measurement of the transmission matrix of a highly scattering material using a DMD and phase retrieval techniques," Opt Express **23**, 11898-11911 (2015).

89. X. Tao, D. Bodington, M. Reinig, and J. Kubby, "High-speed scanning interferometric focusing by fast measurement of binary transmission matrix for channel demixing," Opt Express **23**, 14168-14187 (2015).

90. X. Zhang and P. Kner, "Binary wavefront optimization using a genetic algorithm," Journal of Optics **16**, 125704 (2014).

91. D. Akbulut, T. J. Huisman, E. G. van Putten, W. L. Vos, and A. P. Mosk, "Focusing light through random photonic media by binary amplitude modulation," Opt Express **19**, 4017-4029 (2011).

92. J. W. Tay, J. Liang, and L. V. Wang, "Amplitude-masked photoacoustic wavefront shaping and application in flowmetry," Opt Lett **39**, 5499-5502 (2014).

93. S. N. Chandrasekaran, H. Ligtenberg, W. Steenbergen, and I. M. Vellekoop, "Using digital micromirror devices for focusing light through turbid media," in 2014), 897905-897905-897910.

94. I. M. Vellekoop, M. Cui, and C. Yang, "Digital optical phase conjugation of fluorescence in turbid tissue," Applied Physics Letters **101**, 081108 (2012).

95. T. Kurokawa and S. Fukushima, "Spatial light modulators using ferroelectric liquid crystal," Optical and Quantum Electronics **24**, 1151-1163 (1992).

96. M. Azimipour, F. Atry, and R. Pashaie, "Calibration of digital optical phase conjugation setups based on orthonormal rectangular polynomials," Appl Optics **55**, 2873-2880 (2016).

97. J. A. Kubby, *Adaptive Optics for Biological Imaging* (CRC press, 2013).

98. P. R. Dmochowski, B. R. Hayes-Gill, M. Clark, J. A. Crowe, M. G. Somekh, and S. P. Morgan, "Camera pixel for coherent detection of modulated light," Electronics Letters **40**, 1403-1404 (2004).

99. K. Barjean, K. Contreras, J.-B. Laudereau, É. Tinet, D. Ettori, F. Ramaz, and J.-M. Tualle, "Fourier transform acousto-optic imaging with a custom-designed CMOS smart-pixels array," Opt Lett **40**, 705-708 (2015).

100. S. Tripathi, R. Paxman, T. Bifano, and K. C. Toussaint, "Vector transmission matrix for the polarization behavior of light propagation in highly scattering media," Opt Express **20**, 16067-16076 (2012).

101. J. W. Goodman, *Speckle phenomena in optics: theory and applications* (Roberts and Company Publishers, 2007).

102. P. H. Beckwith, I. McMichael, and P. Yeh, "Image distortion in multimode fibers and restoration by polarization-preserving phase conjugation," Opt Lett **12**, 510-512 (1987).

103. J. Park, J.-H. Park, H. Yu, and Y. Park, "Focusing through turbid media by polarization modulation," Opt Lett **40**, 1667-1670 (2015).

104. B. Cense, T. C. Chen, B. H. Park, M. C. Pierce, and J. F. de Boer, "Thickness and Birefringence of Healthy Retinal Nerve Fiber Layer Tissue Measured with Polarization-Sensitive Optical Coherence Tomography," Investigative Ophthalmology & Visual Science **45**, 2606-2612 (2004).

105. C. E. Shannon, "Communication in the presence of noise," Proceedings of the IRE **37**, 10-21 (1949).

106. M. Jang, H. Ruan, H. Zhou, B. Judkewitz, and C. Yang, "Method for auto-alignment of digital optical phase conjugation systems based on digital propagation," Opt Express **22**, 14054-14071 (2014).

107. I. N. Papadopoulos, S. Farahi, C. Moser, and D. Psaltis, "Focusing and scanning light through a multimode optical fiber using digital phase conjugation," Opt Express **20**, 10583-10590 (2012).

108. T. R. Hillman, T. Yamauchi, W. Choi, R. R. Dasari, M. S. Feld, Y. Park, and Z. Yaqoob, "Digital optical phase conjugation for delivering two-dimensional images through turbid media," Scientific reports **3**, 1909 (2013).

109. F. Le Clerc, L. Collot, and M. Gross, "Numerical heterodyne holography with two-dimensional photodetector arrays," Opt Lett **25**, 716-718 (2000).

110. I. M. Vellekoop and A. P. Mosk, "Universal Optimal Transmission of Light Through Disordered Materials," Phys Rev Lett **101**, 120601 (2008).

111. M. Fink, "Time-Reversed Acoustics," Scientific American **281**, 67-73 (1999).

112. Z. Ficek and P. D. Drummond, "Time reversed acoustics," Physics today **50**, 34-40 (1997).

113. A. Derode, P. Roux, and M. Fink, "Robust Acoustic Time Reversal with High-Order Multiple Scattering," Phys Rev Lett **75**, 4206-4209 (1995).

114. C. Prada, F. Wu, and M. Fink, "The iterative time reversal mirror: A solution to self-focusing in the pulse echo mode," The Journal of the Acoustical Society of America **90**, 1119-1129 (1991).

115. M. Fink, D. Cassereau, A. Derode, C. Prada, P. Roux, M. Tanter, J.-L. Thomas, and F. Wu, "Time-reversed acoustics," Reports on progress in Physics **63**, 1933 (2000).

116. S. M. Popoff, G. Lerosey, M. Fink, A. C. Boccara, and S. Gigan, "Controlling light through optical disordered media: transmission matrix approach," New Journal of Physics **13**, 123021 (2011).

117. P. Lai, X. Xu, and L. V. Wang, "Ultrasound-modulated optical tomography at new depth," J Biomed Opt **17**, 066006 (2012).

118. H. Ke, T. N. Erpelding, L. Jankovic, C. Liu, and L. V. Wang, "Performance characterization of an integrated ultrasound, photoacoustic, and thermoacoustic imaging system," J Biomed Opt **17**, 056010 (2012).

119. L. Wang and X. Zhao, "Ultrasound-modulated optical tomography of absorbing objects buried in dense tissue-simulating turbid media," Appl Optics **36**, 7277-7282 (1997).

120. S.-R. Kothapalli and L. V. Wang, "Ultrasound-modulated optical microscopy," J Biomed Opt **13**, 054046 (2008).

121. H. Zhang, M. Sabooni, L. Rippe, C. Kim, S. Kröll, L. V. Wang, and P. R. Hemmer, "Slow light for deep tissue imaging with ultrasound modulation," Applied Physics Letters **100**, 131102 (2012).

122. M. Kempe, M. Larionov, D. Zaslavsky, and A. Z. Genack, "Acousto-optic tomography with multiply scattered light," Journal of the Optical Society of America A **14**, 1151-1158 (1997).

123. S.-R. Kothapalli, S. Sakadzic, C. Kim, and L. V. Wang, "Imaging optically scattering objects with ultrasound-modulated optical tomography," Opt Lett **32**, 2351-2353 (2007).

124. M. Gross, P. Goy, and M. Al-Koussa, "Shot-noise detection of ultrasound-tagged photons in ultrasound-modulated optical imaging," Opt Lett **28**, 2482-2484 (2003).

125. S. Sakadžić and L. V. Wang, "High-resolution ultrasound-modulated optical tomography in biological tissues," Opt Lett **29**, 2770-2772 (2004).

126. G. Rousseau, A. Blouin, and J.-P. Monchalin, "Ultrasound-modulated optical imaging using a high-power pulsed laser and a double-pass confocal Fabry–Perot interferometer," Opt Lett **34**, 3445-3447 (2009).

127. Y. Li, H. Zhang, C. Kim, K. H. Wagner, P. Hemmer, and L. V. Wang, "Pulsed ultrasound-modulated optical tomography using spectral-hole burning as a narrowband spectral filter," Applied Physics Letters **93**, 011111 (2008).

128. T. J. Farrell, M. S. Patterson, and B. Wilson, "A diffusion theory model of spatially resolved, steady-state diffuse reflectance for the noninvasive determination of tissue optical properties invivo," Medical physics **19**, 879-888 (1992).

129. C. Ma, X. Xu, and L. V. Wang, "Analog time-reversed ultrasonically encoded light focusing inside scattering media with a 33,000× optical power gain," Scientific reports **5**, 8896 (2015).

Vita

Yan Liu

Degrees

Ph.D., Biomedical Engineering
Washington University in St. Louis, St. Louis, USA
December 2016

B.Eng., Materials Science and Engineering
Also completed all courses of Physics & Optics majors, and most courses of Electronic Engineering major
Tsinghua University, Beijing, China
July 2010

Peer-reviewed journal publications (* denotes co-first authors.)

15. **[**Y. Shen*, **Y. Liu***]**, C. Ma, and L. V. Wang, "Sub-Nyquist sampling boosts targeted light transport through opaque scattering media", in press, ***Optica*** (2016).

14. **Y. Liu**, C. Ma, Y. Shen, J. Shi, and L. V. Wang, "Focusing light inside scattering tissue with millisecond digital optical phase conjugation", under review, ***Optica*** (2016).

13. **[**Y. Shen*, **Y. Liu***]**, C. Ma, and L. V. Wang, "Focusing light through biological tissue and tissue-mimicking phantoms up to 9.6 centimeters in thickness with digital optical phase conjugation", ***Journal of Biomedical Optics*** 21(8), 085001 (2016).

12. **Y. Liu**, Y. Shen, C. Ma, J. Shi, and L. V. Wang, "Lock-in camera based heterodyne holography for ultrasound-modulated optical tomography inside dynamic scattering media", ***Applied Physics Letters***, 108, 231106 (2016).

11. **Y. Liu**, C. Ma, Y. Shen, and L. V. Wang, "Bit-efficient, sub-millisecond wavefront measurement using a lock-in camera for time-reversal based optical focusing inside scattering media", ***Optics Letters***, 41, 1321-1324 (2016).

10. **[**Y. Shen*, **Y. Liu***]**, C. Ma, and L. V. Wang, "Focusing light through scattering media by full-polarization digital optical phase conjugation", ***Optics Letters***, 41, 1130-1133 (2016).

9. **[Y. Liu***, P. Lai*]**, C. Ma, X. Xu, A. A. Grabar, and L. V. Wang, "Optical focusing deep inside dynamic scattering media with near-infrared time-reversed ultrasonically encoded (TRUE) light," ***Nature Communications*** 6 (2015).

8. **Y. Liu**, C. Zhang, and L. V. Wang, "Effects of light scattering on optical-resolution photoacoustic microscopy," ***Journal of Biomedical Optics*** 17(12), 126014 (2012).

7. C. Ma, X. Xu, **Y. Liu**, and L. V. Wang, "Time-reversed adapted-perturbation (TRAP) optical focusing onto dynamic objects inside scattering media," ***Nature Photonics*** 8(12), 931-936 (2014).

6. C. Ma, F. Zhou, **Y. Liu**, and L. V. Wang, "Single-exposure optical focusing inside scattering media using binarized time-reversed adapted perturbation", ***Optica*** 2, 869-876 (2015).

5. L. Gao, A. Garcia-Uribe, **Y. Liu**, C. Li, and L. V. Wang, "Photobleaching imprinting microscopy: seeing clearer and deeper," ***Journal of Cell Science*** 127(2), 288-294 (2014).

4. C. Li, L. Gao, **Y. Liu**, and L. V. Wang, "Optical sectioning by wide-field photobleaching imprinting microscopy," ***Applied Physics Letters*** 103(18) (2013).

3. J. Xia, A. Danielli, **Y. Liu**, L. Wang, K. Maslov, and L. V. Wang, "Calibration-free quantification of absolute oxygen saturation based on the dynamics of photoacoustic signals," ***Optics Letters*** 38(15), 2800-2803 (2013).

2. L. Gao, L. Wang, C. Li, **Y. Liu**, H. Ke, C. Zhang, and L. V. Wang, "Single-cell photoacoustic thermometry," ***Journal of Biomedical Optics*** 18(2), 026003 (2013).

1. M. R. N. Avanaki, A. G. Podoleanu, J. B. Schofield, C. Jones, M. Sira, **Y. Liu**, and A. Hojjat, "Quantitative evaluation of scattering in optical coherence tomography skin images using the extended Huygens-Fresnel theorem," ***Applied Optics*** 52(8), 1574-1580 (2013).